

A high spatial resolution X-ray and H α study of hot gas in the halos of star-forming disk galaxies. I. Spatial and spectral properties of the diffuse X-ray emission

David K. Strickland,^{1,2,3} Timothy M. Heckman,³ Edward J.M. Colbert,³ Charles G. Hoopes,³ and Kimberly A. Weaver.⁴

ABSTRACT

We present arcsecond resolution *Chandra* X-ray and ground-based optical H α imaging of a sample of ten edge-on star-forming disk galaxies (seven starburst and three “normal” spiral galaxies), a sample which covers the full range of star-formation intensity found in disk galaxies. The X-ray observations make use of the unprecedented spatial resolution of the *Chandra* X-ray observatory to more robustly than before remove X-ray emission from point sources, and hence obtain the X-ray properties of the diffuse thermal emission alone. We have combined the X-ray observations with existing, comparable-resolution, ground-based H α and R-band imaging, and present a mini-atlas of images on a common spatial and surface brightness scale to aid cross-comparison. In general, the morphology of the extra-planar diffuse X-ray emission is very similar to the extra-planar H α filaments and arcs, on both small and large scales (scales of 10’s of pc and kiloparsecs respectively). The most spectacular cases of this are found in NGC 1482 (for which we provide the first published X-ray observation) and NGC 3079. We provide a variety of quantitative measures of how the spectral hardness and surface brightness of the diffuse X-ray emission varies with increasing height z above the plane of each galaxy. Of the eight galaxies in which diffuse X-ray emitting halos are found (the starbursts and the normal spiral NGC 891), significant spatial variation in the spectral properties of the extra-planar emission ($|z| \geq 2$ kpc) is only found in two cases: NGC 3628 and NGC 4631. In general, the vertical distribution of the halo-region X-ray surface brightness is best described as an exponential, with the observed scale heights of the sample galaxies lying in the range $H_{\text{eff}} \sim 2 - 4$ kpc. The presence of extra-planar X-ray emission is always associated with the presence of extra-planar optical line emission of similar vertical extent. No X-ray emission was detected from the halos of the two low mass normal spiral galaxies NGC 6503 and NGC 4244. AGN, where present, appear to play no role in powering or shaping the outflows from the the starburst galaxies in this sample. The *Chandra* ACIS X-ray spectra of extra-planar emission from all these galaxies can be fit with a common two-temperature spectral model with an enhanced α -to-iron element ratio. This is consistent with the origin of the X-ray emitting gas being *either* metal-enriched merged SN ejecta *or* shock-heated ambient halo or disk material with moderate levels of metal depletion onto dust. Our favored model is that SN feedback in the disks of star-forming galaxies create, via blow out and venting of hot gas from the disk, tenuous exponential atmospheres of density scale height $H_g \sim 4 - 8$ kpc. The soft thermal X-ray emission observed in the halos of the starburst galaxies is either this pre-existing halo medium, which has been swept-up and shock heated by the starburst-driven wind, or wind material compressed near the walls of the outflow by reverse shocks within the wind. In either case the X-ray emission provides us with a powerful probe of the properties of gaseous halos around star-forming disk galaxies.

Subject headings: ISM: jets and outflows — ISM: bubbles — galaxies: individual (NGC 253; NGC 891; NGC 1482; NGC 3034 (M82); NGC 3073; NGC 3079; NGC 3628; NGC 4244; NGC 4631; NGC 4945; NGC 6503) — galaxies: halos — galaxies: starburst — X-rays: galaxies

1. Introduction

Massive stars exercise a profound influence over the baryonic component of the Universe, through the return of ionizing radiation, and via supernovae (SNe), kinetic energy and metal-enriched gas, back into the interstellar medium (ISM) from which they form — usually called “feedback”. Feedback influences gas-phase conditions in the immediate environment of the clusters within which the massive stars form (McKee 1995; Hollenbach & Tielens 1997; Wiseman & Ho 1998; Pudritz & Fiege 2000), on galactic scales the phase structure and energetics of the ISM (McKee & Ostriker 1977; Cox 1981; Norman & Ikeuchi 1989; Norman & Ferrara 1996), and on multi-Mpc scales the thermodynamics and enrichment of the inter-galactic medium (IGM — e.g. see Chiang, Ryu & Vishniac 1988; Heckman, Armus & Miley 1990; Shapiro, Giroux & Babul 1994; Voit 1996; Heckman 1999; Aguirre et al. 2001).

The vast range of spatial scales involved is only one of the difficulties encountered in attempting to study feedback. Restricting the discussion to purely mechanical feedback from SNe and stellar winds (commonly termed SN feedback), a further difficulty is the broad range of complicated gas-phase physics – (magneto)hydrodynamic effects such as shocks and turbulence, thermal conduction, and non-ionization equilibrium emission processes. A final complication is that much of the energy and metal-enriched material involved is in the hard-to-observe coronal ($T \gtrsim 10^5$ K) and hot ($T \gtrsim 10^6$ K) gas phases, necessitating the use of space-based FUV and X-ray telescopes.

X-ray observations of the halo-regions of nearby edge-on disk galaxies provide the best single probe of the action of mechanical feedback on the galactic scale. Optical spectroscopy and imaging, sensitive to warm neutral and ionized gas with $T \sim 10^4$ K, are a less direct probe of mechanical feedback as much of the excitation energy is supplied by ionizing radiation from massive stars (radiative feedback), even when the kinematics and spatial distribution of this gas are controlled by SN feedback. If mechanical feedback processes transport mass, newly-synthesized metals, and

energy from galaxies into the IGM, then this material must pass through the halo of the host galaxy on its way into the IGM, where its properties can be ascertained before it expands and fades into observational invisibility.

Diffuse thermal X-ray emission is seen to extend to large distances (5 to 20 kpc) above the planes of edge-on *starburst* galaxies (e.g. Fabbiano, Heckman & Keel 1990; Armus et al. 1995; Read, Ponman & Strickland 1997; Dahlem, Weaver & Heckman 1998), which also show unambiguous optical emission line evidence for energetic galactic scale outflows — “superwinds” (Heckman et al. 1990). These outflows are potentially very significant in enriching and heating the IGM (Heckman 1999).

That superwinds can be driven by the collective power of large numbers of supernovae is beyond doubt — the observational evidence for the link between starburst regions and kinematic and/or morphological evidence of outflow is overwhelming (e.g. see Bland & Tully 1988; Heckman et al. 1990; McKeeth et al. 1995; Lehnert & Heckman 1995, 1996; Dahlem 1997, among many others). Nevertheless, the question of whether Seyfert nuclei or low-luminosity AGN (LLAGN) can also contribute significantly to these outflows, or can directly drive poorly-collimated superwind-like outflows in the absence of any starburst, has been raised many times (Schiano 1985; Veilleux et al. 1994; Colbert et al. 1996a,b; Williams, Baker & Perry 1999; Pietsch, Trinchieri & Vogler 1998; Veilleux et al. 2002). This is a potentially serious complication for assessing SN feedback, as many of the “classical” starburst superwind galaxies also host weak Seyferts or LLAGN.

Both fully-numerical and semi-analytical theoretical modeling (Suchkov et al. 1994; Silich & Tenorio-Tagle 1998; Murakami & Babul 1999) suggest that the properties of the gaseous halos these winds expand into play a major role in determining the fate of the material in superwinds (i.e. escape into the IGM, or confinement and eventual return to the disk). Although simulations of starburst-driven winds should be treated with caution, given the lack of calibration against observational data, one robust result is the sensitivity of the wind properties (in particular mass and metal loss to the IGM) on the disk and halo ISM properties (e.g. De Young & Heckman 1994; Suchkov et al. 1994; Silich & Tenorio-Tagle 1998; Strickland & Stevens 2000; Silich & Tenorio-Tagle 2001). In our view, the emphasis given to galactic mass as a primary paramete-

¹Chandra Fellow.

²Guest investigator of the UK Astronomy Data Centre.

³Department of Physics and Astronomy, The Johns Hopkins University, 3400 North Charles Street, Baltimore, MD 21218

⁴NASA/Goddard Space Flight Center, Code 662, Greenbelt, Maryland 20771

ter influencing gas and metal ejection efficiencies (e.g. Dekel & Silk 1986; Mac Low & Ferrara 1999; Ferrara & Tolstoy 2000; Ferrara et al. 2000) blinds non-expert readers to the more fundamental role played by the poorly-known disk and halo ISM distributions. The gravitational potential only enters at a secondary level, by influencing the gas distribution and finally via the escape velocity. Redressing the lack of observational knowledge about the gaseous halos that superwinds must pass through is one motivation for studying the halos of *normal* star-forming galaxies.

Modern theories of the ISM in normal spiral galaxies also predict hot gas in the halo, due to the interchange of material between the disk and halo through “galactic fountains” (Shapiro & Field 1976; Bregman 1980; de Avillez 2000), or in a more-localized form through “chimneys” (Norman & Ikeuchi 1989). Energy feed back into the ISM from supernovae is believed to create bubbles of hot, metal-enriched, gas, which blow out of the disk and vent their contents into the halo of the galaxy. After $\gtrsim 10^8$ years or so, this material cools and falls back to the disk, possibly in a form analogous to the Galactic high velocity clouds.

Unfortunately, many of the fundamental aspects of these fountain/chimney disk/halo interaction theories are observationally unconstrained, fundamentally due to our *current* lack of knowledge about the X-ray properties of spiral galaxy halos. Studies, with *Einstein* and the *ROSAT* PSPC, of nearby edge-on star-forming galaxies revealed *only one* genuinely normal spiral, NGC 891 (Bregman & Pildis 1994), with X-ray-emitting gas in its halo (although it is common to find starburst galaxies with hot halos mistakenly classified as normal spirals, e.g. NGC 4631). Although edge-on normal spiral galaxies did not receive as much attention with *Einstein* & *ROSAT* as other classes of galaxy, those observations that were performed failed to produce believable detections of hot halo gas in other edge-on normal star-forming galaxies (Bregman & Glassgold 1982; Vogler, Pietsch & Kahabka 1995; Bregman & Houck 1997; Fabbiano & Juda 1997; Benson et al. 2000).

It is also not clear to what extent fountains are a distinct phenomenon from superwinds. It is not unreasonable to think that physical conditions and kinematics of the gas making up a fountain may be quite different from that in a superwinds, despite the general similarity in driving mechanism. For example, the filling factor of the dominant X-ray-emitting plasma might be high in a fountain (Bregman 1980), as compared

to superwinds where the filling factor is low (Chevalier & Clegg 1985; Suchkov et al. 1994; Strickland & Stevens 2000; Strickland et al. 2000). Intriguingly, in a *ROSAT* PSPC-based sample of both normal spiral galaxies and starburst galaxies of all inclinations, Read & Ponman (2001) find that the X-ray-emitting gas “in the coronal systems [*i.e.* galaxies assumed to have a hydrostatic hot gas corona/halo] appears to be cooler than that seen in the wind systems [*i.e.* starburst galaxies with superwinds]”.

1.1. A description of the present study

In this paper we report the results of a small, but representative, survey of the diffuse X-ray emission from 10, approximately edge-on, star-forming disk galaxies using the ACIS imaging CCD spectrometer on the *Chandra* X-ray Observatory.

Compared to previous *ROSAT* and/or *ASCA*-based studies, or even current work using *XMM-Newton*, the use of *Chandra* offers significant advantages. Firstly, *Chandra*’s unequaled spatial resolution¹ allows the robust detection and removal of X-ray emission from the extremely numerous X-ray point sources found in star-forming galaxies, and the foreground and background point sources found over the entire sky, without the loss of large areas of sky. Secondly, accurately quantifying the spatial morphology and surface brightness of the diffuse emission requires a resolution well matched to the physical sizes of interest, *i.e.* equivalent to the ground-based optical imaging.

In § 2 we discuss simple methods of assessing the intensity of star formation in galaxies, and the sample of galaxies in this paper. The data analysis techniques we have used are presented in § 3. The properties of the diffuse X-ray emission in the halos of 7 starburst and 3 normal spiral galaxies we observed are presented in § 4. We provide a detailed discussion of the location of the X-ray emission with respect to other properties of the galaxies in § 4.2, a quantitative study of the spatial variation of the spectral hardness and surface brightness along the minor axis (§4.3), and the spectral properties of the halo X-ray emission (§5). In § 6 we discuss and interpret some of these results, and summarize the results and conclusions of this paper in § 7.

¹The on-axis angular resolution of ACIS is $\sim 0''.8$ (FWHM), which corresponds to a physical scale of $\sim 7.8(D/2\text{Mpc})$ pc for a source at distance D . By way of comparison, the resolution of the *ROSAT* HRI was $\sim 5''$, *XMM-Newton* $\sim 6''$ and *ROSAT* PSPC $\sim 30''$.

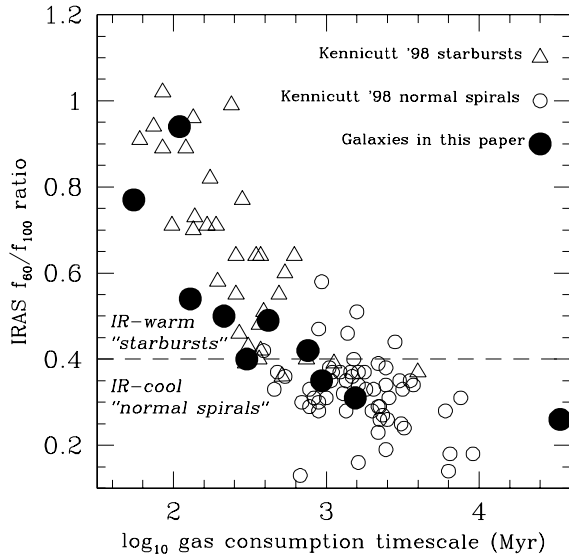


Fig. 1.— Infrared warmth and gas consumption timescales for our edge-on star-forming galaxy sample (filled circles), compared to other starburst (open triangles) and normal spiral (open circles) galaxies from the Kennicutt (1998a) sample. See discussion in § 2.

In Strickland et al. (2004, henceforth referred to as Paper II) we investigate how the empirical properties of the hot gas, in particular the extra-planar emission, correlate with the size, mass, star formation rate and star formation intensity in the host galaxies. We find that SN-feedback models best explain the observed diffuse X-ray emission. We use this data to empirically test basic, but fundamental, aspects of wind and fountain theories, in particular the critical energy required for disk “blow-out” (e.g. Mac Low & McCray 1988), and then discuss the issue of halo blow-out.

We shall present a quantitative study of the relationship between the $H\alpha$ surface brightness, optically-derived gas kinematics, and the physical origin and properties of the halo thermal X-ray emission in a separate future paper.

2. Star formation in disk galaxies, and our edge-on disk galaxy sample

Our sample of edge-on ($i \gtrsim 60^\circ$) star-forming galaxies is formed from seven starburst galaxies and three “normal” star-forming galaxies. Basic physical properties of the sample galaxies are shown in Table 1. We have chosen to study only mod-

erate luminosity ($L_{\text{BOL}} \sim 10^{10} L_\odot$), moderate-mass ($M \sim 10^{10} - 10^{11} M_\odot$) disk galaxies within a distance of $D \lesssim 20$ Mpc, and not include any *Chandra* observations of star-forming dwarf galaxies or ultra-luminous infrared galaxies (ULIRGs). Given that the physical conditions in these other systems are somewhat distinct from star-forming disks, and that they rarely present the clean “edge-on” geometry necessary to separate disk X-ray emission from halo X-ray emission, it makes sense to study them separately, at least initially. Furthermore, the X-ray fluxes from both the dwarf starbursts and the ULIRGs are considerably lower than those of the typical galaxies within this sample.

This work can be considered as an updated version of earlier *ROSAT* PSPC and *ASCA* based surveys of diffuse X-ray emission in star-forming galaxies (Read, Ponman & Strickland 1997; Dahlem, Weaver & Heckman 1998; Read & Ponman 2001), with which our sample shares many galaxies in common.

2.1. Star formation rates and star-formation intensities

Our sample spans the full range of star formation activity found in disk galaxies (see Fig. 1), although we emphasize that it is not complete in any flux or volume-limited sense. In Fig. 1 we plot the estimated gas consumption time-scales for the galaxies in our sample, along with the normal and starburst galaxies from Kennicutt 1998a, against the IRAS 60 to $100\mu\text{m}$ flux ratio. The gas consumption time-scale is simply the ratio of the total gas mass (atomic plus molecular gas) divided by the star formation rate, $\tau_{\text{gas}} = M_{\text{gas}}/\dot{M}_{\text{SFR}}$. Starbursts are traditionally defined as those galaxies that would totally consume the gas reserves within the star forming region in a time significantly less than a Hubble time (typically within a few hundred Myr), were star formation to continue at the currently observed rate. More normal spiral galaxies, such as NGC 891 and the Milky Way have gas consumption time-scales of order several Gyr (Kennicutt, Tamblyn & Congdon 1994; de Mello, Wiklind & Maia 2002).

The gas consumption time-scales were calculated directly from the gas surface densities and star-formation rate surface densities given in Kennicutt (1998a), except for NGC 1482, NGC 3628, NGC 4244, NGC 4631 & NGC 4945, which were not part of Kennicutt’s sample. For these galaxies used the

TABLE 1
BASIC PHYSICAL PROPERTIES OF THE SAMPLE GALAXIES

Galaxy	α, δ (J2000) (h m s, ° ' '')	i (°)	PA (°)	v_{rot} (km/s)	D (Mpc)	scale (pc)	f_{60} (Jy)	f_{60}/f_{100}	$L_{\text{IR}}/(10^{10} L_{\odot})$			$L_{\text{H}\alpha}$ ($10^{40} \text{ erg s}^{-1}$)	M_{TF} ($10^{10} M_{\odot}$)	SFR_{IR} ($M_{\odot} \text{ yr}^{-1}$)	$\log \tau_{\text{gas}}$
(1)	(2)	(3)	(4)	(5)	(6)	(7)	(8)	(9)	(L_{IR}) (10)	(L_{K}) (11)	(L_{B}) (12)	(13)	(14)	(15)	(16)
M82	09 55 51.9 +69 40 47.1 ^a	73 ^b , 82 ^c	65 ^d	137 ^a	3.6 ^e	17.5	1313.5 ^f	0.97	5.36	0.75	0.33	7.0 ^g	1.9	9.2	2.04
NGC 1482	03 54 39.3 -20 30 08.9 ^h	58 ⁱ	103 ^j	165 ^k	22.1	107.1	35.3 ^f	0.77	5.00	0.84	0.38	N 9.4 ^l	3.6	8.6	1.74
NGC 253	00 47 33.2 -25 17 16.2 ^m	79 ⁿ , 72 ^o	52 ^d , 49 ^o	225 ^m	2.6 ^p	12.6	936.7 ^f	0.50	2.10	0.89	0.58	3.6 ^q	10.6	3.6	2.11
NGC 3628	11 20 16.95 +13 35 20.1 ^r	87 ^s , 80 ^r	104 ^d	229 ^r	10.0 ^u	48.5	51.6 ^f	0.50	1.74	1.58	1.06	N 2.3 ^v	11.3	3.0	2.33
NGC 3079	10 01 57.8 +55 40 47.2 ^w	85 ^w	165 ^d	244 ^r	17.1	82.9	50.2 ^f	0.49	4.76	1.55	0.98	N 9.1 ^d	14.1	8.1	2.62
NGC 4945	13 05 25.3 -49 29 09.0 ^x	78 ^y	43 ^y	184 ^r	3.7	17.9	588.1 ^z	0.42	2.70	0.94	0.73	N 2.4 ^d	5.2	4.6	2.88
NGC 4631	12 42 07.2 +32 32 31.9 ^{aa}	85 ^{ab} , 81 ^{ac}	86 ^{ac} , 83 ^{ac}	150 ^{ab}	7.5 ^{ab}	36.4	82.9 ^z	0.40	1.74	0.62	0.98	N 14.3 ^{ad}	2.6	3.0	2.48
NGC 6503	17 49 26.4 +70 08 39.7 ^{ae}	75 ^{af}	123 ^{af}	120 ^{ag}	5.2 ^{ah}	25.2	10.2 ^f	0.35	0.12	0.14	0.18	0.76 ^{ai}	1.2	0.20	2.97
NGC 891	02 22 33.2 +42 20 56.2 ^{aj}	89 ^{aj}	23 ^{aj}	225 ^f	9.6	46.5	61.1 ^z	0.31	2.47	1.66	0.78	3.3 ^{ae}	10.6	4.2	3.19
NGC 4244	12 17 29.7 +37 48 20.4 ^{ak}	85 ^{ak}	48 ^{ak}	100 ^{ak}	3.6	17.5	4.2 ^z	0.26	≤ 0.02	0.04	0.08	0.42 ^{ad}	0.6	0.04	4.53

NOTE.—Column 2: Coordinates of the dynamical center of the galaxy, where available. Column 3: Inclination. Column 4: Position angle of the galactic disk. Multiple values for the inclination and position angle are given when several values are often reported in the literature. Column 5: Inclination-corrected circular velocity within the disk. Column 6: Assumed distance. Unless a specific reference is given, distances were calculated using the galaxy recessional velocity with respect to the microwave background (de Vaucouleurs et al. 1991), and $H_0 = 75 \text{ km s}^{-1} \text{ Mpc}^{-1}$. Column 7: Physical distance corresponding to an angular size of 1 arcsecond. Column 8: IRAS 60 μm flux in Janskys. Column 9: IRAS 60 to 100 μm flux ratio. Column 10: Total IR luminosity based on the observed IRAS fluxes, $L_{\text{IR}} = 5.67 \times 10^5 D_{\text{Mpc}}^2 \times (13.48f_{12} + 5.16f_{25} + 2.58f_{60} + f_{100}) L_{\odot}$, where D_{Mpc} is the distance to the galaxy in Mpc (Sanders & Mirabel 1996). Given the large angular size of these local galaxies we use IRAS fluxes from extended source analyses, the exact source of the IRAS data used is given in a case by case basis above. Where multiple measurements were available for any galaxy, we used the following sources in order of preference: Rice et al. (1988), and Soifer et al. (1989). Column 11: K-band luminosity, calculated from the K-band total magnitudes given in Jarret et al. (2003) and converted to the Cousins-Glass-Johnson system using the transformations presented in Carpenter (2001). Zero points for conversion from magnitude to flux were taken from Bessel, Castelli & Plez (1998). Note that the units are L_{\odot} , not $L_{\text{K},\odot}$. Column 12: B-band luminosity from RC3 catalog B_T magnitude (de Vaucouleurs et al. 1991), and corrected for Galactic extinction using reddening values from Burstein & Heiles (1982). Note that no correction for extinction internal to the specific galaxy has been made. Column 13: Observed H α -luminosity in units of $10^{40} \text{ erg s}^{-1}$. Note these values have *not* been corrected for extinction. Measurements that have not been corrected for [NII] emission are marked with a preceding N . Column 14: Baryonic mass (stellar plus HI) estimated from the K-band Tully Fisher relationship of Bell & de Jong (2001), where $M_{\text{TF}} = 10^{9.79} \times (v_{\text{rot}}/100 \text{ km s}^{-1})^{3.51} M_{\odot}$. Column 15: Total galactic star formation rate in units of $M_{\odot} \text{ yr}^{-1}$ estimated from the IR luminosity (Kennicutt 1998b), where $SFR_{\text{IR}} = 4.5 \times 10^{-44} L_{\text{IR}} [\text{erg s}^{-1}]$. Column 16: Logarithm of the gas consumption timescale in Myr, where $\log \tau_{\text{gas}} = \log \Sigma_{\text{gas}} - \log \Sigma_{\text{SFR}}$, and Σ_{gas} and Σ_{SFR} are the surface density of gas ($M_{\odot} \text{ pc}^{-2}$) and star-formation rate ($M_{\odot} \text{ yr}^{-1} \text{ kpc}^{-2}$) respectively. Data are from Kennicutt (1998a), except for NGC 1482, NGC 3628, NGC 4244, NGC 4631 and NGC 4945. For these galaxies the star formation rate was estimated from the IRAS fluxes. Gas masses were obtained from Elfhag et al. (1996) for NGC 1482 (using the CO brightness to H_2 column density scaling in Kennicutt (1998a), and a radius of 2 kpc, as ISO observations by Dale et al. (2000) demonstrate that 80% of the star-formation occurs within this radius), Irwin & Sofue (1996) for NGC 3628 (central, $R \leq 340 \text{ pc}$, H_2 gas mass), from Olling (1996) for NGC 4244 (total HI gas mass), from Golla & Wielebinski (1994) for NGC 4631 (H_2 gas mass for $R \leq 2.5 \text{ kpc}$) and from Dahlem et al. (1993) for NGC 4945 (molecular gas mass within central 1.1 kpc).

References. — (a) Weliachew, Fomalont & Greisen (1984), (b) Ichikawa et al. (1995), (c) Lynds & Sandage (1963), (d) Lehnert & Heckman (1995), (e) Freedman et al. (1994), (f) Soifer et al. (1989), (g) McCarthy, Heckman & van Bruegel (1987), (h) 2MASS Second Incremental Release, (i) Hameed & Devereux (1999), (k) Calculated assuming $v_{\text{rot}} = W_{20}/2 \sin^2 i$, using the W_{20} value from Roth, Mould & Davies (1991), (l) Hameed & Devereux (1999), (m) Sorai et al. (2000), (n) Pence (1981), (o) Puche, Carignan & van Gorkom (1991), (p) Puche & Carignan (1988), (q) From H α images published in Strickland et al. (2002a), (r) Douglas et al. (1996), (s) Irwin & Sofue (1996), (t) Sofue (1997), (u) Soifer et al. (1987) (v) Fabbiano et al. (1990), (w) Irwin & Seaquist (1991), (x) Ott et al. (2001), (y) Koorneef (1993), (z) Rice et al. (1988), (aa) Dynamical center, Golla & Wielebinski (1994), (ab) Rand (1994), (ac) Golla (1999), (ad) Hoopes et al. (1999), (ae) Central optical & X-ray source, Lira, Johnson & Lawrence (2002), (af) de Vaucouleurs et al. (1991), (ag) Bottema & Gerritsen (1997), (ah) Karachentsev & Sharina (1997), (ai) Kennicutt (1998a), (aj) Nuclear 1.4 GHz continuum point source, Rupen (1991), (ak) HI dynamical center, Olling (1996).

same methodology of Kennicutt (1998a) to calculate the nuclear-region gas consumption time-scale. Gas masses were obtained from the CO and H I data of Elfhag et al. (1996), Irwin & Sofue (1996), Olling (1996), Rand (1994), Golla & Wielebinski (1994) and Dahlem et al. (1993), and the star-formation rates were calculated from the IR luminosity using the relationship given in (Kennicutt 1998b). Values for the calculated star formation rates and gas consumption time scales are given in Table 1.

Fig 1 also validates the definition of galaxies with a IRAS flux ratio $f_{60}/f_{100} > 0.4$ as being starburst galaxies. Physically, the dust temperature in a star-forming galaxy (and hence the IRAS f_{60}/f_{100} ratio) is related to the energy density of the inter-stellar radiation field (in particular the energy density in the UV, from 900 to 3000 Å, see Désert, Boulanger & Puget 1990), and hence is related to the star-formation rate per unit area of the disk².

Theoretically, the fraction of the mechanical energy returned to the ISM by massive stars that is available to drive large scale flows (*i.e.* that fraction that is not radiated away) is a function of the SN rate per unit volume, as this directly alters the porosity of the ISM, and hence the radiative losses SNe experience (Larson 1974; McKee & Ostriker 1977; Slavin & Cox 1993). Feedback in a galaxy should then depend on the star formation intensity (SF rate per unit disk area or per unit volume), in addition to the total SF rate. Therefore we display the sample galaxies in all figures, and list them in all further tables, in order of decreasing f_{60}/f_{100} ratio.

2.2. The starburst galaxies

The starburst galaxies in our sample are all good examples of the “typical” starburst galaxy in the local universe, *i.e.* infrared warm (IRAS 60 to 100 μm flux ratio $f_{60}/f_{100} \geq 0.4$) galaxies with a far-infrared luminosity $L_{\text{FIR}} \approx$ a few $\times 10^{10} L_{\odot}$ (Soifer et al. 1987). Minor-axis velocity-split optical emission lines provide unambiguous kinematic evidence for $v \sim 300$ to 600 km s^{-1} outflows — galactic superwinds — in M82, NGC 253, NGC 4945, NGC 3079 & NGC 1482 (Bland & Tully 1988; Heckman et al. 1990; Cecil et al. 2001; Veilleux & Rupke 2002). Spectroscopic ev-

²Based on the data presented in Désert et al. (1990), then to first order $f_{60}/f_{100} \sim 0.32 \times U_{\text{ISRF}}^{1/3}$, where U_{ISRF} is the energy density in the interstellar radiation field in units of eV cm^{-3} . Note that this only applies when massive stars dominate the dust heating.

idence for outflow is weaker, but still compelling, for NGC 3628 (Fabbiano, Heckman & Keel 1990; Irwin & Sofue 1996). NGC 4631 (where the star-formation activity is more widely spatially distributed than in the other starbursts of this sample) currently lacks spectroscopic evidence for a outflow, apart for one region to the south of the brightest H II region (Golla, Dettmar & Domgörgen 1996). With the exception of NGC 4945 (which is at low Galactic latitude and hence suffers high foreground obscuration), all of these galaxies have clearly-detected, ~ 5 to 20 kpc-scale, extra-planar (“halo”) diffuse X-ray and H α emission, again typical of galaxies with $f_{60}/f_{100} \geq 0.4$ (Heckman et al. 1990; Lehnert & Heckman 1995, 1996; Dahlem et al. 2001).

2.3. The normal spiral galaxies

At present there are relatively few *Chandra* observations aimed at normal (*i.e.* non-starburst, non-Seyfert) spiral galaxies, and the majority of these galaxies are not edge-on. Our sample includes the only spiral galaxies with $i > 60^\circ$ and IRAS $f_{60}/f_{100} < 0.4$ that have been observed with *Chandra* for which the data was available as of 2002 September: NGC 891, NGC 4244, & NGC 6503.

NGC 891 is a well-studied spiral galaxy, believed to be relatively similar to our own galaxy, although somewhat more IR-luminous. It is the *only* “normal” spiral galaxy (apart from possibly our own) for which robust evidence of extra-planar diffuse X-ray emission has been discovered (Bregman & Pildis 1994). Both NGC 6503 and NGC 4244 are relatively low mass spiral galaxies. Individual galaxies are discussed in more detail in § 4.2.

2.4. AGN contamination

Only two of these galaxies host AGN luminous enough to possibly bias the the star-formation rate and intensity diagnostics we employ in this paper and in Paper II. These galaxies are NGC 4945 (e.g. Whiteoak 1986; Marconi et al. 2000), and to a lesser extent NGC 3079 (e.g. Hawarden et al. 1995; Trotter et al. 1998). The luminosity of these AGN, their effect on the SF-rate indicators, and a quantitative investigation of whether the AGN are partially responsible for the outflows from these galaxies will be addressed in a future paper. In § 6 we provide a preliminary, more qualitative, discussion of whether the AGN play a significant role driving the outflows in these specific galax-

ies. Note that the luminosities and star formation rates given in Table 1 have not been corrected in any way for the (rather uncertain) AGN contribution.

3. Data sources and data reduction

3.1. X-ray data

The *Chandra* ACIS data for the 10 sample galaxies comprises 11 ACIS-S observations and 2 ACIS-I observations (see Table 2). The 6 ACIS-S observations of the starburst galaxies M82, NGC 253 (two separate observations), NGC 1482, NGC 3079 and NGC 3628 are all from guest observer programs awarded to our group. The *Chandra* data for the remaining galaxies was obtained from the *Chandra* data archive.

All the *Chandra* data were reduced and analyzed in a uniform, self-consistent, manner using a scripted analysis pipeline employing the CIAO (version 2.2.1) and HEASOFT (version 5.2, XSPEC version 11.2.0h) software packages. For a more detailed description of many of the data analysis techniques used we refer the reader to Strickland et al. (2002a). Unless otherwise stated, our data processing follows the recommended guide lines released by the CXC and the ACIS instrument team³. Our analysis procedures take account of all currently known bugs and peculiarities of the CIAO software. A few points of specific importance are discussed below.

3.1.1. Calibration and spectral response files used

The original *Chandra* data files were reprocessed to update the instrument gain and astrometric solution, using version 2.12 of the *Chandra* Calibration Database (CALDB).

The officially recommended randomization of (spatially dependent) pulse height amplitude (PHA) channel values to (spatially-independent) PI channel value was applied. The artificial $\sim 0''.5$ spatial blurring applied in the default *Chandra* pipeline was *not* applied in our reprocessing — the resulting optical-axis point source point spread function we measure in the data is $0.8 \pm 0.1''$ FWHM.

The two ACIS-I observations of M82 (ObsIDs 361 & 1302), taken on the same day, were combined into a single dataset using the CIAO task RE-

³The CIAO (v2.2) Science Threads can be found at http://asc.harvard.edu/ciao/documents_threads.html, and the Penn State University ACIS instrument team's recipes at <http://www.astro.psu.edu/xray/acis/recipes/>.

PROJECT_EVENTS. We have not attempted to correct these ACIS-I observations for the radiation-damaged-induced charge transfer inefficiency problem (e.g. see Townsley et al. 2000), as the $\sim 20\%$ in energy resolution and quantum efficiency this would provide is small compared to other sources of uncertainty.

3.1.2. Background flare removal

Short periods of significantly-enhanced background count rate – “flares” – were removed using the iterative 3σ clipping technique described in Strickland et al. (2002a). The “good” exposure times, *i.e.* that remaining after clipping, are given in Table 2.

3.1.3. Astrometric accuracy

We use the default astrometric solutions, based on the latest reprocessing of all observations available as of June 2002. Typically, the 90% uncertainty⁴ in the *Chandra* astrometric solution is $0''.6$. We have only explicitly checked the astrometry for X-ray point sources that have optical counterparts in the NGC 253 and NGC 3628 *Chandra* observations, which we find are accurate to within $0''.5$.

3.1.4. Point source detection and removal

We used the wavelet-based source detection algorithm WAVDETECT to search for point-like objects in each X-ray observation. Each chip was treated separately, searching for sources in images created in the soft X-ray 0.3 – 2.0 keV energy-band, hard X-ray 2.0 – 8.0 keV energy band and total 0.3 – 8.0 keV energy band. Only sources with signal-to-noise ratios ≥ 2 were accepted as point sources, in the initial iteration of the data analysis.

We screen out point sources from the data used for both imaging and spectral analysis to a radius equivalent to 4 Gaussian σ , based on a fit to the radius of the *Chandra* PSF as a function of off-axis angle. The holes left in any image by source removal are filled in using the CIAO task DMFILTH. The observed distribution of pixel values in a background annulus around the point source, defines the probability density function from which random values are chosen to fill in the source region (The DIST option in DMFILTH). Care was taken to ensure that the background annulus chosen did not contain other point sources, which would

⁴From “*Chandra* absolute astrometric accuracy”, <http://asc.harvard.edu/cal/ASPECT/celmon/index.html>

TABLE 2
CHANDRA X-RAY OBSERVATION LOG

Galaxy	ObsID	Observation date, days since launch	α, δ (J2000) (h m s, $^{\circ}$ ' '')	Roll (deg)	Mode	FP Temp. ($^{\circ}$ C)	Active chips (8)	Good time (ks)	(10)
(1)	(2)	(3)	(4)	(5)	(6)	(7)	(8)	(9)	(10)
M82	361+1302	1999 Sep 20, 55	09 55 55.1 +69 40 47.4	30	ACIS-I	-110	012367	48.51 I1	48.50 I3
M82	2933	2002 Jun 18, 1061	09 55 53.6 +69 40 12.6	288	ACIS-S	-120	235678	17.76 S2	17.99 S3
NGC 1482	2932	2002 Feb 05, 928	03 54 39.9 -20 30 42.1	289	ACIS-S	-120	235678	27.90 S2	23.46 S3
NGC 253	969	1999 Dec 16, 146	00 47 34.0 -25 17 53.9	299	ACIS-S	-110	56789	13.50 S2	10.99 S3
NGC 253	790	1999 Dec 27, 157	00 47 21.3 -25 13 00.6	300	ACIS-S	-110	56789	43.30 S2	38.30 S3
NGC 3628	2039	2000 Dec 12, 508	11 20 18.4 +13 35 53.5	71	ACIS-S	-120	456789	56.60 S2	54.70 S3
NGC 3079	2038	2001 Mar 07, 593	10 01 53.3 +55 40 41.9	200	ACIS-S	-120	235678	26.69 S2	26.52 S3
NGC 4945	864	2000 Jan 27, 188	13 05 29.1 -49 27 51.5	61	ACIS-S	-120	23678	40.66 S2	28.66 S3
NGC 4631	797	2000 Apr 16, 268	12 41 56.9 +32 37 33.9	201	ACIS-S	-120	235678	57.61 S2	55.67 S3
NGC 6503	872	2000 Mar 23, 244	17 49 28.4 +70 09 19.2	95.6	ACIS-S	-120	23678	12.91 S2	10.64 S3
NGC 891	794	2000 Nov 01, 467	02 22 22.2 +42 20 49.9	187	ACIS-S	-120	235678	49.68 S2	30.72 S3
NGC 4244	942	2000 Mar 20, 241	12 17 22.1 +37 46 50.6	231	ACIS-S	-120	235678	48.84 S2	47.51 S3

NOTE.—Column 2: *Chandra* observation identification number. Two separate observations of M82, taken on the same day and with the same telescope pointing, were merged. Column 4: Telescope axis pointing direction. Column 5: Telescope roll angle in degrees. Column 7: Focal plane CCD temperature. Column 8: Identification numbers for the CCD chips active during the observation. Chips 5 and 7 (a.k.a. S1 and S3) are back-illuminated chips. The remaining chips are all front-illuminated chips. The images and spectra described in this paper are taken from only those chips shown in bold-face. Columns 9 and 10: The remaining exposure time left *after* removal of periods of high background count rate, for the two most important chips in each observation (the chosen chips are specified alongside the exposure time).

TABLE 3
X-RAY BACKGROUND RATES AND POINT SOURCE SENSITIVITIES

Galaxy	N_{H}	τ_{Oviii}	BG method	Background surface brightness			2σ PS sensitivity	
				0.3–1 keV	1–2 keV	2–8 keV	f_{X}	L_{X}
(1)	(2)	(3)	(4)	(5)	(6)	(7)	(8)	(9)
M82 ^a	4.0	0.237	local	2.45	1.63	6.28	2.4×10^{-15}	3.8×10^{36}
M82 ^b	4.0	0.237	blank sky	6.31	2.95	9.76	4.7×10^{-15}	7.3×10^{36}
NGC 1482	3.7	0.219	blank sky	6.61	3.09	10.20	3.6×10^{-15}	2.1×10^{38}
NGC 253 ^c	1.4	0.083	blank sky	6.36	2.97	9.80	7.2×10^{-15}	5.9×10^{36}
NGC 253 ^d	1.4	0.083	blank sky	6.36	2.97	9.80	2.1×10^{-15}	1.7×10^{36}
NGC 3628	2.2	0.130	blank sky	6.06	2.83	9.39	1.5×10^{-15}	1.8×10^{37}
NGC 3079	0.8	0.047	blank sky	6.34	2.95	9.76	3.0×10^{-15}	1.0×10^{38}
NGC 4945	15.7	0.930	local	10.98	7.87	26.59	3.8×10^{-15}	6.1×10^{36}
NGC 4631	1.3	0.077	blank sky	6.67	3.12	10.29	1.4×10^{-15}	9.6×10^{36}
NGC 6503	4.1	0.242	local	9.64	5.75	21.18	8.0×10^{-15}	2.6×10^{37}
NGC 891	7.6	0.450	local	9.78	6.53	20.33	3.0×10^{-15}	3.3×10^{37}
NGC 4244	1.7	0.101	local	5.06	2.80	9.62	1.7×10^{-15}	2.8×10^{37}

NOTE.—Column (2): The foreground Galactic hydrogen column, in units of 10^{20} cm^{-2} (Dickey & Lockman 1990). (3): The optical depth at the energy of the O VIII Ly α line ($E=0.65 \text{ keV}$) equivalent to the Galactic foreground column, assuming Galactic dust-to-gas ratios and Solar abundances. The optical depth at $E=0.3 \text{ keV}$ is 5.1 times greater. (4): Method used to calculate the combined particle and X-ray background. See § 3.1.5 for details. Columns 5, 6 & 7: Observed ACIS S3 chip background surface brightness levels, given in units of $10^{-7} \text{ counts s}^{-1} \text{ arcsec}^{-2}$, for the 0.3–1.0, 1.0–2.0 and 2.0–8.0 keV energy bands. For M82 the values correspond to the ACIS I3 chip instead of the S3 chip. (8): Intrinsic 0.3–8.0 keV flux of the faintest distinguishable individual point sources, assuming a $\Gamma = 1.7$ power law spectrum, absorbed by an intrinsic hydrogen column of 10^{21} cm^{-2} in addition to the foreground Galactic column. See text for details. (9): The corresponding 0.3–8.0 keV X-ray luminosity.

^aACIS-I observations of M82, ObsIDs 361 & 1302.

^bACIS-S observation of M82, ObsID 2933.

^cNGC 253 observation ObsID 969, nucleus and disk on chip S3, northern halo on S4.

^dNGC 253 observation ObsID 790, northern halo on chip S3, disk and nucleus on S2.

have biased the interpolation, and this requirement largely controlled the width of the background annulus used. In very crowded fields (e.g. M82’s nuclear region) a background annulus width of 2 ACIS pixels ($\sim 1''$) was used, although more commonly an annular width of 8 ACIS pixels was used. In a few cases where it was impossible to create two source regions with non-overlapping background annuli, we merged nearby point sources into a single source removal region. A variety of tests were performed, using this methodology on point-source-free diffuse emission regions, that demonstrated that this procedure provided a Poisson-statistically accurate interpolation of the diffuse emission.

For spectral analysis sources detected in any of the three bands (the soft, hard and total bands described above) are excluded when creating diffuse-emission-only spectra. When making images of diffuse emission, the soft band source lists are used for any image created within the energy range 0.3 – 2.0 keV. The hard and total band source lists are used for any image created within the 2.0 – 8.0 keV energy band.

In practice, fully-automated point source detection is not perfect. In a few cases bright features in the diffuse X-ray emission were identified as point sources. Note that this is expected behavior for a wavelet-based algorithm, which looks for distinct features on a variety of spatial-scales, not just objects corresponding to the local PSF. In other cases, low S/N features that most probably are genuine point sources were missed by the source-detection algorithm. These sources became apparent only once all brighter point sources had been removed. We assessed each such feature, and removed those that appeared to be point-like based on our personal scientific judgment.

These observations are sensitive to point source fluxes of $f_X \gtrsim$ a few times 10^{-15} erg s $^{-1}$ cm $^{-2}$ in the 0.3 – 8.0 keV energy band (equivalent to a point source with a total of ~ 10 photons detected over the entire observation). If we assume that a typical point source has a power-law X-ray spectrum with a photon index $\Gamma = 1.7$, and is seen through a total absorbing column equal to the sum of the Galactic foreground (column 2 in Table 3) and a $N_H = 10^{21}$ cm $^{-2}$ column intrinsic to the host galaxy, then we are sensitive to point sources of intrinsic luminosity $\log L_X \geq 36.5 - 37.5$, depending on the distance to the galaxy and the length of the observation (Table 3). This is typically 10 – 30 times fainter than the point sources in the *ROSAT*-based studies of Read et al. (1997) and Dahlem et al. (1998).

For M82 and NGC 3079 the ACIS data probes sources two orders of magnitude fainter than the PSPC observations.

3.1.5. Background subtraction

Accurate background subtraction is vital when studying faint diffuse X-ray emission. We experimented with various methods of background level estimation and background subtraction for each observation, before settling on the methods detailed below.

Whenever possible, we use the appropriate summed blank-sky field provided as part of CIAO. We rescale the blank-sky background data set so as to match the observed 3.0 – 6.0 keV energy band count rate in the data (having excluded all point source X-ray emission when making the comparison). For M82 and NGC 253, the two brightest galaxies in the sample, we excluded the area associated with the disk of the galaxy to avoid biasing the background rescaling factor with emission due to unresolved point sources in the disk, and possible diffuse hard X-ray emission from the nuclear starburst regions (e.g. Griffiths et al. 2000). The assumption that there is negligible diffuse hard X-ray emission in the halos of these galaxies is justified on both an empirical and theoretical basis (e.g. Dahlem et al. 1998; Strickland & Stevens 2000; Strickland et al. 2002a). The background correction is performed on a chip-by-chip basis. Typically this requires a correction of $\lesssim 8\%$, in accordance with the observed long-term variation in the background rate (Markevitch 2001).

Use of the rescaled-blank sky datasets for background subtraction is appropriate only if the spectral shape of the background within each specific *Chandra* observation matches the “typical” background contained within the blank-sky fields. There are two factors that might lead to this requirement not being fulfilled. Firstly, the intensity of the soft X-ray background is known to vary by a factor ~ 2 over the sky, based on the *ROSAT* All Sky Survey measurements (Snowden et al. 1995). Secondly, the high radiation environment that *Chandra* experiences can lead to observations being taken during periods of significantly higher than normal particle backgrounds.

Using the online X-Ray Background Tool ⁵ we find the background in the summed *ROSAT* R1, R2 R4 and R5 bands (roughly the 0.12-1.21 keV energy band) for our targets deviates by at maximum 23% from the

⁵The X-Ray Background Tool can be found at <http://heasarc.gsfc.nasa.gov/cgi-bin/Tools/xraybg/>

mean background in the sample. That the variation is smaller than that found over the entire sky is to be expected, as we are observing targets generally located well out of the plane of the galaxy. In the R4+R5 band ($E = 0.47 - 1.21$ keV), which is better choice for comparison with the Chandra 0.3-1.0 or 0.6-1.0 keV energy bands (especially given the reduction in *Chandra*'s low energy sensitivity due to molecular contamination of the optical blocking filter), the extreme deviation is only $\pm 14\%$. This number is similar to the typical degree we have had to rescale the blank-sky background data.

All attempts to use rescaled blank-sky data for background subtraction of the ACIS observations of NGC 4945, NGC 6503, NGC 891 and NGC 4244 led to obvious over-or-under subtraction of the background (in particular in the soft $E = 0.3 - 1.0$ keV energy band). For the first three targets, the particle background was significantly higher than normal during a large fraction of each observation, even after the strongest background “flares” had been removed. More aggressive flare removal led to unacceptably low remaining exposure times. For NGC 4244, the *low energy* count rates over the S3 chip (once point sources had been removed) were significantly *lower* than expected based on comparison with the blank-sky fields. For these four datasets we calculated a local background surface brightness, in any particular chip and energy band, based on the sum of 2 to 3 local background regions. These regions were chosen to exclude any diffuse X-ray emission from the host galaxy, while remaining close enough to the galaxy to minimize the effect of any variation in the background over the chip. Such variations do exist, and have proved to be particularly troublesome at high energies in the ACIS observation of NGC 891, and to a lesser extent in NGC 6503 and NGC 4244 observations. Emission from all detected X-ray point sources was excluded when calculating the background count rate or surface brightness.

This local background estimate needs to be scaled appropriately when calculating the background in any other region on the chip, given that the background varies over any chip. For image-based analysis we used the relative intensity from an exposure map (the product of the effective exposure, and collecting area, at some X-ray photon energy for each point on each ACIS chip) to map from an observed local background to a chip-wide model background image. This was done on a chip-by-chip and energy band-by-energy

band basis. This method works well except when the background is high due to additional particle-based events, which are not vignettted by the telescope structure in the same way as the X-ray photons are.

For spectral analysis we do not use this exposure-map based correction, instead rescaling the background so as to achieve a net zero count rate in the point-source-subtracted halo spectra, in the 3.0 – 8.0 keV energy band. This requires a very minor correction, in all cases $\lesssim 8\%$.

For the ACIS-I observation of M82 we used local background estimation for each of the four ACIS-I chips, even though the background appears well-behaved. This observation was taken much earlier than the observation used to create the blank-sky fields, and we felt it better to use a direct, local, estimate of the background rather than attempt to re-scale the blank-sky fields. The local background regions were placed along the edges of the ACIS-I chips, again avoiding any regions of known diffuse X-ray or optical emission.

Table 3 specifies for which datasets blank-sky or local methods of background subtraction were used, along with the observed background surface brightness in the S3 or I3 chips. Simple estimates using the PIMMS count rate conversion software demonstrate that the *ROSAT*-predicted background rates in the *Chandra* 0.3–1.0 and 1.0–2.0 keV bands are lower than the background levels we find with *Chandra*, indicating that the particle contribution to the background is significant, as expected.

The accuracy of the background subtraction for each data set was checked by measuring the number of residual counts in a background-subtracted image from regions free of point source emission and any possible diffuse emission (based on visual inspection of the smoothed *Chandra* images, and comparison of any existing X-ray images from *ROSAT* observations). This was done in each of the four following energy bands, 0.3–0.6, 0.6–1.0, 1.0–2.0 and 2.0–8.0 keV. The size of these regions was in all cases between 1 – 2 square arcminutes, large enough that there were between hundred and a thousand counts due to the background in each region and in each energy band. In all data sets, and for all energies, the residual emission in these regions after background subtraction data lies within 1 standard deviation of zero. We conclude that our background subtraction methods are as good as any method that can be feasibly employed at this time.

3.1.6. Diffuse emission X-ray spectra and spectral response files

Background-subtracted spectra were manually created using the FTOOL task MATHPHA, instead of letting the XSPEC spectral-fitting program perform the background subtraction itself. This allows us to both rebin the spectra to ensure a minimum of 10 counts per bin after background subtraction (using GRPPHA), and associate more-realistic statistical errors with the data (Poisson errors instead of \sqrt{N} errors). This is necessary as the surface brightness of the diffuse X-ray emission away from the disk of these galaxies is typically at or below the background level. Thus the standard method of rebinning to a fixed number of counts per bin before background subtraction does not ensure that there will be sufficient counts per bin left after background subtraction to allow χ^2 spectral fitting.

Spectral response matrix files (RMFs) and auxiliary response files (ARFs) for the diffuse emission spectra were constructed using the CIAO tools MKRMF and MKWARF, appropriately weighted by the observed, point-source *and background-subtracted*, spatial distribution of the diffuse emission.

For those observations taken at an ACIS CCD operating temperature of -120°C (see Table 2) the standard response files from CALDB v2.12 were used. The RMF files in CALDB v2.12 for ACIS observations taken with the CCDs at -110°C are known to be significantly less accurate, in particular with respect to the energy resolution (see the discussion in § 2.1.5 of Strickland et al. 2002a). As updated responses for these observations were not available at the time analysis was performed, we instead used the responses for -120°C for these observations, which is more accurate than using the default -110°C responses.

In the case of the ACIS-I observation of M82 (the combined data from ObsIDs 361 and 1302), appropriately-weighted RMF and ARF files were created separately for each ACIS-I chip. The HEASOFT tools ADDRMF and ADDRMF were then used to combine these separate response files into the single RMF and ARF file used in the spectral fitting.

3.2. Optical narrow-band observations and data analysis

For the majority of these galaxies we have used existing, previously-published, narrow-band $\text{H}\alpha$ imaging and narrow-or-broad-band continuum imaging. For the purposes of comparing the spatial morphology and

extent of the optical emission with that of the X-ray emission, we found astrometric solutions for the optical images, typically using between 10 – 30 stars per image. Positions for these stars were taken from either the Automatic Plate Measuring (APM) survey (Maddox et al. 1990), or the U.S. Naval observatory A2.0 catalog. The astrometric solutions were calculated using the STARLINK software package ASTROM. The rms uncertainty in the absolute positions for the various optical images lies in range $\sim 0''.3 - 0''.5$. We shall present a quantitative X-ray-vs- $\text{H}\alpha$ flux comparison in a future paper.

3.2.1. Existing reduced optical data

For M82 we used optical R-band and $\text{H}\alpha$ images from the “UV/Visible Sky Gallery on CDROM” (Chen et al. 1997), originally taken on the 0.9m telescope at KPNO. The images were convolved with a Gaussian mask to achieve a common spatial resolution of $1''.5$ FWHM, prior to using the R-band image to continuum-subtract the $\text{H}\alpha$ image

The continuum R-band and continuum-subtracted $\text{H}\alpha$ images of NGC 1482 were provided by S. Hameed, and originally published in Hameed & Devereux (1999). For NGC 253 we use the 6649 Å-continuum and continuum-subtracted $\text{H}\alpha$ images originally published in Hoopes, Walterbos & Greenawalt (1996), in addition to the higher resolution R-band and $\text{H}\alpha$ images published in Lehnert & Heckman (1996) (these images are the same as those used in Strickland et al. 2002a, which gives more detail on their properties and origin). The R-band and $\text{H}\alpha$ images of NGC 3628 are those originally obtained and presented by Fabbiano et al. (1990). For NGC 3079 we use the deep $\text{H}\alpha$ image presented in Heckman et al. (1990), along with its R-band counterpart, in addition to the new images discussed below. The continuum-subtracted $\text{H}\alpha$ image of NGC 4945 is from Lehnert & Heckman (1996). The continuum image of NGC 4945 is from the Digitized Sky Survey. The continuum-subtracted $\text{H}\alpha$ and narrow-band continuum images of NGC 4631, NGC 891 and NGC 4244 are all from Hoopes et al. (1999).

3.2.2. Other optical data

Narrow-band $\text{H}\alpha$ and broad-band continuum images of NGC 3079 were obtained on the night of 2002 May 4, using the SPICAM instrument on the 3.5m Apache Point Telescope. Four 300 s narrow-band im-

ages were obtained through the 6585 Hodge filter (center 6586 Å, FWHM 22.3 Å) filter, in addition to two 60 s R-band images. The CCDPROC task in IRAF was used to perform standard overscan, bias subtraction, and flat-fielding corrections and cosmic ray rejection. The images were convolved with a Gaussian mask to achieve a uniform resolution of 1''4 FWHM prior to continuum subtraction. The R-band image was subtracted off the median-combined narrow-band images, scaled so as to leave zero residual emission associated with foreground Galactic stars. This continuum-subtracted H α image has superior spatial resolution to the more sensitive image from Heckman et al. (1990).

For NGC 6503 we obtained and reduced a dataset from the Isaac Newton Group (ING) telescope archive. The observation was taken with the 1.0m Jacobus Kapteyn Telescope on La Palma on 1999 April 25. The same form of data reduction used on the NGC 3079 data was applied. The final effective resolution of the H α and R-band images is 1''5.

4. Spatial analysis

4.1. X-ray and optical images

Figures 2 to 13 show soft and hard X-ray, optical R-band and continuum-subtracted H α images of all the galaxies in our sample. A common X-ray surface brightness scale and physical region size (2 kpc, and 20 kpc square) is used, as this provides a fairer comparison of the relative brightness of the extra-planar diffuse emission between the various galaxies.

In many cases the images are composites of data from several ACIS chips — generally the ACIS S2, S3 & S4 chips (ACIS I0, I1, I2 & I3 for the ObsID 361 + 1302 observations of M82) — chips which have different sensitivities as a function of photon energy. To obtain a chip-and-instrument-independent measure of the X-ray surface brightness we build an image in any broad energy band out of several images from narrower energy bands, appropriately weighted by the effective area of the instrument for that sub-energy and chip-type (created using the CIAO task MKEXPMAP). This weighting is done after background (and any point-source) subtraction. Finally, exposure times and pixel sizes are taken into account to create an image in units of photons s⁻¹ cm⁻² arcsec⁻², *i.e.* an estimate of the X-ray photon flux in that energy band immediately *prior* to passing through the telescope’s optics. For example, each exposure-corrected 0.3–2.0 keV energy band image is built out of exposure-map-correct im-

ages in the 0.3–0.6, 0.6–1.0, 1.0–1.5 and 1.5–2.0 keV energy bands. Inspection of the results of this procedure in cases where we have separate front-illuminated and back-illuminated chip exposures of the same object (e.g. M82, the disk and northern halo of NGC 253) shows that it works well, even when relatively broad sub-energy bands are used (we use 0.3 and 0.5 keV-wide bands for $E < 2$ keV, and 2 keV-wide bands for $E > 2$ keV).

The X-ray images in Figs. 2 to 13 have been adaptively smoothed to achieve a *local* S/N ratio of 3. In some images, weak CCD-chip artifacts appear that proved impossible to totally remove. These occur most noticeably along the edges of the chips. The gaps between the chips are also visible, most notably in the ACIS-I observations of M82. For convenience we have labeled these features with “CA” (chip artifacts) and outline the individual CCD chips with dotted lines.

We have not made any effort to show the optical R and H α images on a common surface brightness scale in this paper. Instead, we have chosen the minimum and maximum intensities to highlight specific features — in the case of the R-band image to show the distribution of stellar light and/or dust lanes, and in the case of the continuum-subtracted H α images to show the extra-planar emission. The location of the *Chandra* ACIS chips is also marked on the optical images.

4.2. Notes on individual galaxies

These are currently the highest resolution X-ray images of these galaxies yet obtained, the first from which the point source contribution can be largely removed, and they are likely to remain the only X-ray data with spatial resolution comparable to ground based optical imaging for the foreseeable future. We therefore believe it worthwhile to describe the morphology of the diffuse X-ray emission we find, and its relationship to the previously observed properties of these galaxies.

In some cases the *Chandra* data confirms the conclusions observers reached based on lower spatial resolution *Einstein*, *ROSAT* HRI, PSPC and *ASCA* data, while in other cases a revision of ideas is necessary. In many cases structure is found within the diffuse emission on all spatial scales down to the limits imposed by the combination of the photon statistics and the ACIS PSF.

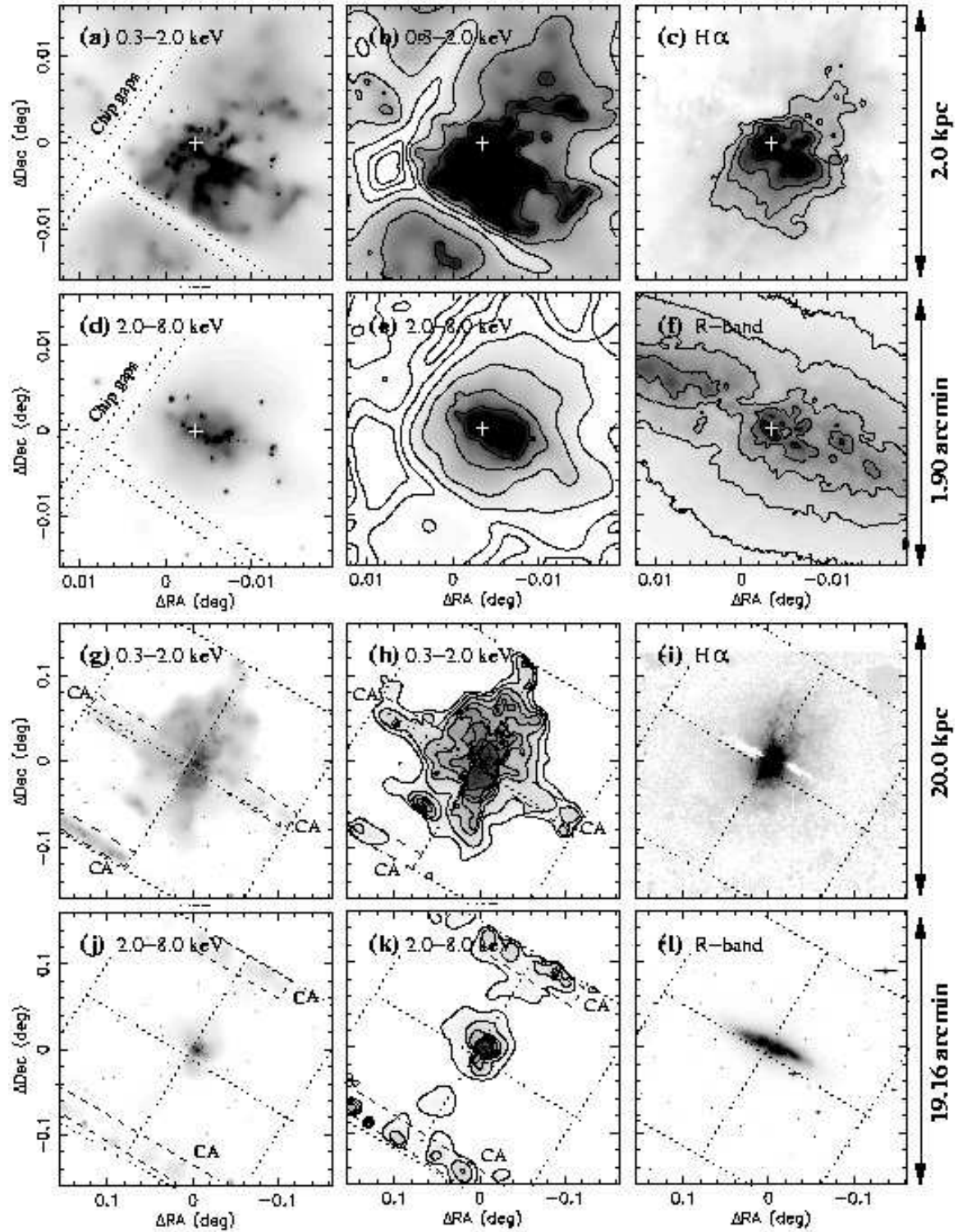


Fig. 2.— *Chandra* X-ray and optical images of M82 (the ACIS-I observations). Panels a through f display the central 2 kpc of M82, with the dynamical center of the galaxy at the exact center of each image (caption continued overleaf).

Fig. 2.— (continued). The nuclear region X-ray images, which include X-ray emission from point sources, (plots a & d) are shown on a square-root intensity scale, from a surface brightness of 1×10^{-8} counts s^{-1} cm^{-2} $arcsec^{-2}$ (white) to 1×10^{-5} counts s^{-1} cm^{-2} $arcsec^{-2}$ (black). Contours are shown in intervals of 0.5 dex, between 2×10^{-9} and 6×10^{-7} counts s^{-1} cm^{-2} $arcsec^{-2}$. Images of the diffuse X-ray emission (*i.e.* all point sources removed) from the central 2 kpc (plots b & e) are also shown on a square-root intensity scale, from a surface brightness of 1×10^{-8} counts s^{-1} cm^{-2} $arcsec^{-2}$ (white) to 1×10^{-6} counts s^{-1} cm^{-2} $arcsec^{-2}$ (black). Contours are shown in intervals of 0.5 dex, between 2×10^{-9} and 6×10^{-7} counts s^{-1} cm^{-2} $arcsec^{-2}$. Continuum-subtracted $H\alpha$, and R-band images, are shown in panels c & f, respectively. The images are shown using a square-root intensity scale between arbitrary surface brightness levels. The position of the nucleus cited in Table 1 is marked by a black-or-white cross in panels a through f. Panels g through l are similar to panels 1 through f, but cover a 20×20 kpc region. Again, all plots are shown on a square root intensity scale. The contour levels for the X-ray images are the same as in panels a, b e & f, although the gray-scale is shown between different surface brightness levels. In panels g & j (X-ray emission including the point source contribution), the gray-scale displays surface brightnesses between 1×10^{-9} (approximately half the background level) and 1×10^{-5} counts s^{-1} cm^{-2} $arcsec^{-2}$. Panels h & k (diffuse X-ray emission only), the gray-scale displays surface brightnesses between 1×10^{-9} (approximately half the background level) and 1×10^{-6} counts s^{-1} cm^{-2} $arcsec^{-2}$. Note that all X-ray images have been background subtracted. Artificial linear features in the X-ray images due to hot columns near the CCD node boundaries are marked CA (chip artifact), in the cases where they could not be completely removed in the data processing. The location of the edges of the ACIS CCD chips are marked with thin dotted lines, and these locations are repeated on the optical images to ease cross-comparison between the X-ray and optical images.

4.2.1. M82

Both the diffuse and point-source X-ray emission are sharply concentrated within the central ~ 900 pc, coincident with the central starburst region (e.g. Muxlow et al. 1994; Golla, Allen & Kronberg 1996; Förster Schreiber et al. 2001). The brightest pillars or filaments of diffuse soft X-ray emission emerge perpendicular to the plane of the galaxy, toward the south east (Figs. 2b, 3b). The diffuse emission to the north west is fainter, consistent with absorption by the intervening disk. In general, X-ray and $H\alpha$ emission to the NW of the major axis is fainter than that to the SE of the plane, as expected based on the inclination of the galaxy. Two relatively narrow X-ray-and- $H\alpha$ bright nuclear filaments to the north west of the nuclear disk are notable as they also appear in the R-band image (Fig. 2f). This is most probably due to the inclusion of $H\alpha$ line emission in the R-band, as B-band images show no similar structures.

On the larger scale, the ACIS images of the diffuse emission show few differences from ROSAT HRI and PSPC images (Bregman, Schulman & Tomisaka 1995; Strickland, Ponman & Stevens 1997). The filamentary nature of the brighter diffuse emission is more apparent in the higher resolution, higher sensitivity ACIS images than in the old ROSAT HRI images (Shoppell & Bland-Hawthorn 1998). As with NGC 253, the soft X-ray emission resembles the $H\alpha$ emis-

sion on all scales.

Surrounding the filamentary X-ray emission is lower surface brightness diffuse emission, which appears more uniformly distributed. The larger spatial extent and greater uniformity might be purely an artifact of lower photon statistics and heavier smoothing. However, there is a smooth component of the $H\alpha$ emission (Bland & Tully 1988) with a similar spatial extent (e.g. see Fig. 2i). The smooth $H\alpha$ component is predominantly dust-scattered nuclear light, given its polarization (Schmidt, Angel & Cromwell 1976; Bland & Tully 1988), so the conditions in the dusty medium and the X-ray emitting plasma must be somewhat distinct from that in the X-ray-and- $H\alpha$ bright filaments.

The *Chandra* data also show diffuse X-ray emission associated with the faint northern $H\alpha$ filaments that stretch between the main X-ray/ $H\alpha$ nebula ($0 < z$ [kpc] $\lesssim 5$), and the northern “cloud” or “cap” (at $z \sim 11$ kpc, see Devine & Bally 1999; Lehnert et al. 1999. The northern cloud is not visible in Figs. 2 and 3, as it lies just beyond the top of these figures.).

To the south of the galaxy the diffuse X-ray emission can be traced out to a distance of ~ 7 kpc below the plane of the galaxy, only slightly further than seen with ROSAT. A notable feature is a bright arc of diffuse X-ray emission, detached to the east of the main southern outflow (centered at $\alpha = 09^h 56^m 38^s.3$, $\delta = +69^\circ 37' 47'' 6$, J2000.0, see Fig. 2h), possibly associated with faint $H\alpha$ emission at the same location

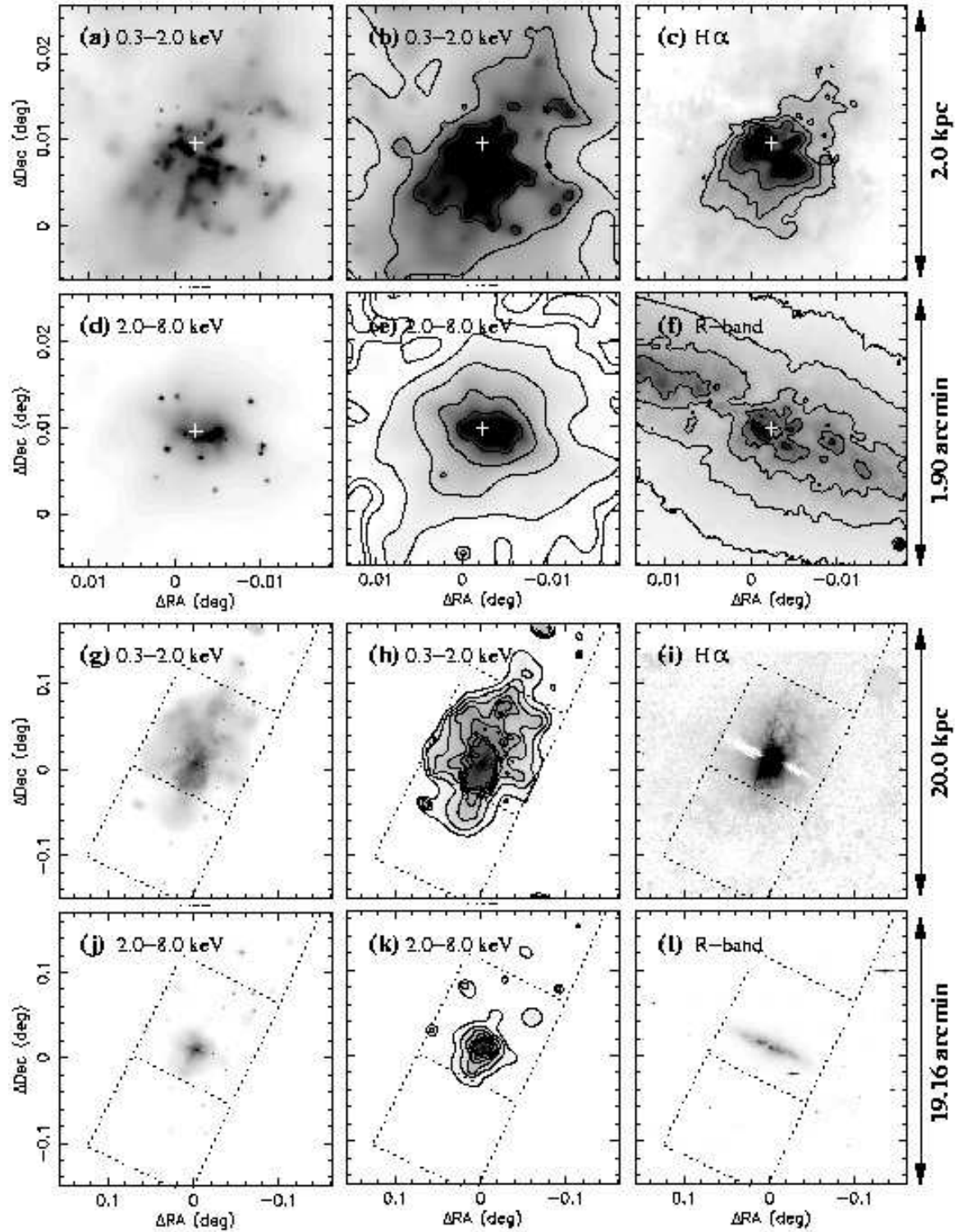


Fig. 3.— *Chandra* X-ray and optical images of M82 (the ACIS-S observation). The meaning of each panel, and the intensity scales and contour levels used, are the same as those described in Fig. 2.

(Fig. 2i). Given the apparent sharpness of the eastern edge of the southern outflow, the presence of this diffuse feature further to the east is interesting. This feature is not associated with any of the tidal HI streamers around M82 (Yun, Ho & Lo 1993). The origin of this structure may be similar to that of the northern cloud discussed in Lehnert et al. (1999).

The diffuse hard X-ray emission, discovered by Griffiths et al. (2000), is preferentially extended along the major axis of the galaxy at high X-ray surface brightness (Figs. 2e, 3e). However, at lower surface brightness it appears to also participate in the minor axis outflow (see also Figs. 2k and 3k).

There is no obvious enhancement in the diffuse X-ray emission, in either the soft or hard energy bands, associated with the locations of the 4 expanding HI shells described by Wills, Pedlar & Muxlow (2002). Several of the brighter X-ray point sources lie within the confines of Wills et al.'s shell 3 (previously detected in CO emission, see Weiss et al. 1999; Matsushita et al. 2000). It is worth noting that the off-nuclear intermediate luminosity X-ray object (Kaaret et al. 2001; Matsumoto et al. 2001) lies *outside* shell 3, weakening the argument by Matsushita et al. (2000) that the two are related.

4.2.2. NGC 1482

NGC 1482 is a IR-warm starburst galaxy, of similar mass and size to that of M82, located at a distance of approximately 22 Mpc. Given its southern declination, and only moderate inclination ($i \sim 58^\circ$), it has escaped serious observational attention until recently. Hameed & Devereux (1999) first pointed out the spectacular extra-planar $H\alpha$ filamentation (e.g. Fig. 4i), prompting both our *Chandra* observation (the first published X-ray study of this galaxy), and an optical spectroscopic investigation by Veilleux & Rupke (2002) that confirmed the presence of a ~ 250 km/s outflow. There is no sign of any AGN activity, its optical spectroscopic classification being that of a standard HII galaxy (Kewley et al. 2001).

The star formation appears to be concentrated in a ~ 1 kpc-diameter nuclear disk, based on the location of both the $H\alpha$ emission and the hard X-ray emission (Fig. 4c & d). In the soft X-ray band (0.3–2.0 keV), a well collimated, limb-brightened outflow emerges to the south of the nucleus (the beginnings of which can be seen in Fig. 4b), and extends out to $z \sim 5$ kpc below the plane of the galaxy (Fig. 4h), before disappear-

ing at approximately the same location at which the $H\alpha$ emission disappears (Fig. 4i). The overall morphology is that of the archetypal superwind – a limb-brightened cone truncated at its base in the disk of the galaxy.

The northern outflow is very similar in morphology and size, although both the X-ray and $H\alpha$ emission from the innermost kiloparsec is heavily absorbed by the strong dust lane that is visible in the R-band image (Fig. 4l) of the galaxy.

Close inspection of unsmoothed images shows that the soft X-ray emission is very similar in morphology to the $H\alpha$ emission, and displays the same limb-brightened truncated conical geometry, despite the filled-in appearance of the smoothed X-ray images presented in Fig. 4. We will present a more detailed comparison of the X-ray emission with the $H\alpha$ emission in a future paper.

The surface brightness of the diffuse soft X-ray emission is higher than in the majority of the galaxies in this sample, and is very similar to that of the diffuse emission from M82.

4.2.3. NGC 253

NGC 253, the most massive galaxy in the Sculptor group (Puche & Carignan 1988), hosts a compact nuclear starburst, although recent star-formation is also widespread throughout the disk (Ulvestad & Antonucci 1997; Engelbracht et al. 1998; Sofue et al. 1994; Ulvestad 2000). At a distance of only ~ 2.6 Mpc, it is the closest massive galaxy undergoing a starburst. It has been heavily studied at X-ray wavelengths, originally with *Einstein* (Fabbiano & Trinchieri 1984). Lacking any obvious nearby companion galaxy, the original cause of the starburst activity is a mystery.

Figs. 5 and 6 display both *Chandra* X-ray and optical images of NGC 253. In general the morphology and surface brightness of the diffuse emission is consistent between the two observations. The only significant exception to this is the apparently diffuse hard X-ray emission filling the S3 chip in the shorter observation (Fig. 5k). This is undoubtedly an artifact, as such hard diffuse emission is not detected in the S2 chip which covers this location in the longer observation (see Fig. 6k), and is due to the excess background emission in the S3 chip discussed in Strickland et al. (2002a).

We refer the reader to Strickland et al. (2000),

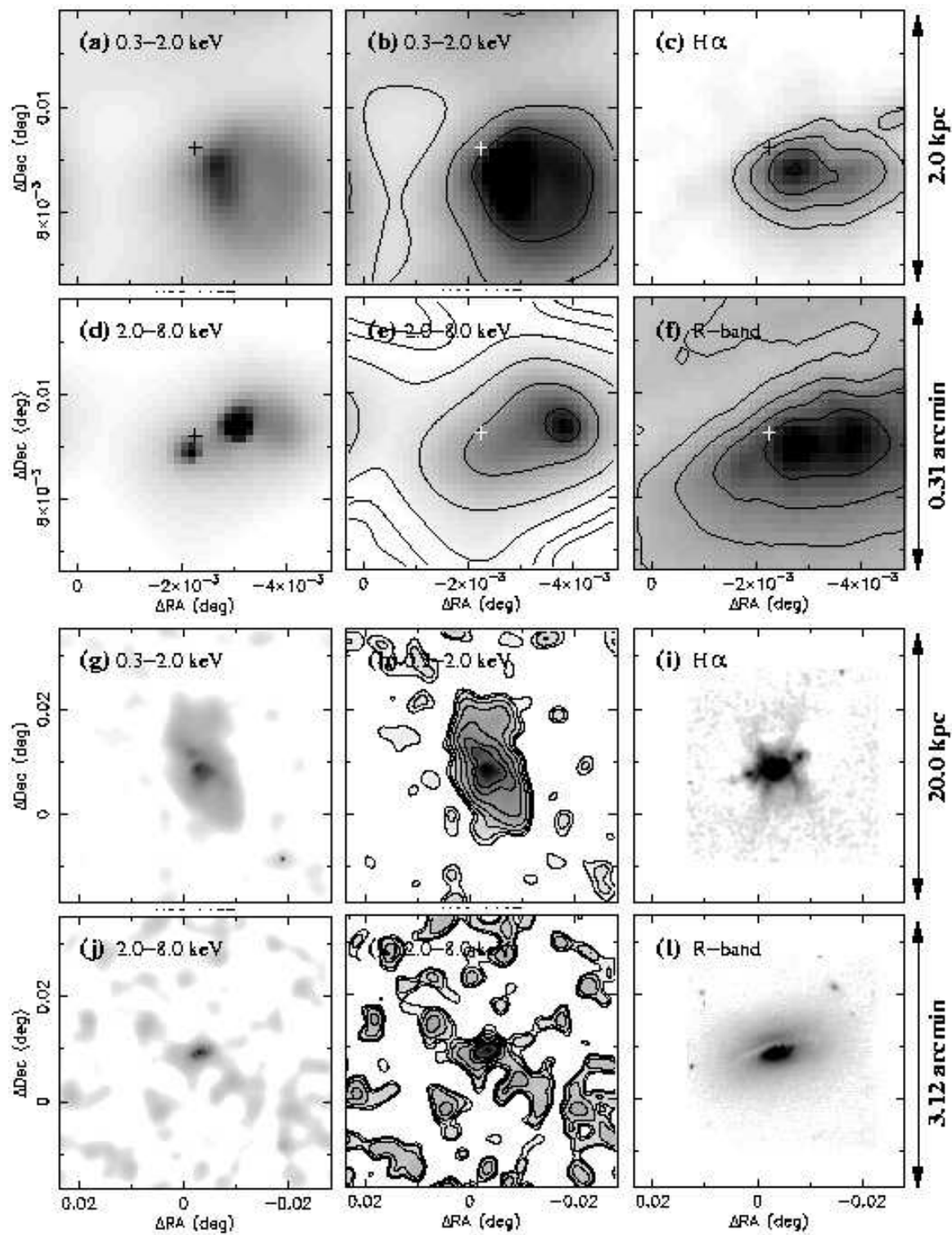


Fig. 4.— *Chandra* X-ray and optical images of NGC 1482. The meaning of each panel, and the intensity scales and contour levels used, are the same as those described in Fig. 2.

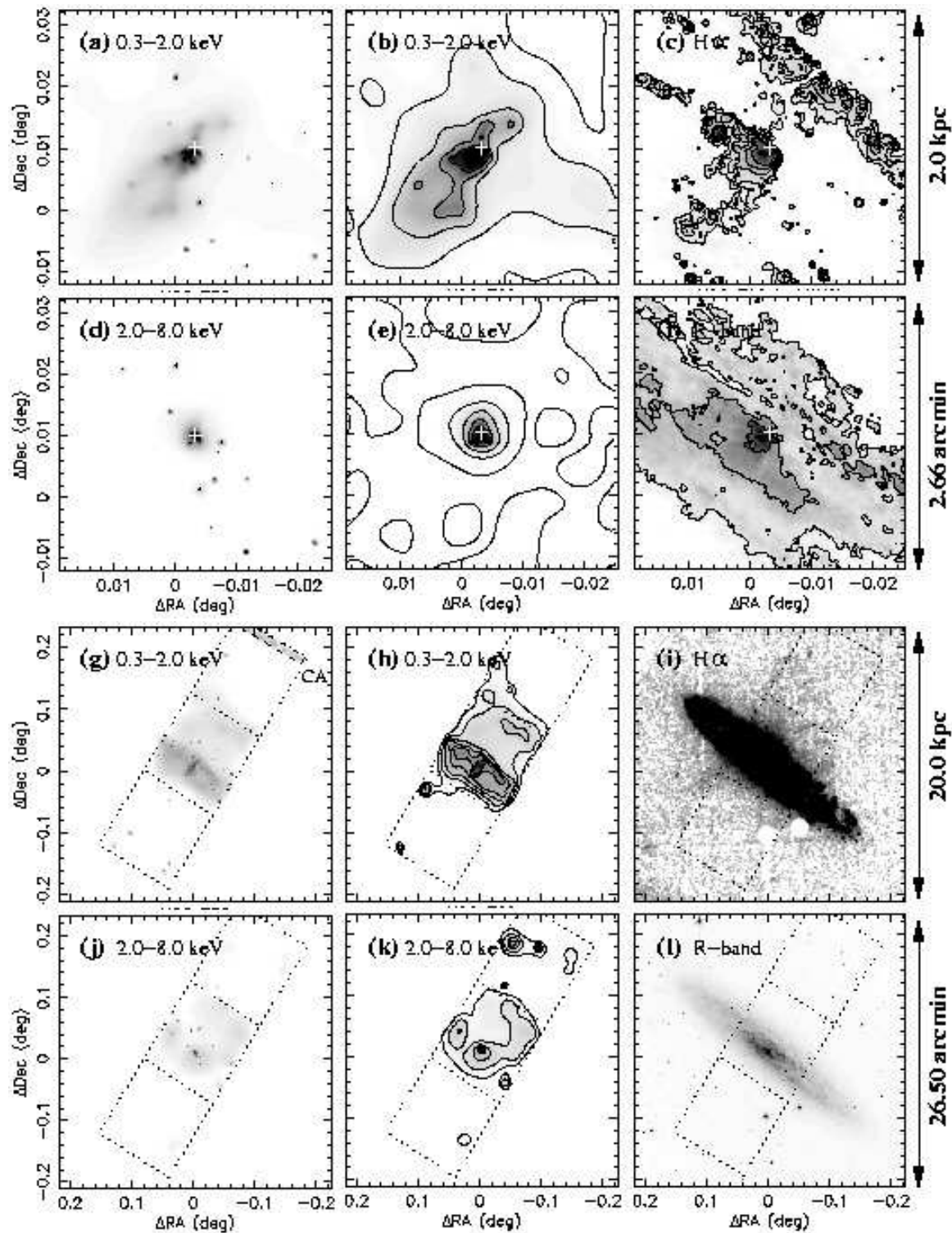


Fig. 5.— *Chandra* X-ray and optical images of NGC 253 (ObsID 969). The meaning of each panel, and the intensity scales and contour levels used, are the same as those described in Fig. 2. The diffuse hard X-ray filling the majority of the S3 chip in panel k is an artifact (see § 4.2.3).

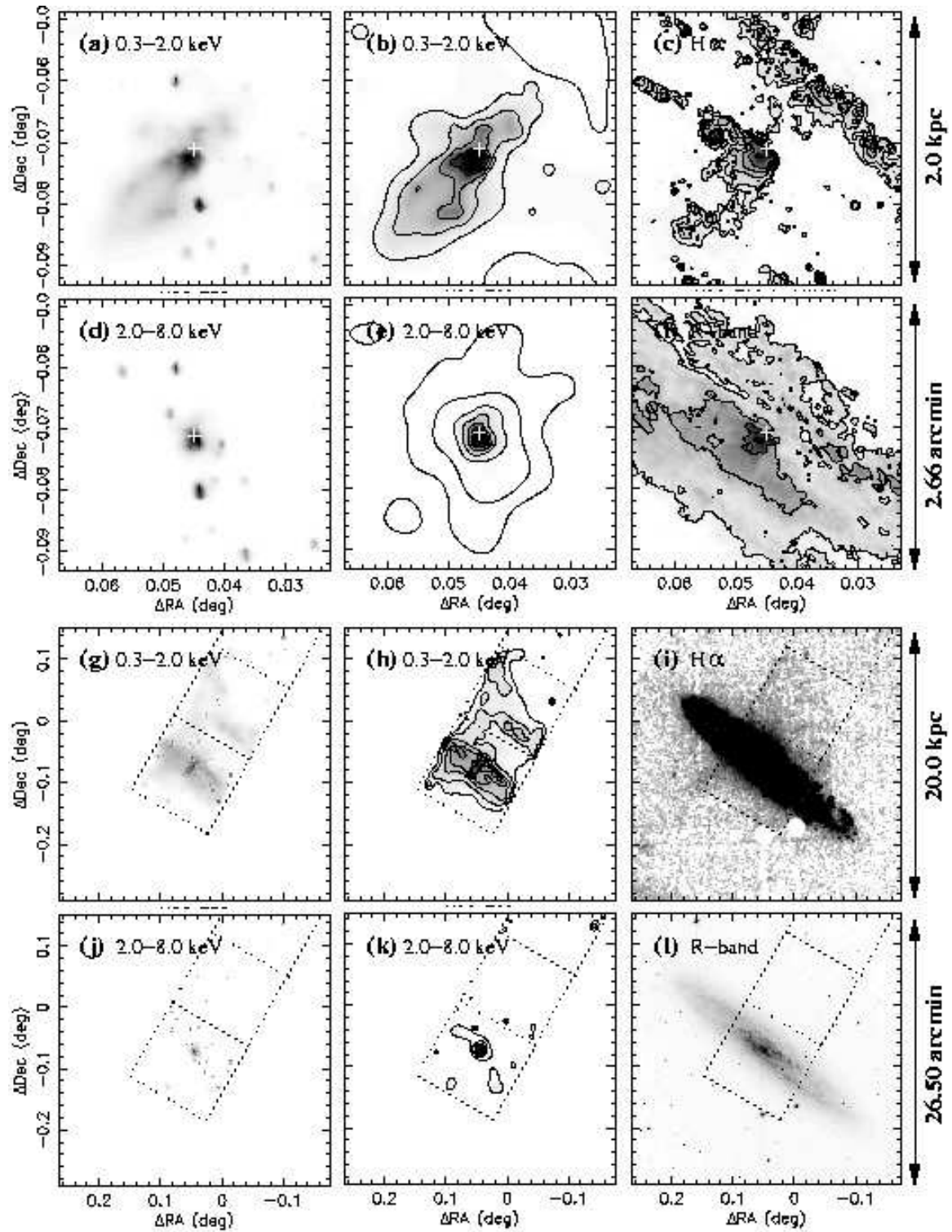


Fig. 6.— *Chandra* X-ray and optical images of NGC 253 (ObsID 790). The meaning of each panel, and the intensity scales and contour levels used, are the same as those described in Fig. 2.

Strickland et al. (2002a) and Weaver et al. (2002) for detailed presentation and discussion of the *Chandra* observations of NGC 253.

4.2.4. NGC 3628

NGC 3628, a member of the Leo triplet, hosts a compact nuclear star-forming disk, approximately 300 pc in diameter based on the non-thermal radio emission from young supernovae (Carral, Turner & Ho 1990; Irwin & Sofue 1996; Zhao et al. 1997; Cole, Mundell & Pedlar 1998), although the star-formation rate is high within the entire central kiloparsec (e.g. Irwin & Sofue 1996). An optical and HI tidal arm extends ~ 100 kpc to the east of NGC 3628 (Kormendy & Bahcall 1974; Rots 1978; Haynes, Giovanelli & Chincarini 1984), evidence of a close interaction between NGC 3628 and NGC 3627 approximately 800 Myr ago, based on the modeling of Rots (1978). A very distinct boxy/peanut-shaped bulge suggests a bar may be present.

The *Chandra* X-ray observations (Fig. 7) reveal a wealth of detail, generally in agreement with the *Einstein* and *ROSAT* observations of Fabbiano et al. (1990), Read et al. (1997) and Dahlem et al. (1996).

We find extended hard X-ray emission associated with the optically-obscured nuclear starburst region (Fig. 7d & 7e). The major-axis spatial extent of this emission ($\sim 8''$) is similar to the $6''$ -diameter ridge of 1.4 GHz (Cole et al. 1998) and 15 GHz radio emission (Carral et al. 1990). The nuclear hard X-ray emission is most likely predominantly a blend of spatially-unresolved high-mass X-ray binaries, rather than genuinely diffuse emission. The relative faintness of the nuclear emission, as compared to other binaries seen in projection within the central 2 kpc, is no doubt related to the high absorbing column density toward the nucleus.

Relatively bright, but patchy, $H\alpha$ emission extends $\sim 10''$ (~ 450 pc) to both the north and south of the location of this nuclear disk (Fig. 7c). We speculate that this is emission from a well-collimated nuclear outflow, seen along sight-lines of lower than normal obscuration. The *Chandra* data supports this hypothesis, as we also see diffuse soft X-ray emission in the same region (Fig. 7b), again preferentially extended along the minor axis. The adaptive smoothing applied to Fig. 7b tends to destroy details of the structure of the diffuse emission. In the un-smoothed pixel maps the diffuse soft X-ray emission clearly separates into

two approximately rectangular regions, separated from each other by a $\sim 3''$ thick soft-X-ray-dark region, corresponding spatially to the starburst region. The region to the north the nucleus is $\sim 8''$ wide (~ 390 pc), and extends $\sim 12''$ (~ 580 pc) to the NNE along the minor axis. The southern region has a similar major-axis extent, but only extends $\sim 5''$ (~ 250 pc) to the SSW. The northern rectangle or cylinder is the brighter of the two, consistent with the commonly-assumed geometry of NGC 3628, which is that the disk of NGC 3628 is inclined so we see its northern face. These structures are likely to be analogous to the nuclear outflow cones seen in NGC 253 and NGC 4945.

On the larger scale (panels g to l in Fig. 7), diffuse soft X-ray emission is again found in association with $H\alpha$ emission, within the limited field of view of the $H\alpha$ image. To both the north and south of the disk, the western-most edge of the diffuse emission is the brightest. There is suggestive evidence for a eastern limb to the X-ray emission in both the north and south, *i.e.* a bi-polar, limb-brightened, cavity somewhat similar to an open-ended hourglass in morphology (dashed and dotted lines have added to Fig. 7 to guide the reader these faint features, and the others we describe below).

The X-ray emission to the south of the optical disk of the galaxy is brightest in the region bounded by the ~ 4 kpc-long $H\alpha$ filament discovered by Fabbiano et al. (1990) (for a clearer presentation of this, see Fig. 3 in Strickland 2002). This X-ray-plus- $H\alpha$ filament is very similar to the ~ 650 pc-long filament 6 in the dwarf starburst NGC 1569 (Martin, Heckman & Kobulnicky 2002). This filament appears to join the disk of the galaxy $20''$ (1.0 kpc) to the west of the nucleus, although the inclination of the galaxy makes the location of the filament at heights $z \lesssim 1$ kpc of the plane uncertain. To the east of the nucleus, extra-planar $H\alpha$ filamentation is less pronounced, and can only be traced with confidence to ~ 2 kpc south of the plane. Diffuse soft X-ray is present within this region, but lacks any clearly developed limb/filament of the sort found on the western limb.

On the northern side of the galaxy the $H\alpha$ emission appears in the form of a series of faint ≤ 2 kpc-long filaments, primarily above the nucleus and to the west of the nucleus. The westernmost extent of the $H\alpha$ emission coincides with a bright H II complex $\approx 40''$ (≈ 2 kpc) to the west of the nucleus. Extra-planar diffuse X-ray emission is relatively bright above this region. East of the nucleus, the lack of significant extra-planar

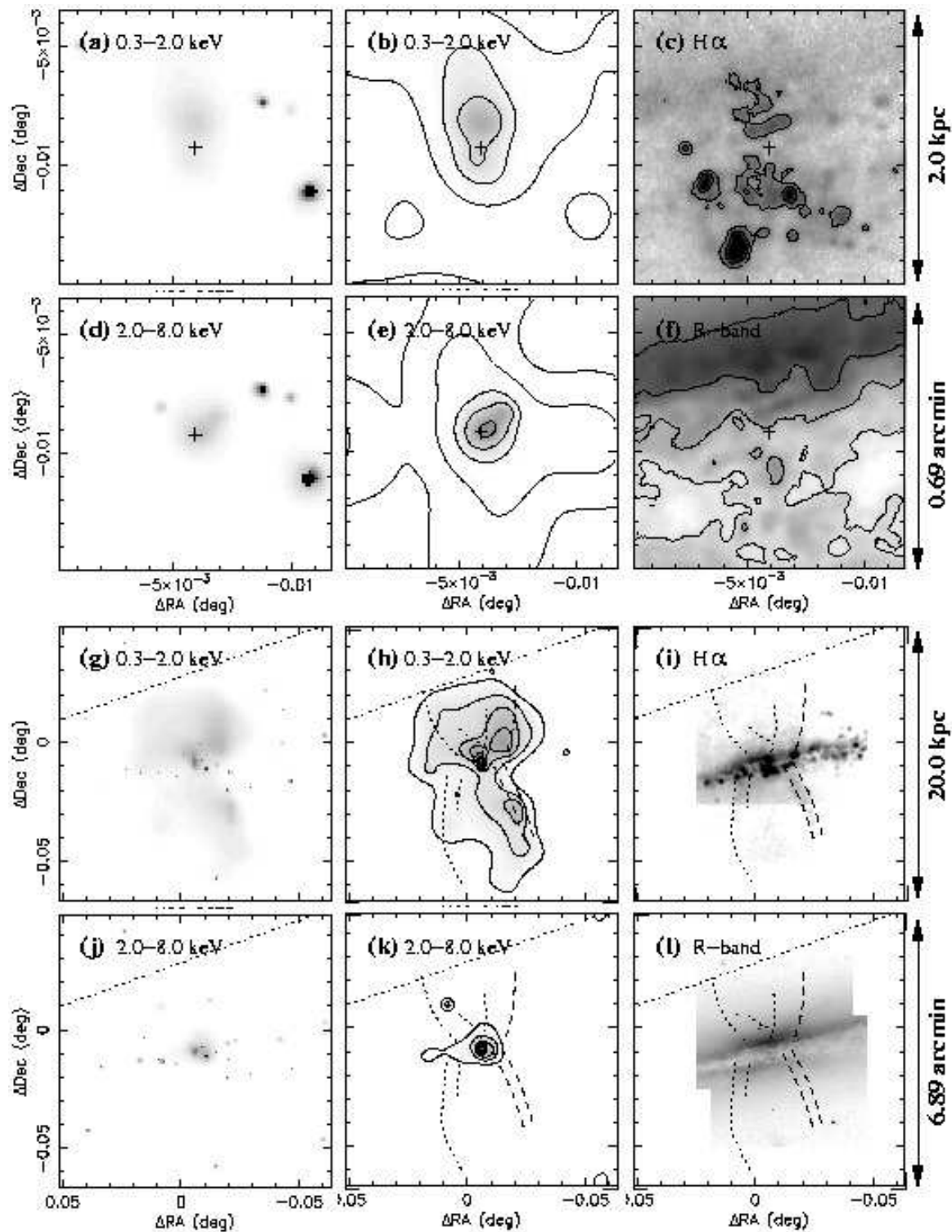


Fig. 7.— *Chandra* X-ray and optical images of NGC 3628. The meaning of each panel, and the intensity scales and contour levels used, are the same as those described in Fig. 2. The dashed and dotted arcs marked on panels h, i, k, and l are intended to draw the reader’s eye to the features discussed in § 4.2.4.

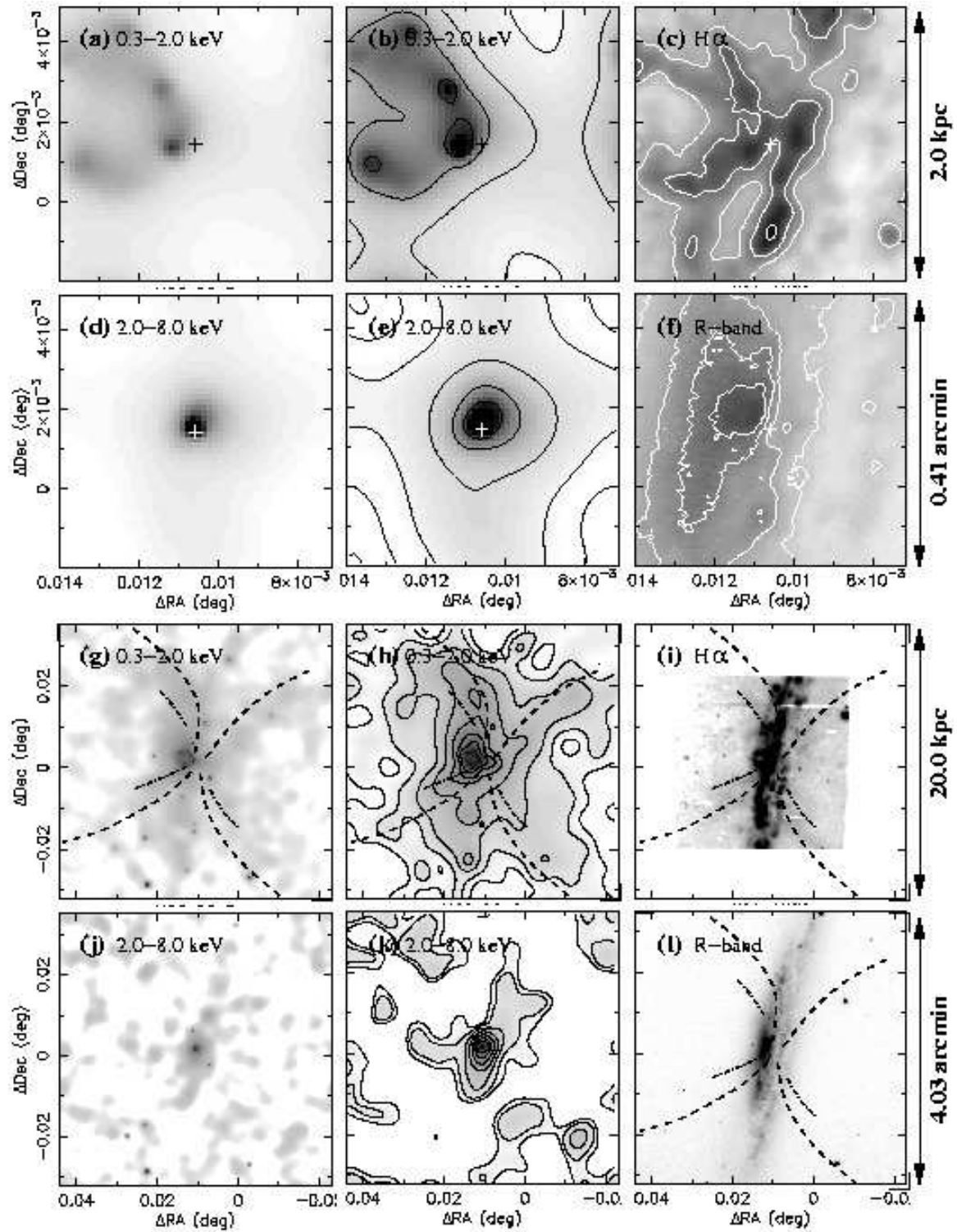


Fig. 8.— *Chandra* X-ray and optical images of NGC 3079. The meaning of each panel, and the intensity scales and contour levels used, are the same as those described in Fig. 2. The arced dashed lines marked on panels h, i, k, and l are intended to draw the reader’s eye to the features discussed in § 4.2.5.

H α emission is matched by a similar lack in diffuse X-ray emission.

It is interesting to note that the base of the eastern and western edges of the extra-planar H α and X-ray emission is similar to the maximum extent of the box-shaped bulge seen in optical continuum images, which may be related to a bar (see e.g. Irwin & Sofue 1996; Cole et al. 1998).

What is the cause of the pronounced east/west emission asymmetry? Jonathan Bland-Hawthorn (2000, private communication) has suggested that some of the asymmetry in the M82 wind, in particular the apparent $\sim 10^\circ$ bending of the flow away from the minor axis, might be due to ram pressure acting on the wind as M82 moves through the inter-group medium. If NGC 3628 is moving primarily to the west, then ram pressure confinement or compression would lead to higher gas densities on the western side of the wind, and hence produce the higher H α and X-ray surface brightness that is seen. Unfortunately, NGC 3628's motion within the Leo triplet is unknown, as only kinematic model of the Leo triplet (Rots 1978) deals with the relative motion of NGC 3627 with respect to NGC 3628.

With the higher sensitivity, and better point source rejection afforded by the use of *Chandra*, we robustly trace the diffuse emission out to $\sim 2'.4$ (~ 7.0 kpc) to the north and $\sim 3'.7$ (~ 10.8 kpc) to the south of the disk. The maximum major-axis width of the emission is $\sim 3'.7$ in the north, and slightly less to the south.

The diffuse X-ray emission to the north of the disk may extend even further from galaxy (beyond the outermost contour in Fig. 7h), out to $\sim 5'.0$ (~ 14.6 kpc), at low surface brightness, but the signal-to-noise is low, given that this region lies on the lower sensitivity front-illuminated S2 chip.

The ability to robustly remove unrelated X-ray point sources makes much more of a difference to determining the morphology and extent of the diffuse X-ray emission in NGC 3628, than it does in nearer objects such as M82 and NGC 253. Our large-scale diffuse emission image is closest in resemblance to the smoothed point-source-subtracted *ROSAT* PSPC image of Read et al. (1997). Many of the features in the images of Fabbiano et al. (1990), and the ostensibly point-source-subtracted images of Dahlem et al. (1996), are due to background point sources⁶. Conse-

⁶We note in passing that the *Chandra* data shows no connection between the diffuse emission and a $z = 2.15$ AGN, claimed by Arp et al. (2002) based on heavily smoothed *ROSAT* PSPC data (see Hard-

castle 2000 for a discussion of statistical inference from smoothed images). Note that the $z = 2.15$ AGN lies outside the field of view of Fig. 7 panels g to l, which contain the full extent of the diffuse X-ray emission. Nor does the diffuse X-ray emission correlate with the "chain of optical objects" discussed in that paper. Only one object from the region of the optical chain that lies within the projected region of diffuse X-ray emission, the $z = 0.995$ AGN, has an X-ray counterpart. The chance of finding an X-ray source this bright ($f_x \sim 3 \times 10^{-14}$ erg s $^{-1}$ cm $^{-2}$ in each of the soft and hard energy bands), within the $220'' \times 320''$ area covered by the diffuse X-ray emission, is 20 to 40% (based on the soft and hard-band point source luminosity functions published in Giacomoni et al. 2001), which makes it most likely that this is a chance superposition.

4.2.5. NGC 3079 (and NGC 3073)

NGC 3079 is a massive spiral galaxy with a LINER nucleus (Heckman 1980), and is home to both vigorous disk-wide star-formation (as evidenced by the high values of the IRAS 60 μ m to 100 μ m flux ratio throughout the optical disk, see Mayya & Rengarajan 1997, in addition to Seaquist, Davis & Bignell 1978; Veilleux et al. 1994; Braine et al. 1997) and a weak AGN with a pc-scale radio jet (e.g. Irwin & Seaquist 1988; Trotter et al. 1998; Sawada-Satoh et al. 2000). Direct radio detection of young SN remnants in the nuclear region (as found in other galaxies with nuclear starbursts such as M82, NGC 253 and NGC 3628) is currently lacking, although this may be mainly due to a combination of the greater distance of NGC 3079 as compared to these other starbursts, and the general focus of radio studies on the nuclear radio source and the probable radio jet. Nevertheless, there is good observational evidence pointing to recent star-formation within the molecular-gas-rich central few hundred pc (Armus et al. 1995; Israel et al. 1998).

We originally targeted NGC 3079 as part of a program seeking to ascertain whether the close spatial correlation between X-ray and H α emission found in the southern NGC 253 nuclear outflow cone (Strickland et al. 2000) is a general feature of all superwinds. NGC 3079 was known to have an outflowing, kiloparsec-scale, limb-brightened optical emission line bubble (Ford et al. 1986; Heckman et al. 1990; Filippenko & Sargent 1992; Veilleux et al. 1994), subsequently dramatically imaged by the HST WFPC2 (Cecil et al. 2001), and there was suggestive evidence for bright structured diffuse X-ray emission in the same region from *ROSAT* HRI observations (Dahlem et al. 1998;

Pietsch et al. 1998).

The *Chandra* observations of NGC 3079 show that the diffuse X-ray emission is very closely associated with the optical filaments forming the bubble – the lower half of which can be seen in the left hand side of Fig. 8 panels a and c (see Strickland et al. (2003) for a direct overlay of the X-ray emission on the H α emission, or Cecil, Bland-Hawthorn & Veilleux (2002)⁷ for a comparison to both the HST images and the radio emission). Note that the 1.5 kpc-scale radio lobes, the only large-scale-feature unambiguously associated with the AGN, are offset from the X-ray/H α bubble (see Fig. 3 in Cecil et al. 2002). The lack of any clear correlation, or anti-correlation, between the bubble and the radio lobes strongly suggests that they are unrelated and spatially distinct phenomena, the partial overlap being due to projection.

On the larger scale, the diffuse X-ray emission is brightest along a set of 10-kpc-scale arcs that define a roughly X-shaped structure centered on the nucleus (see Fig 8h) — a structure visible in the lower signal-to-noise *ROSAT* PSPC data (Read et al. 1997; Dahlem et al. 1998; Pietsch et al. 1998). Comparison with the continuum-subtracted H α image taken by Heckman et al. (1990, – see also Fig 8i) demonstrates that the X-ray arcs or filaments correspond closely to the location of the multi-kpc-scale X-shaped optical filaments discovered by Heckman et al. The NGC 3079 observations were one of the shorter exposures in the sample, and consequently the higher noise level is visible in the hard X-ray images (Fig. 8j and k)

Diffuse soft X-ray emission almost completely fills the 20×20 kpc-scale boxes shown in Fig 8 panels g through l. The diffuse X-ray emission is easily traced

⁷The X-ray fluxes, emission integrals, luminosities, and other derived physical properties of the X-ray-emitting gas quoted in Cecil et al. (2002) are incorrect. For example, in the region they define as the bubble, the absorption-corrected intrinsic 0.1-6.5 keV energy band X-ray flux is $f_X \approx 2 \times 10^{-13}$, a factor 400 lower than the value Cecil et al. quote, but consistent with the value expected based on the count rate within the older ROSAT HRI observations (e.g. Pietsch et al. 1998). We find a best-fit emission integral for this bubble region $EI = n_e n_H \eta_X V = 5 \times 10^{62} (D/17.1 \text{Mpc})^2 \text{cm}^{-3}$, again much lower than the 10^{66}cm^{-3} given in Cecil et al. (2002), which implies the electron densities, gas masses, pressures and energy content are ~ 50 times lower than their quoted values. The flaw in their analysis can not be explained as a simple error in recording the value of a model normalization, as the spectral model they describe fails to match the shape of the observed spectrum. This pattern is typical of the use of an inconsistent set of spectral response files. A further problem is that many of the physical properties quoted in Cecil et al. (2002) also incorrectly state the dependence on the volume filling factor of the hot gas η_X .

to $\sim 140''$ (~ 11.6 kpc) above the disk (to the east) and $\sim 130''$ (~ 10.8 kpc) below the plane (to the west), with the tips of the arc-like X-features extending even further. The northern-most of the eastern arc appears to extend out to $210''$ (17.4 kpc) above the plane.

Tracing the wind out to such large distances strengthens the case that the peculiar HI distribution of the dwarf galaxy NGC 3073 (10.0' away from NGC 3079, corresponding to a minimum physical separation of 49.7 kpc) is due to a wind from NGC 3079 (Irwin et al. 1987) ram-pressure stripping the ISM of this dwarf galaxy⁸. If this is occurring, there should be X-ray and H α emission associated with a bow shock upstream from NGC 3073 (similar to the Lehnert et al. (1999) model for the cloud found 11 kpc to the north of M82). We find no statistically-significant level of X-ray emission associated with NGC 3073 itself. The upper limit on the soft X-ray emission within a 2'-diameter aperture centered on NGC 3073 (this extends $\sim 1' \sim 5$ kpc further upstream than the HI) is $< 1.3 \times 10^{-3}$ counts s^{-1} (3σ , 0.3–2.0 keV energy band). Assuming a total absorbing column equal to the foreground Galactic column of $N_H = 2 \times 10^{20} \text{cm}^{-2}$, emission from a hot plasma with a temperature similar to what Lehnert et al. (1999) found for the M82 northern cloud ($kT \approx 0.8$ keV), and using the appropriate spectral responses, this corresponds to a flux limit of $f_X < 6 \times 10^{-15}$ erg $\text{s}^{-1} \text{cm}^{-2}$, and $L_X < 2 \times 10^{38}$ erg s^{-1} . By way of comparison, the M82 northern cloud has a soft X-ray luminosity of 2×10^{38} erg s^{-1} and a very similar H α luminosity. Were the M82 Northern cloud at a distance of 50 kpc from M82, we might expect its X-ray and H α luminosities to be a factor $(50/11)^2 \sim 20$ times fainter, given that it would intercept a significantly smaller fraction of the superwind's mechanical energy. Deep optical imaging may be a promising way of determining whether there really is a bow shock with luminosity $L_{\text{H}\alpha} \sim L_X \sim 10^{37}$ erg s^{-1} upwind of NGC 3073 (to our knowledge this has not been attempted, despite it being suggested by Irwin et al. 1987).

4.2.6. NGC 4945

NGC 4945 is one of the four brightest FIR sources in the sky outside the local group, along with the starburst galaxies NGC 253, M82 and M83 (Rice et al.

⁸Irwin et al. (1987) originally suggested ram pressure stripping of NGC 3073 when evidence for outflow was limited to the central kiloparsec of NGC 3079.

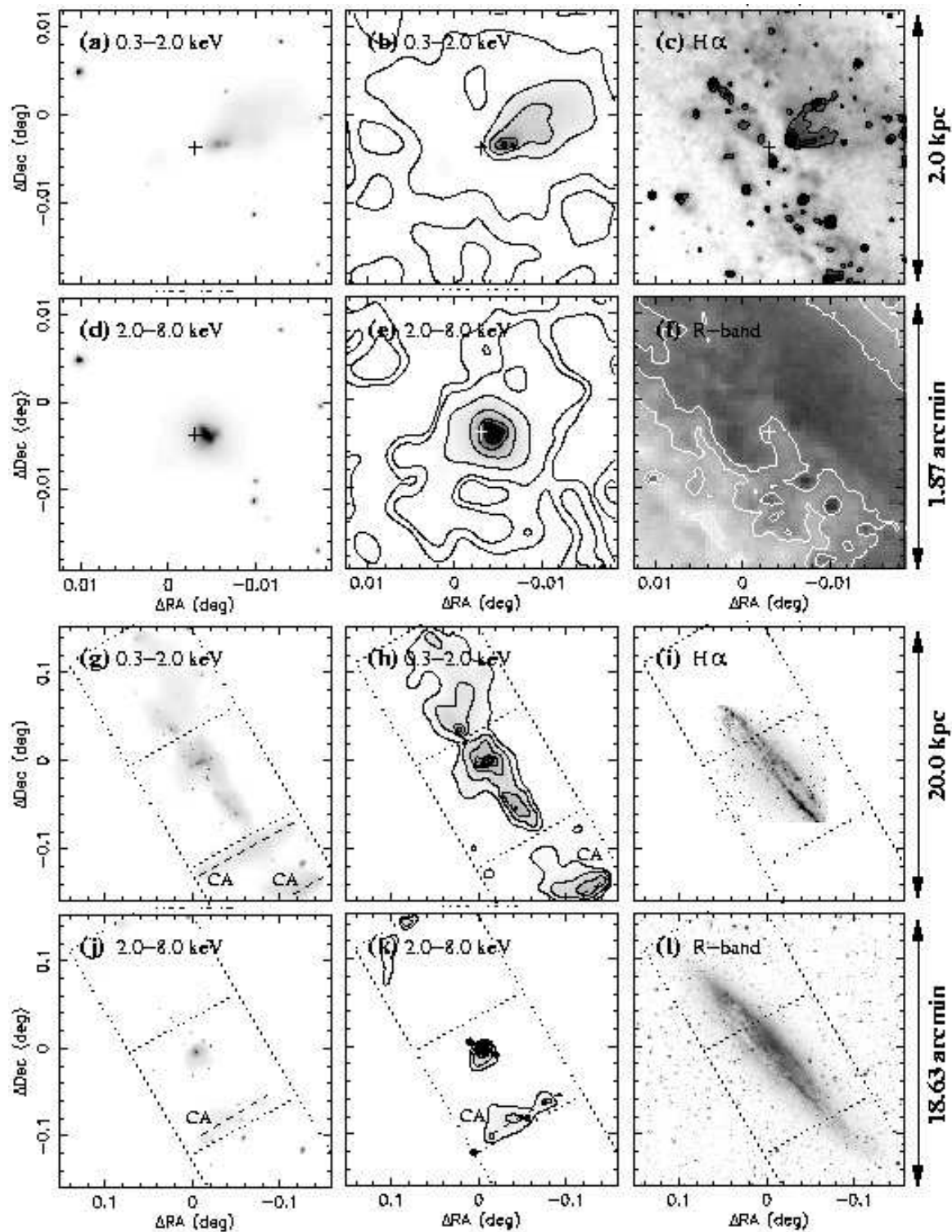


Fig. 9.— *Chandra* X-ray and optical images of NGC 4945. The meaning of each panel, and the intensity scales and contour levels used, are the same as those described in Fig. 2.

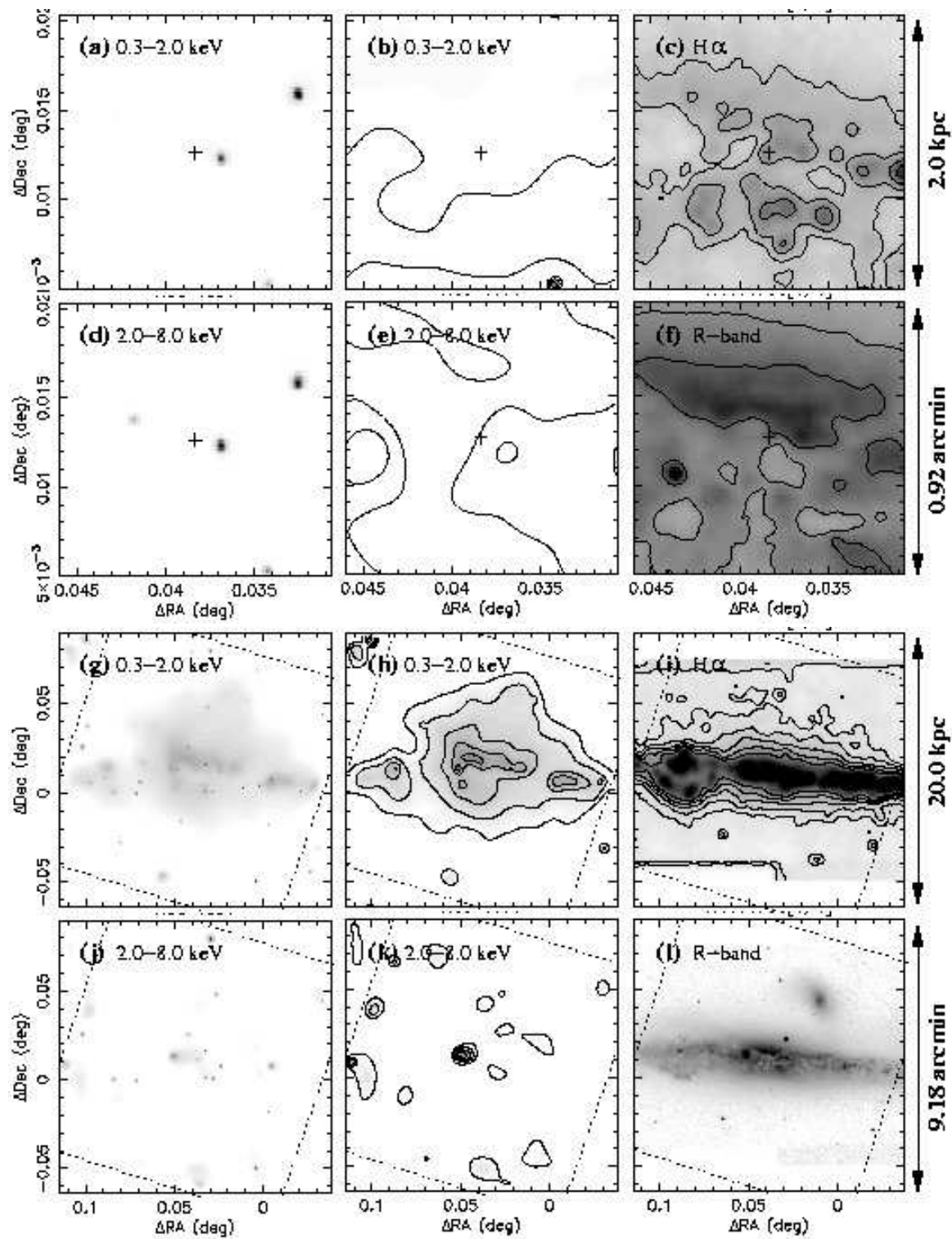


Fig. 10.— *Chandra* X-ray and optical images of NGC 4631. The meaning of each panel, and the intensity scales and contour levels used, are the same as those described in Fig. 2.

1988; Soifer et al. 1989), and hosts both vigorous nuclear star-formation (Moorwood & Oliva 1994; Spoon et al. 2000) and a peculiar AGN⁹ with an estimated bolometric luminosity of $\sim 60\%$ of the nuclear FIR luminosity (Madejski et al. 2000; Brock et al. 1988).

The star-formation is highly concentrated – HST NICMOS Pa α observations (Marconi et al. 2000) reveal a $11''$ -diameter (~ 200 pc) star-forming disk or ring, which corresponds closely in size to the FWHM = $12''$ FIR source that emits $\sim 50\%$ of the $100\mu\text{m}$ flux of the entire galaxy (Brock et al. 1988). Moorwood & Oliva (1994) find Br γ emission confined to the central $20''$. This implies that the current star-formation lies within the molecular gas torus found by Bergman et al. (1992, who argue that the CO emission comes from a ring of inner radius $\sim 7''$ and outer radius $\sim 16''$). Based on ISO-spectroscopy, Spoon et al. (2000) argue that a starburst of age $\geq 5 \times 10^6$ years is responsible for between 50 – 100% of the nuclear region’s bolometric luminosity.

Heckman et al. (1990) discovered a $\sim 500 \text{ km s}^{-1}$ conical outflow from the nucleus, extending at least ~ 600 pc to the NW along the minor axis. This is very similar to the starburst-driven outflow cone in NGC 253, and can *not* be a conventional AGN-lit ionization cone given the lack of [O III] emission (Moorwood et al. 1996). This H α outflow cone (Fig. 9c) is matched by a co-spatial limb-brightened X-ray outflow cone (Fig. 9b, see also Strickland 2002; Schurch et al. 2002). Note that the local signal-to-noise maximization used in the adaptive smoothing of the X-ray images tends to artificially reduce the apparent limb-brightening.

On larger scales, diffuse X-ray emission associated with the star-forming disk of NGC 4945 is apparent

⁹The obscured AGN, although often described as a Seyfert 2, is unusual in several ways. NGC 4945 is the second brightest source in the sky at $E = 100$ keV (Done, Madejski & Smith 1996), yet appears completely obscured along our line of sight at any energy less than ~ 10 keV (Marconi et al. 2000; Guianazzi et al. 2000, although cf. Krabbe et al. 2001). Unless the nuclear AGN is completely obscured over 4π steradian, it can not have a typical Seyfert SED and must be strongly deficient in UV photons given the low mid-IR-excitation and lack of [O III] in the outflow cone (Spoon et al. 2000; Marconi et al. 2000). Madejski et al. (2000) argue that total obscuration is impossible if the absorber is larger in size than a light day or so, based on the X-ray variability. In addition, the models of Levenson et al. (2002) would predict a iron K α equivalent width much higher than the value observed. If the SED of the AGN is unusual, this in turn raises the uncertainty associated with estimates of its bolometric luminosity based on extrapolations from the X-ray flux (e.g. Guianazzi et al. 2000; Madejski et al. 2000).

in Fig. 9h. Indeed, the spatial extent of diffuse X-ray emission is larger along the major axis of the galaxy than the minor axis. There is little or no evidence for significant extra-planar emission in other wave-bands. Optical filaments have only been traced out to ~ 2 kpc from the plane (Nakai 1989), and no radio emission has been discovered (Elmoultie et al. 1997).

NGC 4945 lies at low Galactic latitude, and consequently, the foreground HI column is high. The current lack of evidence for any larger, 10-kpc-scale, extra-planar emission, *i.e.* emission that might be expected from a starburst-driven superwind, is possibly due to the resulting high foreground optical depth of $\tau \sim 1$ for H α and soft X-ray radiation (see Table 3). The X-ray data from *Chandra* is further biased against a detection of diffuse emission due to the significantly higher than normal background experienced during this observation.

4.2.7. NGC 4631

NGC 4631 is often erroneously presented as an example of a “normal” spiral galaxy with a X-ray-emitting halo (e.g. see Wang et al. 2001). However, its large-scale-height non-thermal radio halo, warm IRAS 60 to $100\mu\text{m}$ flux ratio, high H α luminosity and optically disturbed morphology show it to be a highly atypical spiral galaxy. It is a good example of a galaxy experiencing a mild, disk-wide, starburst event (Golla & Wielebinski 1994).

In the optical and UV, NGC 4631 is a large, distorted, edge-on disk galaxy, with many H II regions, dust filaments and young stellar clusters spread throughout the disk (Rand, Kulkarni & Hester 1992; Smith et al. 2001). Four ~ 35 kpc-long HI spurs (Rand 1994) point to strong tidal interactions with a dwarf elliptical companion, NGC 4627 ($2\frac{1}{2}$ to the NW, ~ 5 kpc projected separation), and the edge-on spiral galaxy NGC 4656 ($32\frac{1}{4}$ to the SE, projected separation ~ 71 kpc). This interaction is thought to be the cause for the enhanced star-formation within the disk of NGC 4631. Molecular gas, and the recent star-formation, is less-centrally concentrated in NGC 4631 than in the other starburst galaxies of this sample (Golla & Wielebinski 1994; Golla et al. 1996; Golla 1999; Rand 2000), and Golla & Wielebinski describe the nuclear star-formation as an optically-obscured “mild central starburst.” NGC 4631 was one of the first spiral galaxies discovered to have a non-thermal radio halo (Ekers & Sancisi 1977), which has

been traced out to $\sim 4'$ ($z_{\max} \sim 9$ kpc) above and below the plane of the galaxy (Golla & Hummel 1994). The observed alignment of the halo magnetic field strongly suggests a large-scale outflow from the central 5 kpc of the disk (Golla & Hummel 1994), and although kinematic evidence for outflow exists (Golla et al. 1996; Rand 2000, cf. Martin & Kern 2001) it is less compelling than in the more powerful starbursts discussed earlier. A faint V-shaped pair of ~ 1.5 kpc-long $H\alpha$ filaments is seen directly above the optically-obscured nucleus, reminiscent of the outflow cones seen in NGC 253 and NGC 4945 (Rand et al. 1992, see also the HST WFPC2 images in Wang et al. 2001). The extra-planar $H\alpha$ emission is somewhat less vertically extended than the radio emission ($z_{\max} \sim 5$ kpc, Martin & Kern 2001), and is less-well organized into distinct multi-kpc filaments and arcs than it is in the other starburst galaxies (Rand et al. 1992; Hoopes et al. 1999). Vertically extended diffuse X-ray emission was first robustly detected by *ROSAT* PSPC observations (e.g. Wang et al. 1995; Vogler & Pietsch 1996; Read et al. 1997; Dahlem et al. 1998). Results from the *Chandra* ACIS-S observation of NGC 4631 were published by Wang et al. (2001).

The lack of central concentration in the star-formation is dramatically illustrated by the weakness of both soft and hard X-ray emission from the central 2 kpc (see Fig. 10a, b, d and e), both diffuse and point-like, in comparison to the starburst galaxies previously considered. There is diffuse emission in the central 2 kpc, but at low surface brightness (e.g. Wang et al. 2001).

There is no evidence of AGN-like activity in NGC 4631. The aligned triple radio source $\sim 6''$ to the SW of the dynamical center of the galaxy, identified by Golla (1999) as a low luminosity AGN candidate, has no X-ray counterpart in the *Chandra* observations.

The diffuse X-ray emission is brightest, and has its greatest vertical extent, above the central ~ 4 kpc of NGC 4631 (Fig. 10g and h). This region corresponds to the CO ring or bar (Rand 2000), is also the location of the brightest radio emission (Golla & Hummel 1994; Golla 1999), and is bounded on the east by the most prominent giant H II region visible within NGC 4631, CM67¹⁰ (Crillon & Monnet 1969). Diffuse X-

¹⁰Golla et al. (1996) present long-slit $H\alpha$ spectra with features consistent with outflow at velocities of several hundred km/s to the south of CM67. Rand (2000) presents evidence for outflow of molecular gas to the north of CM67.

ray emission definitely extends at least $180''$ (6.5 kpc) to the north and $130''$ (4.7 kpc) to the south of the disk, and appears to extend out to the edge of the S3 chip at $z \sim \pm 8$ kpc at lower surface brightness. Given the low diffuse X-ray flux, and its lack of concentration into specific filaments or arcs, the S/N of the diffuse X-ray images is low. This hinders a meaningful feature-by-feature comparison with the $H\alpha$ emission, beyond the general observation that the diffuse X-ray emission is brightest above the regions of the disk with the most prominent extra-planar $H\alpha$ emission.

Based on the older *ROSAT* PSPC observations of NGC 4631 it was already known that in terms of overall spatial extent the non-thermal radio emission (at either 1.4 GHz or 4.86 GHz, see Golla & Hummel 1994; Dahlem, Lisenfeld & Golla 1995) resembles the soft X-ray emission, the radio emission being somewhat more extended and/or brighter to the north of the disk, and most vertically extended above the same region of the disk (see the X-ray/radio overlays presented in Wang et al. 1995; Vogler & Pietsch 1996). It is difficult to make a more detailed morphological comparison than this using either the *ROSAT* data or the *Chandra* observations, in part due to the spatial filtering inherent in radio imaging. Vogler & Pietsch (1996) suggest, rather convincingly in our opinion, that “the north-eastern and south-eastern radio spurs seem to be avoided by the X-ray emission”, although both the radio and X-ray emission are faint in these regions. Nevertheless, when comparing the brightness of the soft X-ray emission to that of the nonthermal radio emission on a location by location basis it is as easy to find regions of apparent spatial correlation as to find regions with X-ray/radio anti-correlation (based on the images presented in Wang et al. 1995; Vogler & Pietsch 1996 or when overlaying the 1.4 GHz emission from the NVSS survey on the *Chandra* X-ray images), leading us to speculate that the halo magnetic fields and cosmic rays may be somewhat decoupled from the hot plasma. Perhaps the only robust conclusion that can be drawn is that there are magnetic fields and cosmic rays in the halo of NGC 4631, in addition to hot plasma.

4.2.8. NGC 6503

NGC 6503 is a low mass Sc galaxy, similar in size, mass, blue luminosity and infrared warmth to M33 (de Vaucouleurs & Caulet 1982; Rice et al. 1988). While otherwise an unremarkable galaxy, it has a compact, low velocity dispersion nucleus (Bottema & Gerritsen 1997), best classified as a borderline starburst-LINER

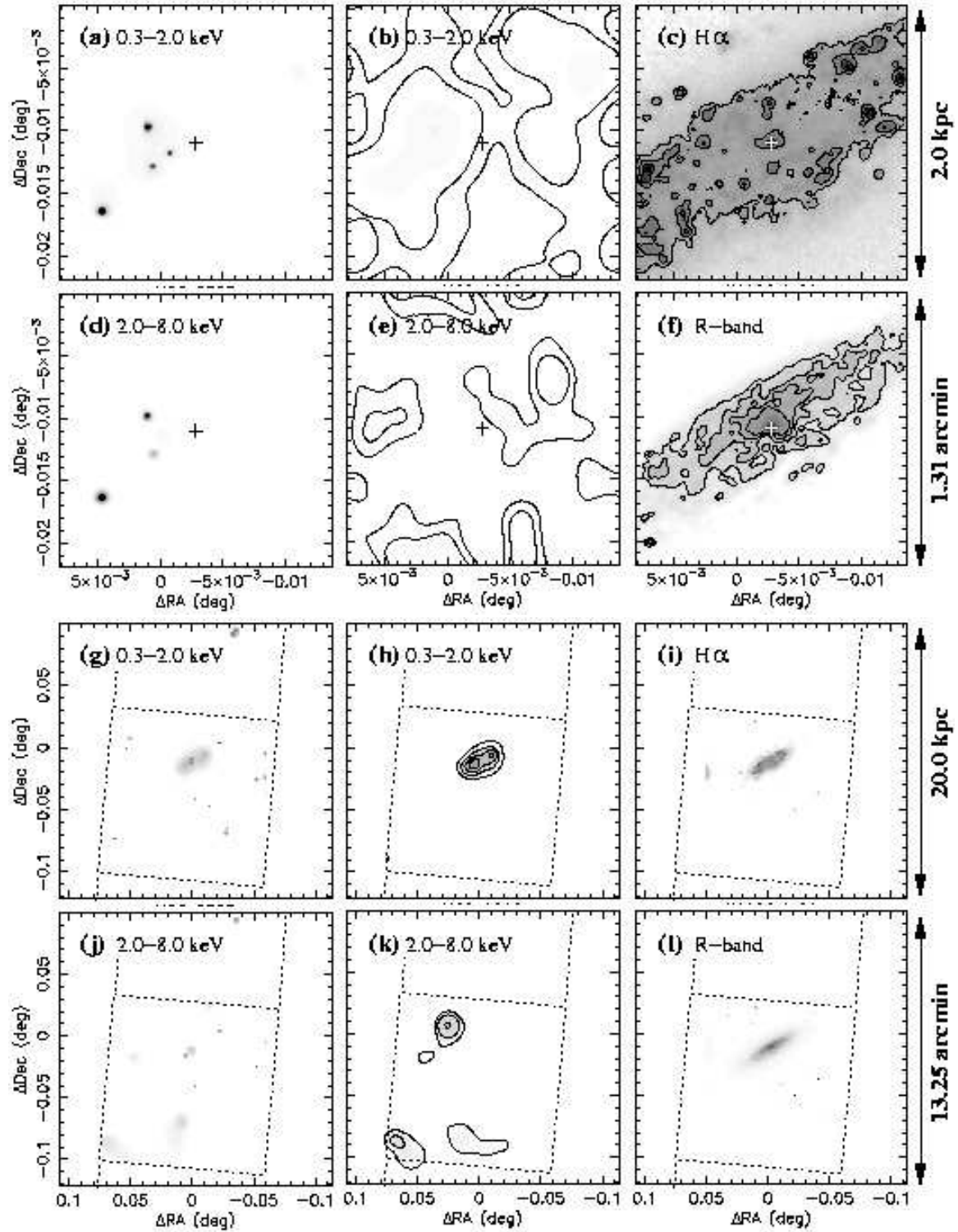


Fig. 11.— *Chandra* X-ray and optical images of NGC 6503. The meaning of each panel, and the intensity scales and contour levels used, are the same as those described in Fig. 2.

(Lira et al. 2002).

The moderate values of the IRAS f_{60}/f_{100} flux ratio and star-formation rate given in Table 1 imply that NGC 6503 as a whole should not be considered as a starburst galaxy.

Diffuse X-ray emission, first reported by Lira et al. (2002), is weak, and confined exclusively within the optical confines of the disk of NGC 6503 (see Fig. 11). We can only place upper limits on diffuse X-ray emission from the halo. The nucleus of the galaxy is marked by a very weak X-ray point source (see Lira et al. (2002) for more discussion of the point sources), and there is no obvious concentration of the diffuse X-ray emission toward the nucleus.

4.2.9. NGC 891

NGC 891 is a spiral galaxy very similar in size, total luminosity, spiral-type and molecular gas spatial distribution to the Milky Way, seen almost exactly edge-on (van der Kruit 1984; Scoville et al. 1993). Despite these similarities, *NGC 891 is forming stars more intensely than the Milky Way*, as it is twice as rich in molecular gas (Scoville et al. 1993), twice as IR-luminous as the Milky Way (Wainscoat, de Jong & Wesselius 1987), and several times more radio-luminous at 1.4 GHz (Allen, Baldwin & Sancisi 1978). The IRAS f_{60}/f_{100} ratio for NGC 891 is higher than that of the Milky Way (0.31 for NGC 891 vs. ~ 0.2 for the Milky Way, see Rice et al. 1988 and Boulanger & Péroult 1988).

There is no direct evidence for a weak AGN in NGC 891, although the *Chandra* observations do show a weak hard X-ray source (see Fig. 12a and d) $\sim 3''$ to SW of the position of the radio continuum point source we have adopted as the nucleus (Rupen 1991). Given the $\sim 2''$ positional uncertainty associated with the radio source, the X-ray source may be associated with it.

Little is known about the star formation rate in the nucleus of NGC 891 — optically the region is highly obscured by the prominent dust lane bisecting much of the disk. Diffuse X-ray emission within the central few kiloparsecs is faint, with a surface brightness 1 to 1.5 orders of magnitude fainter than in the starburst galaxies such as M82, NGC 1482 and NGC 3079. In the 0.3–1.0 keV energy band the presence of the dust lane is obvious (although not immediately apparent in Fig. 12b), and forms the basis of the X-ray shadowing experiment performed by Bregman & Irwin (2002).

NGC 891 has a radio (Allen et al. 1978), $H\alpha$ (Rand et al. 1990; Dettmar 1990; Hoopes et al. 1999), HI (Swaters, Sancisi & van der Hulst 1997) and X-ray halo, all of which extend to heights ~ 5 kpc above the plane of the galaxy. Dense dust clouds and filaments have been traced to heights of $|z| \sim 2$ kpc (Howk & Savage 1999, 2000). Diffuse X-ray emission in the halo of NGC 891 was discovered in *ROSAT* PSPC observations (Bregman & Pildis 1994; Bregman & Houck 1997), and it is currently the only normal spiral galaxy around which extra-planar diffuse X-ray emission has been detected.

Star-formation, as traced by $50\mu\text{m}$ IR emission (Wainscoat et al. 1987), non-thermal radio emission (Rupen et al. 1987), and $H\alpha$ emission (e.g. Hoopes et al. 1999), is not uniformly distributed throughout the disk of NGC 891. Star formation activity appears stronger along the major axis to the north-east of the nucleus than along the major axis to the south-west of nucleus. The distribution of extra-planar $H\alpha$ and soft X-ray emission is similarly asymmetric with respect to the nucleus, emission being strongest above the region of the disk to the north-east of nucleus (Fig. 12h and i). This strongly suggests that the extra-planar $H\alpha$ and soft X-ray is created by star-formation processes within the disk, as opposed to some form of accretion scenario (Toft et al. 2002; Sommer-Larsen et al. 2002). Diffuse *halo* X-ray emission extends along the plane of the galaxy $\sim 150''$ to the NE, and $\sim 90''$ to the SW, of the nucleus ($r \sim 7$ kpc and $r \sim 4.2$ kpc respectively), and appears to reach a height of $\sim 90''$ above and below the plane of galaxy over most of this region.

As in the case of NGC 4631, both the X-ray and $H\alpha$ emission appear relatively smooth and spatially uniform, although $H\alpha$ observations do show a variety of vertical filaments reaching heights of ~ 1.5 kpc above the plane (e.g. Howk & Savage 2000).

Note also that the diffuse X-ray emission is particularly intense, and has its greatest vertical extent, above (to the NW of) the nucleus (Fig. 12h), extending $\sim 140''$ ($z \sim 6.5$ kpc) from the nucleus. This suggests significant nuclear star formation is occurring in this region (perhaps associated with the $\sim 15''$ -radius [~ 700 pc] bar seen in CO emission, see García-Burillo & Guélin 1995).

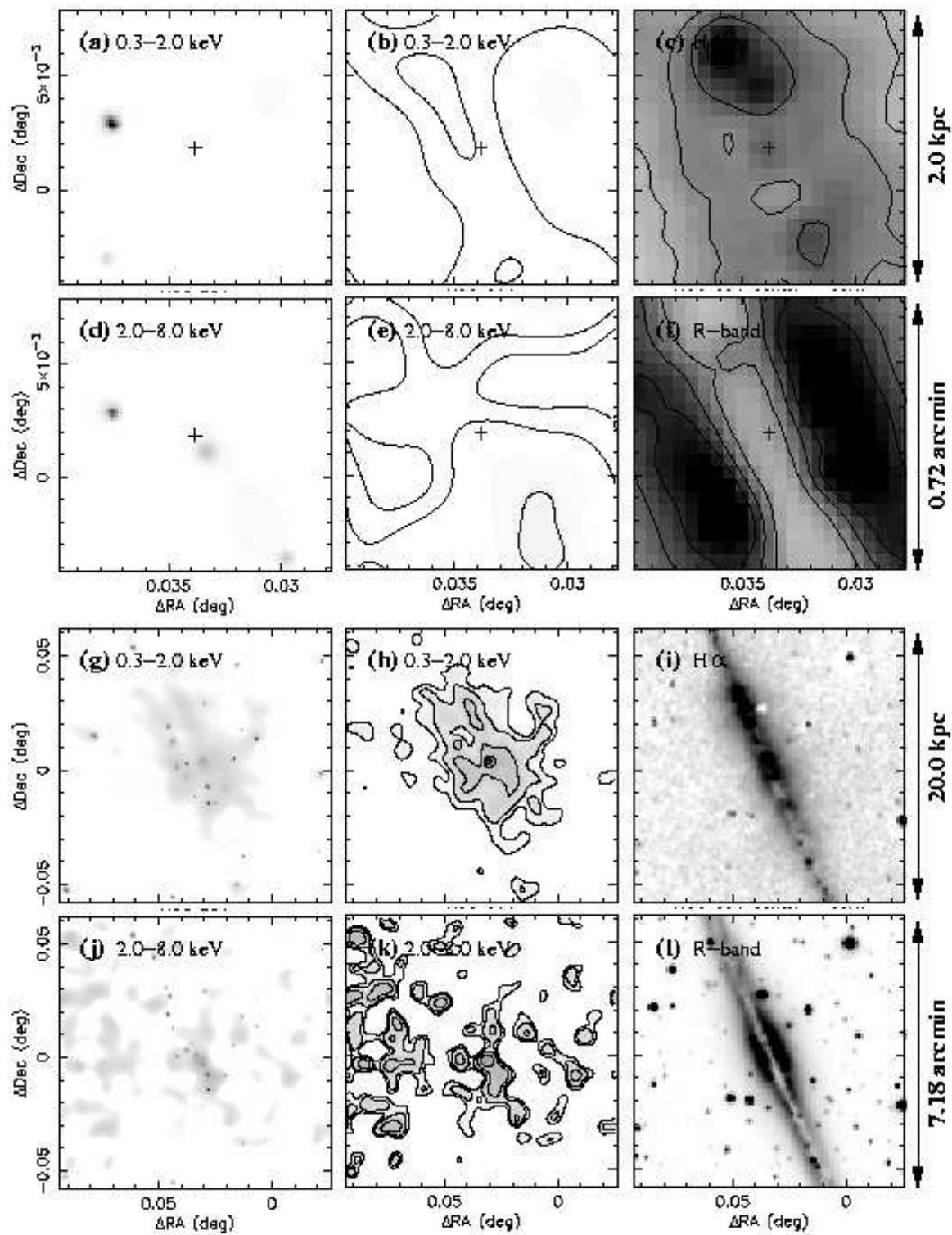


Fig. 12.— *Chandra* X-ray and optical images of NGC 891. The meaning of each panel, and the intensity scales and contour levels used, are the same as those described in Fig. 2.

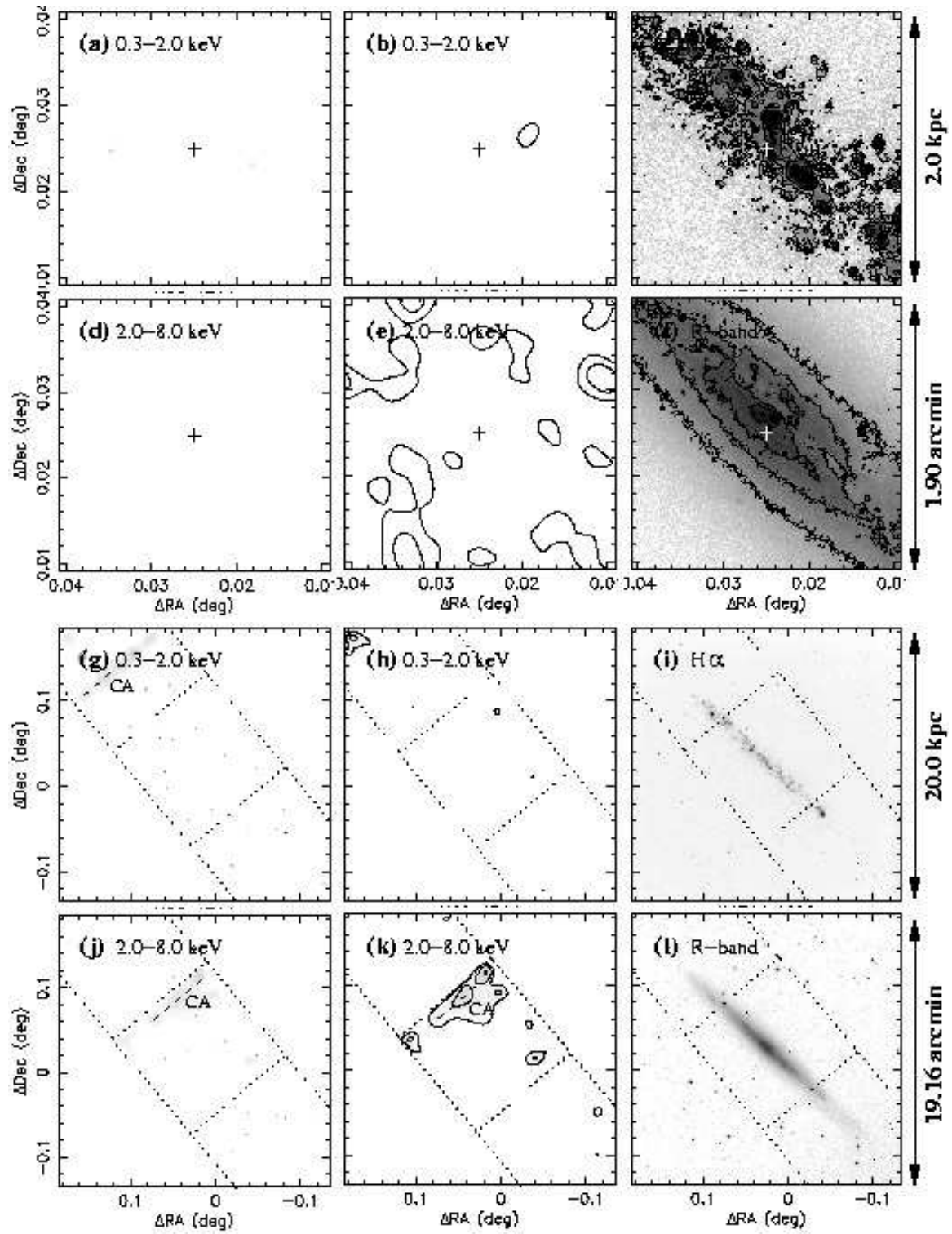


Fig. 13.— *Chandra* X-ray and optical images of NGC 4244. The meaning of each panel, and the intensity scales and contour levels used, are the same as those described in Fig. 2.

4.2.10. NGC 4244

NGC 4244 is a nearby, low-mass, Scd galaxy ($M_{\text{tot}} \approx 10^{10} M_{\odot}$; Fry et al. 1999) at a distance of 3.6 Mpc. The current star formation rate is low, based on the low IR (Rice et al. 1988) and $H\alpha$ luminosities (Hoopes et al. 1999). No evidence for a radio, UV or X-ray-emitting halo has been found (Bregman & Glassgold 1982; Schlickeiser, Werner & Wielebinski 1984; Deharveng et al. 1986, this paper). Deep $H\alpha$ imaging (Hoopes et al. 1999) demonstrates that warm ionized gas at $T \sim 10^4$ K is confined to within $40''$ (700 pc) of the disk of the galaxy. No nuclear activity is known in NGC 4244.

Despite the relatively long *Chandra* observation, there is a remarkable lack of X-ray emission from NGC 4244, with little or no concentration of X-ray point sources within the optical confines of the galaxy (see Fig. 13). There is only a weak, $\sim 3\sigma$, detection of residual emission within the disk after point source removal, and only an upper limit of $f_X < 1.6 \times 10^{-14}$ erg s $^{-1}$ cm $^{-2}$ (3σ upper limits in the 0.3–2.0 keV energy band, $L_X < 2.5 \times 10^{37}$ erg s $^{-1}$) could be obtained on diffuse emission from the halo.

4.3. Diffuse X-ray surface brightness and spectral hardness distributions

Quantitative measures of the spatial extent of the diffuse X-ray emission that can be used for comparative purposes are rare to non-existent within the extensive *ROSAT*-based literature. Typically individual papers, even those of samples of star-forming galaxies, only quote the size at which the diffuse emission disappears into the noise, *i.e.* observation-quality-dependent, rather than a size characteristic of the emitting galaxy.

To rectify this problem, we extracted one-dimensional X-ray surface brightness profiles, along both the major and minor axis, from the background-and-point-source-subtracted, exposure-map-corrected, diffuse X-ray images.

The major axis surface brightness profiles (Fig. 14) were extracted in slices 10 kpc high (*i.e.* extending from 5 kpc above and below the plane of the galaxy along the minor axis). The major-axis width of each bin was chosen to achieve ≥ 20 diffuse counts per slice. Errors were calculated taking into account both the Poisson uncertainties in the diffuse emission and the background. We also use the more conservative Gehrels (1986) approximation to Poisson statistics,

rather than using \sqrt{N} errors. Regions of sky exterior to any of the CCD chips were removed to avoid biasing the surface brightness calculations.

The minor axis profiles (Fig. 15) were created using the same method, with slices of total width 10 kpc parallel to the major axis (*i.e.* within 5 kpc of the minor axis of the galaxy).

Profiles were extracted in two energy bands - a soft 0.3–1.0 keV band and a medium 1.0–2.0 keV energy band. The medium band contains fewer counts than the soft energy band, but is significantly less affected by absorption. The effect of absorption of the X-ray emission by the gas within ~ 1 kpc of the planes of these galaxies is particularly noticeable in the minor axis surface brightness profiles of NGC 3628 and NGC 891, where the surface brightness in the 0.3–1.0 keV band drops to zero.

Two further sets of profiles, in 0.3–0.6 keV and 0.6–1.0 keV energy bands were also extracted for the purposes of mapping the variation in X-ray spectral hardness along the major and minor axes. If the surface brightness, or alternatively the count rates, in these four bands are $S_{0.3-1.0}$, $S_{1.0-2.0}$, $S_{0.3-0.6}$ and $S_{0.6-1.0}$ respectively, then we can define the following normalized hardness ratios:

$$Q_A = \frac{S_{0.6-1.0} - S_{0.3-0.6}}{S_{0.3-0.6} + S_{0.6-1.0}}, \text{ and}$$

$$Q_B = \frac{S_{1.0-2.0} - S_{0.3-1.0}}{S_{0.3-1.0} + S_{1.0-2.0}}. \quad (1)$$

For our present purposes, it should be noted that Q_A is sensitive to gas temperature, absorption and metal abundance (increased values of which lead to higher values of Q_A), while Q_B is most sensitive to the temperature of the X-ray emitting plasma, and then to absorption. See Fig. 7 in Strickland et al. (2002a). To enhance the signal-to-noise of the hardness profiles, we re-binned the surface brightness profiles to achieve ≥ 40 counts in the harder of each of the two bands used (this is often, but not always, the band with the fewest counts). Finally, points with hardness ratio uncertainties $\sigma_Q \geq 1$ are not plotted in Figs. 14 and 15, given that the poor constraint on their spectral hardness makes them meaningless.

We explored three independent methods to quantify the spatial extent of the diffuse emission along both the minor and major axes: sizes based on enclosing a fixed fraction of the total diffuse emission, sizes at fixed surface brightness levels (see Tables 4 and 5),

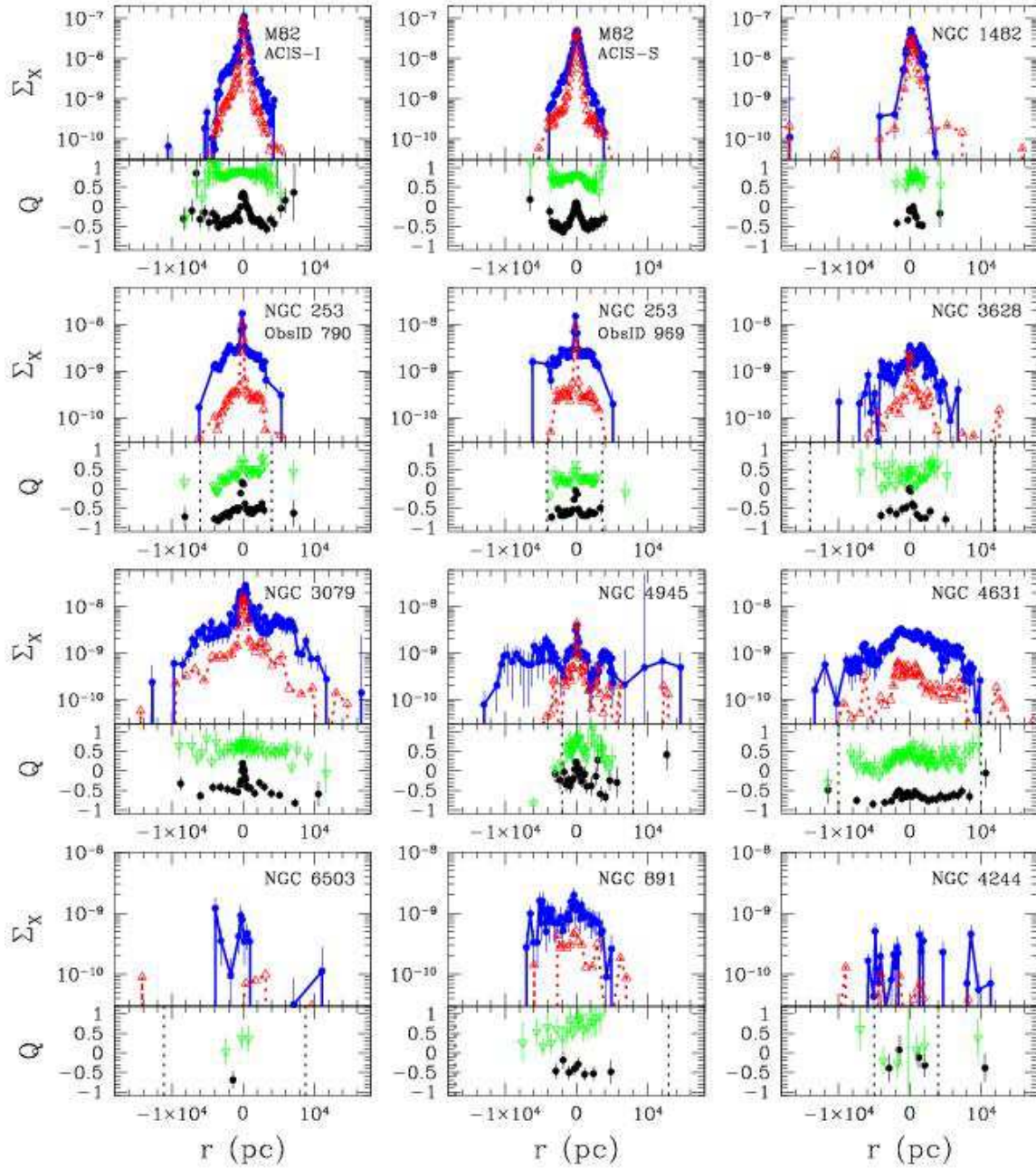


Fig. 14.— Major axis diffuse X-ray surface brightness and spectral hardness profiles. The soft band (0.3–1.0 keV) and medium band (1.0–2.0 keV) surface brightness Σ_X (photons $s^{-1} \text{ cm}^{-2} \text{ arcsec}^{-2}$) are shown as blue filled circles and red open triangles respectively. The spectral hardness ratios Q_A and Q_B (defined in § 4.3) for each galaxy are shown in the panel below the surface brightnesses, as green inverted open triangles and filled black circles respectively. Error bars show 68% confidence regions, based on the Gehrels (1986) approximation to Poisson statistics (error bars are not shown for surface brightness values in the 1.0–2.0 keV energy band). Vertical dashed lines show the approximate location of the edges of the back-illuminated S3 chip. Negative r is defined as the vector running from the nucleus along the major axis that has a position angle in the range $0 \leq \text{PA} \text{ (deg)} < 180$. Data was accumulated within $|z| \leq 5$ kpc of the midplane. Note that the axis scale on the ordinate is constant on a given row of figures, but varies between different rows.

and parameterized exponential, Gaussian and power-law model fits to the data (Table 6).

The galaxies within this sample are among those few edge-on galaxies that are X-ray bright enough, and close enough, to allow robust surface brightness profile fitting. In contrast, diffuse emission sizes based on a fixed flux fraction, or a fixed isophotal size, are more easily computed, even for distant and/or faint galaxies. We present the results from all three methods to allow both a cross-comparison between the various methods, and to allow for a later direct comparison of these galaxies against larger samples of more distant spiral and starburst galaxies.

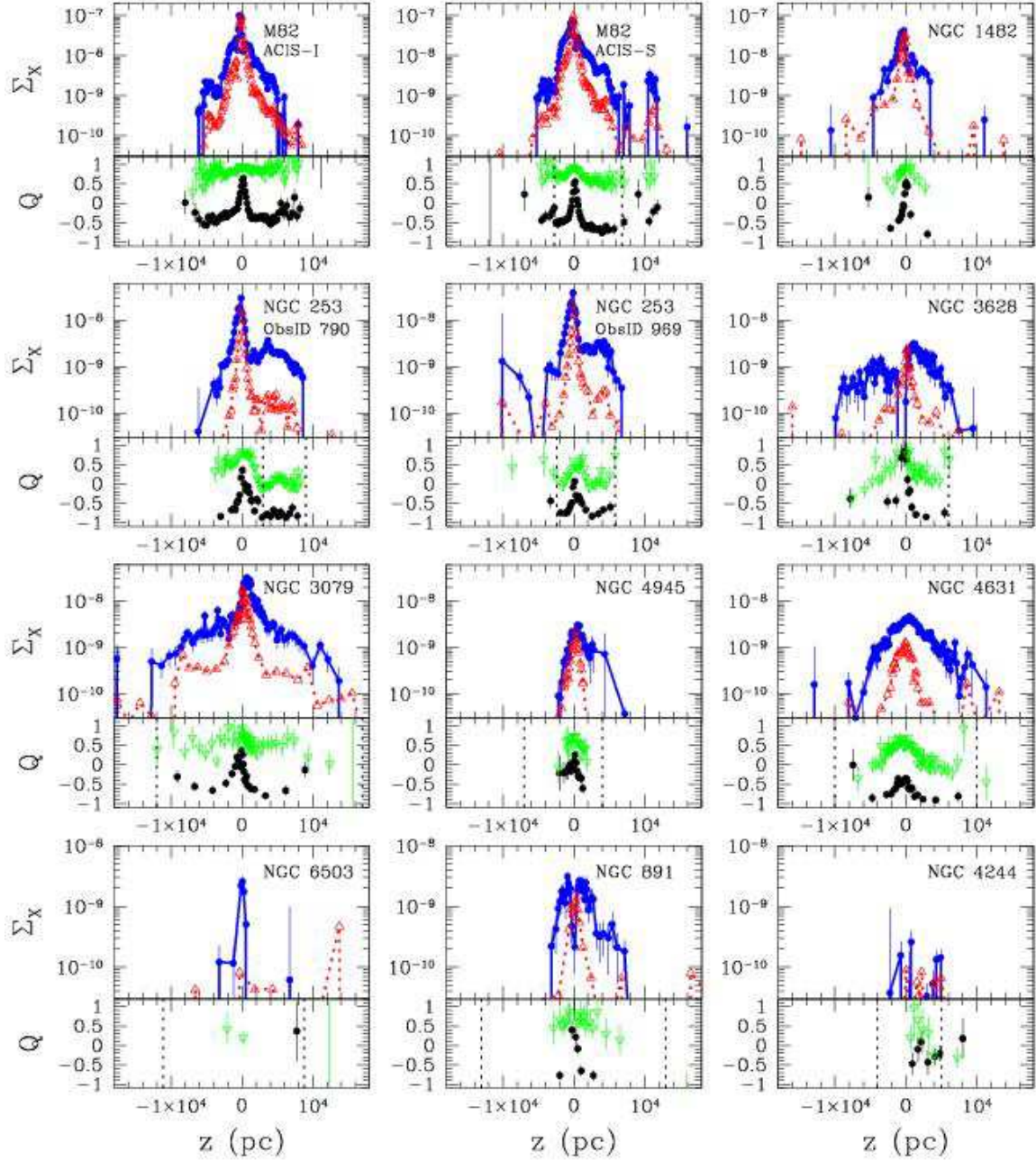


Fig. 15.— Minor axis diffuse X-ray surface brightness and spectral hardness profiles. The meaning of the symbols is the same as that used in Fig. 14. Positive z is defined as the vector running from the nucleus along the minor axis that has a position angle in the range $0 \leq \text{PA} \text{ (deg)} < 90$ or $270 \leq \text{PA} \text{ (deg)} < 360$. Data was accumulated within $|r| \leq 5$ kpc of the minor axis. Note that the axis scale on the ordinate is constant on a given row of figures, but varies between different rows.

TABLE 4
MINOR-AXIS DIFFUSE EMISSION SPATIAL EXTENT AT FIXED ENCLOSED FLUX FRACTIONS

Galaxy (1)	PA (2)	Energy (3)	$z_{0.5}$ (4)	$z_{0.75}$ (5)	$z_{0.9}$ (6)	$z_{0.95}$ (7)	$\Sigma_{0.5}$ (8)	$\Sigma_{0.75}$ (9)	$\Sigma_{0.9}$ (10)	$\Sigma_{0.95}$ (11)	z_{1e-9} (12)
M82 ^a	335	0.3-1.0	0.990	2.23	3.85	4.60	1.83e-08	1.31e-08	8.86e-09	7.78e-09	4.95
M82 ^a	155	0.3-1.0	0.555	1.36	2.19	3.53	7.20e-08	3.68e-08	2.55e-08	1.59e-08	5.48
M82 ^b	335	0.3-1.0	1.11	2.42	4.08	4.73	2.19e-08	1.60e-08	1.16e-08	1.06e-08	11.7
M82 ^b	155	0.3-1.0	0.522	1.12	1.66	1.97	6.58e-08	4.95e-08	4.11e-08	3.69e-08	4.81
NGC 1482	13	0.3-1.0	1.05	1.90	2.48	2.70	5.92e-09	5.13e-09	4.92e-09	4.81e-09	4.13
NGC 1482	193	0.3-1.0	0.587	0.984	1.64	2.05	3.28e-08	3.06e-08	2.22e-08	1.89e-08	4.22
NGC 253 ^c	319	0.3-1.0	0.601	2.54	3.64	4.08	1.15e-08	4.55e-09	3.95e-09	3.75e-09	5.50
NGC 253 ^c	139	0.3-1.0	0.302	0.658	1.08	1.39	3.02e-08	2.44e-08	1.89e-08	1.59e-08	2.03
NGC 253 ^d	319	0.3-1.0	2.63	4.16	5.45	5.92	3.22e-09	2.71e-09	2.37e-09	2.27e-09	6.42
NGC 253 ^d	139	0.3-1.0	0.265	0.632	1.21	1.78	2.47e-08	1.96e-08	1.37e-08	1.01e-08	2.60
NGC 3628	14	0.3-1.0	1.76	2.92	3.87	4.27	2.36e-09	2.06e-09	1.85e-09	1.75e-09	4.05
NGC 3628	194	0.3-1.0	3.48	4.58	5.40	6.03	4.66e-10	5.54e-10	5.89e-10	5.54e-10	4.73
NGC 3079	75	0.3-1.0	1.15	2.66	5.69	7.37	2.25e-08	1.55e-08	8.88e-09	7.23e-09	11.3
NGC 3079	255	0.3-1.0	3.26	5.89	8.22	9.48	3.74e-09	3.16e-09	2.71e-09	2.44e-09	8.64
NGC 4945	313	0.3-1.0	0.623	1.08	1.54	1.84	2.45e-09	2.31e-09	2.03e-09	1.84e-09	2.72
NGC 4945	133	0.3-1.0	0.313	0.800	1.20	1.36	1.91e-09	1.36e-09	1.12e-09	1.03e-09	0.553
NGC 4631	356	0.3-1.0	1.61	3.42	5.42	6.65	3.74e-09	2.81e-09	2.18e-09	1.87e-09	7.02
NGC 4631	176	0.3-1.0	1.37	2.39	3.66	4.42	3.14e-09	2.77e-09	2.22e-09	1.97e-09	3.81
NGC 6503	...	0.3-1.0	(1.0)	...	(4.0)	...	5.61e-9	...	5.63e-10
NGC 891	293	0.3-1.0	1.56	2.52	3.74	4.59	1.47e-09	1.46e-09	1.15e-09	9.94e-10	2.88
NGC 891	113	0.3-1.0	0.717	0.884	1.04	1.13	1.31e-09	1.65e-09	1.65e-09	1.61e-09	2.13
NGC 891	...	0.3-1.0	(1.0)	...	(4.0)	...	3.37e-9	...	2.34e-9
NGC 4244	...	0.3-1.0	(1.0)	...	(4.0)	...	6.97e-11	...	5.61e-11
M82 ^a	335	1.0-2.0	0.256	0.631	1.91	3.03	3.60e-08	2.34e-08	1.07e-08	6.90e-09	2.60
M82 ^a	155	1.0-2.0	0.160	0.555	1.40	1.86	8.68e-08	5.55e-08	2.08e-08	1.55e-08	2.13
M82 ^b	335	1.0-2.0	0.274	0.645	1.84	3.35	4.94e-08	3.50e-08	1.56e-08	9.16e-09	2.73
M82 ^b	155	1.0-2.0	0.209	0.582	1.30	1.71	7.99e-08	5.21e-08	2.95e-08	2.39e-08	2.27
NGC 1482	13	1.0-2.0	0.182	0.649	1.26	1.59	1.43e-08	6.26e-09	4.09e-09	2.81e-09	1.48
NGC 1482	193	1.0-2.0	0.339	0.714	1.75	3.52	2.94e-08	2.26e-08	9.83e-09	5.31e-09	1.77
NGC 253 ^c	319	1.0-2.0	0.155	0.602	2.50	3.78	1.15e-08	5.90e-09	1.76e-09	1.32e-09	0.814
NGC 253 ^c	139	1.0-2.0	0.0642	0.291	0.673	1.02	2.25e-08	1.41e-08	8.44e-09	6.13e-09	0.953
NGC 253 ^d	319	1.0-2.0	0.119	0.575	3.56	4.84	1.11e-08	5.31e-09	1.14e-09	8.92e-10	0.676
NGC 253 ^d	139	1.0-2.0	0.0483	0.211	0.496	0.744	1.81e-08	1.41e-08	8.28e-09	6.27e-09	0.774
NGC 3628	14	1.0-2.0	0.355	1.02	2.55	3.55	1.77e-09	9.72e-10	4.38e-10	3.43e-10	0.322
NGC 3628	194	1.0-2.0	0.435	0.963	1.75	2.10	8.01e-10	5.68e-10	3.64e-10	3.28e-10	0.149
NGC 3079	75	1.0-2.0	0.628	1.37	5.63	8.75	1.11e-08	7.64e-09	2.13e-09	1.51e-09	2.03
NGC 3079	255	1.0-2.0	1.02	3.86	7.89	9.38	4.33e-09	1.60e-09	1.03e-09	8.96e-10	1.93
NGC 4945	313	1.0-2.0	0.220	0.392	0.520	0.576	1.81e-09	1.70e-09	1.58e-09	1.52e-09	0.590
NGC 4945	133	1.0-2.0	0.346	0.857	1.50	2.17	8.93e-10	5.95e-10	4.01e-10	2.80e-10	0.225
NGC 4631	356	1.0-2.0	0.657	1.48	3.70	7.49	8.47e-10	5.82e-10	2.65e-10	1.40e-10	0.221
NGC 4631	176	1.0-2.0	0.839	1.56	2.94	5.14	9.02e-10	7.53e-10	4.49e-10	2.58e-10	0.242
NGC 6503	...	1.0-2.0	(1.0)	...	(4.0)	...	6.84e-10	...	1.07e-10
NGC 891	293	1.0-2.0	0.740	4.90	15.5	16.9	9.00e-10	1.76e-10	8.75e-11	8.56e-11	0.589
NGC 891	113	1.0-2.0	0.209	0.319	0.385	0.407	9.42e-10	9.27e-10	9.18e-10	9.15e-10	0.226
NGC 891	...	1.0-2.0	(1.0)	...	(4.0)	...	2.72e-9	...	6.39e-10
NGC 4244	...	1.0-2.0	(1.0)	...	(4.0)	...	1.18e-10	...	2.80e-11

NOTE.—Fixed enclosed flux and isophotal *heights* of the diffuse X-ray emission. Column 2: Position angle along which the surface brightness profile was extracted. Column 3: Energy band in keV. Column 4: Distance along minor axis (in kpc) at which 50% of the total diffuse X-ray counts, *as measured from the major axis along this specific position angle*, are contained. In other words, $z_{0.5}$ is the minor axis X-ray half-light height. Each side of the disk is treated independently. Columns 5, 6 and 7: As column (4), but the 75, 90 and 95% X-ray-light-enclosed heights. Columns 8, 9, 10 and 11: The effective diffuse X-ray surface brightness, in units of photons $s^{-1} cm^{-2} arcsec^{-2}$, between the major axis and $z_{0.5}$, $z_{0.75}$, $z_{0.90}$ and $z_{0.95}$ respectively. This value is based on the exposure and chip-sensitivity corrected images. Note that this is not the same as the surface brightness at that height. Column 12: Minor axis isophotal height (in kpc), at which the X-ray surface brightness drops to 10^{-9} photons $s^{-1} cm^{-2} arcsec^{-2}$. Note that when a position angle is not given, this denotes a measurement based on the count rate within a circular aperture from the diffuse-emission-only images, and not from the 1-D surface brightness profiles. The radius chosen is shown in brackets in columns 4 and 6. See § 4.3 for details.

^aACIS-I observations of M82, ObsIDs 361 and 1302.

^bACIS-S observation of M82, ObsID 2933.

^cNGC 253 observation ObsID 969, nucleus and disk on chip S3, northern halo on S4.

^dNGC 253 observation ObsID 790, northern halo on chip S3, disk and nucleus on S2.

4.3.1. Sizes at fixed enclosed-light fractions

In Tables 4 and 5 we present the spatial extent of the diffuse emission measured along the minor and major axes from the nucleus, within which a fixed fraction (50, 75, 90 and 95%) of the total number diffuse X-ray counts were found within the 1-dimensional slices. The mean X-ray surface brightness Σ within these regions is also tabulated. As an example, the value of $\Sigma_{0.5}$ in the first row of Table 4 is the surface brightness in the 0.3 – 1.0 keV energy band within a region 10 kpc in major axis extent, and extending 0.99 kpc (the minor axis half-light height $z_{0.5}$) along the minor axis of M82 to the NNE (along position angle 335). The total number of counts is evaluated the extreme edge of each slice, *i.e.* we assume all emission is contained within 20 kpc of the nucleus. There exists the possibility that X-ray emission may extended significantly further than this at lower surface brightness than these observations are sensitive to, although this would have relatively little impact on the 50 and 75%-enclosed light radii and heights we report.

The diffuse X-ray emission in NGC 6503 and NGC 4244 is so faint that direct measurements of the half light and isophotal sizes can not be robustly measured from the 1-D minor axis, or major axis, surface brightness profiles. In this case, we simply report a measurement of the surface brightness within a circular apertures of radius 1 and 4 kpc, values typical of the 50 and 90% enclosed light heights and radii of the other galaxies in the sample. It is possible that at these very low surface brightness levels we are looking at unresolved faint X-ray point source emission, and not truly diffuse hot gas.

4.3.2. Sizes at fixed surface brightness levels

Isophotal sizes, measured from the 1-dimensional surface brightness profiles at the point Σ_X reaches 10^{-9} photons s^{-1} cm^{-2} $arcsec^{-2}$, are given in Tables 4 and 5.

Given the spectrum the X-ray emitting halo gas (see § 5.3), a surface brightness of 10^{-9} photons s^{-1} cm^{-2} $arcsec^{-2}$ in the 0.3–1.0 keV band corresponds to an intrinsic emitted energy flux (*i.e.* correcting for Galactic and intrinsic absorption) of approximately $\sim 2 \times 10^{-18}$ erg s^{-1} cm^{-2} $arcsec^{-2}$ in either the 0.3–1.0 or 0.3–2.0 keV energy band. In the 1.0–2.0 keV energy band, 10^{-9} photons s^{-1} cm^{-2} $arcsec^{-2}$ corresponds to $\approx 1.5 \times 10^{-17}$ erg s^{-1} cm^{-2} $arcsec^{-2}$ in the 0.3–2.0 keV energy band, and $\approx 2 \times 10^{-18}$ erg s^{-1} cm^{-2} $arcsec^{-2}$ in

the 1.0–2.0 keV energy band. These conversion factors are the typical, approximately average, value for all of the galaxies with halo X-ray emission, and are in fact based on the NGC 3079 halo spectra. Note that these conversions take the contamination of the ACIS optical blocking filter into account.

The range of X-ray spectral hardness, foreground absorption, and level of blocking filter contamination in this sample introduces a range of a factor two into this conversion. More specifically, the the intrinsic energy flux per photon is a factor ~ 2 higher for the ACIS-S observation of M82 and a factor ~ 2 lower for the NGC 253 observations.

Diffuse X-ray emission can be robustly detected at lower X-ray surface brightness levels than 10^{-9} photons s^{-1} cm^{-2} $arcsec^{-2}$, in both the 0.3–1.0 and 1.0–2.0 keV energy bands, but we chose this isophote as it is well-matched to deep studies of optical extraplanar emission (for $H\alpha$ emission from gas at $T = 10^4$ K, a surface brightness of 2×10^{-18} erg s^{-1} cm^{-2} $arcsec^{-2}$ corresponds to an emission measure [EM] of 1 pc cm^{-6}).

4.3.3. Model fits

We used the CIAO fitting routine SHERPA to fit exponential, Gaussian and power law models to the 0.3–1.0 keV energy band 1-D X-ray minor axis surface brightness profiles, after splitting the minor axis data into two separate profiles for positive and negative z .

We used the 0.3–1.0 keV energy band as it contains the greatest number of diffuse X-ray counts, and traces the diffuse X-ray emission to greater distances from the plane of the galaxy, than the 1.0–2.0 keV energy band. The obvious disadvantage with using this energy band is that absorption by gas and dust in the plane of the host galaxy can be significant (as can be seen in the higher values of hardness ratio Q_A near the plane in Fig. 15).

However, as the primary aim of this paper is to quantify the properties of the *extra*-planar diffuse X-ray emission, it is advantageous to exclude the data within 1 or 2 kpc of the plane from the fit in any case. Results of the model fitting, along with the range of z values used, is given in Table 6 (to conserve space we have not tabulated the best-fit model normalizations for the Gaussian and power law models). We find that exponential, and/or Gaussian, models provide the best description of the observed minor axis surface profiles.

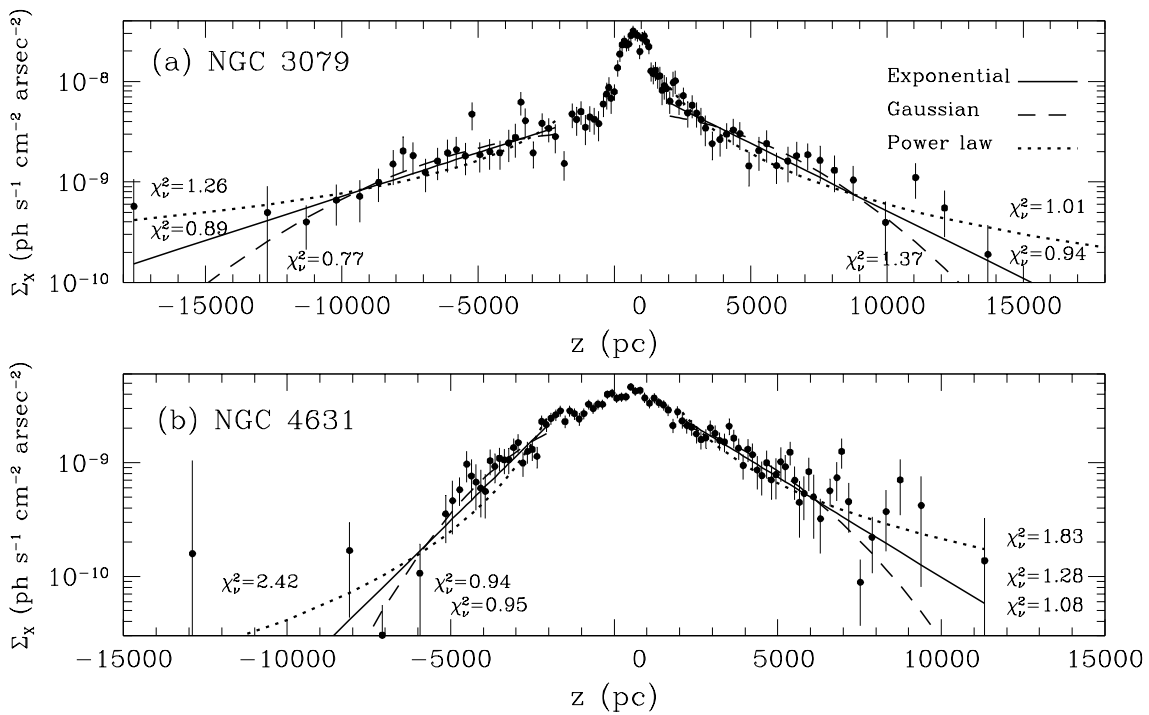


Fig. 16.— Two examples of the observed 0.3–1.0 keV minor axis diffuse X-ray surface brightness profiles, with the best-fit exponential (solid line), Gaussian (dashed) and power law (dotted) models. The reduced χ^2 values of the fits are given alongside the appropriate curve. Points within 2 kpc of the plane of the galaxy were not used in the fitting process due to the high, and spatially non-uniform, absorption near the disk midplane.

TABLE 5
MAJOR-AXIS DIFFUSE EMISSION SPATIAL EXTENT AT FIXED ENCLOSED FLUX FRACTIONS

Galaxy (1)	PA (2)	Energy (3)	$r_{0.5}$ (4)	$r_{0.75}$ (5)	$r_{0.9}$ (6)	$r_{0.95}$ (7)	$\Sigma_{0.5}$ (8)	$\Sigma_{0.75}$ (9)	$\Sigma_{0.9}$ (10)	$\Sigma_{0.95}$ (11)	r_{1e-9} (12)
M82 ^a	245	0.3-1.0	0.313	0.683	1.20	1.87	9.59e-08	6.70e-08	4.63e-08	3.13e-08	3.57
M82 ^a	65	0.3-1.0	0.416	1.35	2.43	2.94	4.59e-08	2.31e-08	1.45e-08	1.25e-08	3.65
M82 ^b	245	0.3-1.0	0.274	0.622	1.11	1.74	4.48e-08	3.31e-08	2.35e-08	1.63e-08	2.63
M82 ^b	65	0.3-1.0	0.321	0.876	1.85	2.48	3.54e-08	2.22e-08	1.32e-08	1.05e-08	3.17
NGC 1482	283	0.3-1.0	0.505	0.934	1.34	1.55	4.05e-08	3.40e-08	2.89e-08	2.60e-08	3.22
NGC 1482	103	0.3-1.0	0.139	0.278	0.394	0.429	2.65e-08	2.34e-08	2.10e-08	2.07e-08	1.97
n253 ^c	229	0.3-1.0	0.843	1.61	2.25	2.56	3.29e-09	2.85e-09	2.73e-09	2.64e-09	3.59
n253 ^c	49	0.3-1.0	0.452	1.59	2.30	2.79	8.77e-09	4.40e-09	3.89e-09	3.58e-09	7.59
n253 ^d	229	0.3-1.0	0.750	1.50	2.15	2.46	4.22e-09	3.33e-09	2.98e-09	2.88e-09	3.20
n253 ^d	49	0.3-1.0	0.847	2.04	2.97	3.48	6.95e-09	4.66e-09	3.84e-09	3.51e-09	4.51
NGC 3628	284	0.3-1.0	1.58	2.43	3.17	3.49	2.33e-09	2.27e-09	2.07e-09	1.96e-09	3.49
NGC 3628	104	0.3-1.0	1.70	3.31	4.05	4.71	1.42e-09	1.14e-09	1.12e-09	8.52e-10	4.10
NGC 3079	345	0.3-1.0	1.99	4.87	6.62	7.40	1.12e-08	7.13e-09	6.32e-09	5.98e-09	9.39
NGC 3079	165	0.3-1.0	1.43	3.82	5.63	6.23	1.05e-08	6.02e-09	4.98e-09	4.75e-09	7.52
NGC 4945	223	0.3-1.0	1.52	3.65	4.42	4.90	1.34e-09	8.14e-10	8.30e-10	7.99e-10	4.16
NGC 4945	43	0.3-1.0	1.67	4.64	7.80	9.59	1.06e-09	7.56e-10	6.08e-10	5.46e-10	6.09
NGC 4631	266	0.3-1.0	2.59	4.73	6.37	6.94	2.22e-09	1.87e-09	1.69e-09	1.65e-09	7.17
NGC 4631	86	0.3-1.0	1.94	3.82	6.17	6.74	2.75e-09	2.20e-09	1.70e-09	1.66e-09	6.73
NGC 891	203	0.3-1.0	0.929	1.60	2.04	2.18	1.10e-09	1.02e-09	9.67e-10	9.56e-10	1.05
NGC 891	23	0.3-1.0	3.04	4.81	6.33	9.67	9.15e-10	9.17e-10	8.26e-10	5.51e-10	5.31
M82 ^a	245	1.0-2.0	0.184	0.401	0.736	1.00	8.41e-08	6.37e-08	4.13e-08	3.21e-08	1.48
M82 ^a	65	1.0-2.0	0.0995	0.329	1.32	2.10	6.58e-08	4.04e-08	1.37e-08	8.52e-09	2.03
M82 ^b	245	1.0-2.0	0.156	0.379	0.730	1.08	4.19e-08	3.10e-08	2.06e-08	1.52e-08	1.32
M82 ^b	65	1.0-2.0	0.153	0.416	0.971	1.82	3.72e-08	2.55e-08	1.42e-08	8.20e-09	1.48
NGC 1482	283	1.0-2.0	0.395	0.747	1.22	1.57	2.66e-08	2.23e-08	1.62e-08	1.30e-08	2.64
NGC 1482	103	1.0-2.0	0.131	0.348	0.637	0.746	1.42e-08	9.20e-09	6.29e-09	5.33e-09	1.40
n253 ^c	229	1.0-2.0	0.149	1.21	2.05	2.47	2.90e-09	7.72e-10	6.05e-10	5.61e-10	0.266
n253 ^c	49	1.0-2.0	0.0682	0.303	1.63	2.21	9.50e-09	5.95e-09	1.65e-09	1.35e-09	0.450
n253 ^d	229	1.0-2.0	0.0795	0.880	1.87	2.28	4.67e-09	1.28e-09	7.79e-10	7.13e-10	0.282
n253 ^d	49	1.0-2.0	0.0606	0.278	1.60	2.28	1.05e-08	6.89e-09	1.78e-09	1.33e-09	0.445
NGC 3628	284	1.0-2.0	0.969	2.66	7.41	9.58	7.01e-10	4.14e-10	1.68e-10	1.41e-10	0.224
NGC 3628	104	1.0-2.0	0.930	2.67	4.73	5.72	5.42e-10	2.97e-10	2.09e-10	1.68e-10	0.181
NGC 3079	345	1.0-2.0	0.568	2.59	4.95	6.54	1.03e-08	3.69e-09	2.27e-09	1.72e-09	3.69
NGC 3079	165	1.0-2.0	0.509	2.81	4.89	6.33	8.12e-09	2.46e-09	1.69e-09	1.39e-09	1.49
NGC 4945	223	1.0-2.0	0.513	2.58	4.35	5.70	1.89e-09	5.90e-10	4.11e-10	3.21e-10	0.368
NGC 4945	43	1.0-2.0	0.414	1.28	2.57	3.02	1.51e-09	7.56e-10	3.47e-10	3.29e-10	0.209
NGC 4631	266	1.0-2.0	3.21	6.60	11.0	12.8	2.77e-10	2.07e-10	1.42e-10	1.40e-10	...
NGC 4631	86	1.0-2.0	1.53	2.45	5.12	6.55	4.34e-10	3.85e-10	2.03e-10	1.89e-10	...
NGC 891	203	1.0-2.0	0.458	1.12	1.72	1.94	3.98e-10	3.10e-10	2.50e-10	2.39e-10	...
NGC 891	23	1.0-2.0	1.06	1.88	2.31	2.43	3.54e-10	3.24e-10	3.16e-10	3.21e-10	...

NOTE.—Fixed enclosed flux and isophotal *radii* measured along the *major* axis of each galaxy. Apart from being the radius from the nucleus, instead of height above the plane, the meaning of the table columns are identical to those in Table 4.

^aACIS-I observations of M82, ObsIDs 361 and 1302.

^bACIS-S observation of M82, ObsID 2933.

^cNGC 253 observation ObsID 969, nucleus and disk on chip S3, northern halo on S4.

^dNGC 253 observation ObsID 790, northern halo on chip S3, disk and nucleus on S2.

TABLE 6

EXPONENTIAL, GAUSSIAN AND POWER LAW MODEL FITS TO MINOR AXIS DIFFUSE EMISSION

Galaxy	PA	Energy	z_{range}	Exponential model			Gaussian model			Power law		
(1)	($^{\circ}$)	(keV)	(kpc)	H_{eff}	Σ_0	χ^2	ν	χ^2/ν	$FWHM$	χ^2/ν	α	χ^2/ν
(1)	(2)	(3)	(4)	(5)	(6)	(7)	(8)	(9)	(10)	(11)	(12)	(13)
M82 ^a	335	0.3-1.0	0.5-5	1.42 ^{+0.06} _{-0.05}	29.16 ^{+1.53} _{-1.48} × 10 ⁻⁹	354.2	30	<u>11.8</u>	4.13 ^{+0.13} _{-0.13}	25.8	1.20 ^{+0.03} _{-0.03}	14.1
M82 ^a	335	0.3-1.0	1-5	1.53 ^{+0.09} _{-0.08}	25.51 ^{+2.25} _{-2.08} × 10 ⁻⁹	329.3	27	12.20	4.83 ^{+0.18} _{-0.17}	18.8	1.53 ^{+0.07} _{-0.07}	<u>8.5</u>
M82 ^a	155	0.3-1.0	0.2-10	0.73 ^{+0.02} _{-0.02}	103.4 ^{+3.52} _{-3.42} × 10 ⁻⁹	1318.5	41	<u>32.16</u>	2.42 ^{+0.05} _{-0.05}	71.1	1.44 ^{+0.01} _{-0.01}	86.6
M82 ^a	155	0.3-1.0	2-6	1.10 ^{+0.17} _{-0.15}	32.21 ^{+1.62} _{-1.50} × 10 ⁻⁹	308.8	25	12.35	4.87 ^{+0.48} _{-0.48}	13.9	3.11 ^{+0.18} _{-0.17}	<u>11.2</u>
M82 ^b	335	0.3-1.0	0.35-16	1.54 ^{+0.05} _{-0.05}	36.22 ^{+1.45} _{-1.45} × 10 ⁻⁹	498.2	56	<u>8.9</u>	4.78 ^{+0.15} _{-0.15}	14.0	1.39 ^{+0.02} _{-0.02}	30.6
M82 ^b	335	0.3-1.0	1-5	0.64 ^{+0.02} _{-0.02}	175.50 ^{+16.14} _{-14.77} × 10 ⁻⁹	453.5	27	16.8	4.66 ^{+0.16} _{-0.15}	20.4	0.94 ^{+0.03} _{-0.03}	<u>5.8</u>
M82 ^b	155	0.3-1.0	0.2-10	0.78 ^{+0.02} _{-0.02}	104.0 ^{+2.7} _{-2.8} × 10 ⁻⁹	674.3	36	18.7	2.35 ^{+0.04} _{-0.04}	<u>18.3</u>	1.27 ^{+0.01} _{-0.01}	121.2
M82 ^b	155	0.3-1.0	2-6	1.04 ^{+0.30} _{-0.27}	27.98 ^{+56.98} _{-78.4} × 10 ⁻⁹	145.4	21	6.92	4.92 ^{+0.69} _{-0.77}	7.4	3.71 ^{+0.47} _{-0.42}	<u>6.3</u>
NGC 1482	13	0.3-1.0	1-17	1.19 ^{+0.38} _{-0.33}	17.59 ^{+12.11} _{-6.98} × 10 ⁻⁹	21.8	13	1.67	4.62 ^{+0.70} _{-0.70}	<u>1.52</u>	2.21 ^{+0.42} _{-0.42}	2.59
NGC 1482	13	0.3-1.0	2-17	0.77 ^{+0.34} _{-0.27}	108.5 ^{+53.0} _{-53.0} × 10 ⁻⁹	10.1	9	1.12	3.76 ^{+0.87} _{-0.87}	<u>0.85</u>	4.32 ^{+1.57} _{-1.57}	1.50
NGC 1482	103	0.3-1.0	0.2-19	0.81 ^{+0.11} _{-0.10}	64.61 ^{+11.40} _{-10.11} × 10 ⁻⁹	28.3	24	<u>1.18</u>	2.07 ^{+0.26} _{-0.23}	1.94	1.39 ^{+0.06} _{-0.06}	5.46
NGC 1482	103	0.3-1.0	2-19	1.14 ^{+0.75} _{-0.49}	29.23 ^{+123.6} _{-20.35} × 10 ⁻⁹	14.9	10	1.49	4.81 ^{+1.80} _{-1.41}	<u>1.42</u>	3.17 ^{+1.40} _{-0.72}	1.71
NGC 253 ^c	319	0.3-1.0	4-8	1.39 ^{+0.77} _{-0.45}	45.11 ^{+166.4} _{-32.5} × 10 ⁻⁹	43.8	8	1.68	6.31 ^{+1.66} _{-1.21}	<u>1.67</u>	2.93 ^{+0.27} _{-0.22}	2.93
NGC 253 ^d	319	0.3-1.0	4-10	2.91 ^{+0.60} _{-0.45}	7.46 ^{+2.96} _{-2.39} × 10 ⁻⁹	34.8	20	1.74	9.65 ^{+0.99} _{-0.81}	<u>1.37</u>	1.92 ^{+0.07} _{-0.07}	2.20
NGC 253 ^c	139	0.3-1.0	0.3-4	0.58 ^{+0.03} _{-0.03}	44.20 ^{+3.39} _{-3.19} × 10 ⁻⁹	35.3	11	3.21	1.69 ^{+0.08} _{-0.07}	<u>3.14</u>	1.38 ^{+0.03} _{-0.03}	29.9
NGC 253 ^d	139	0.3-1.0	0.3-4	0.58 ^{+0.02} _{-0.02}	34.37 ^{+1.91} _{-1.82} × 10 ⁻⁹	73.6	14	<u>5.26</u>	1.68 ^{+0.06} _{-0.07}	9.76	1.86 ^{+0.02} _{-0.02}	77.4
NGC 3628	14	0.3-1.0	1-17	2.00 ^{+0.31} _{-0.27}	5.42 ^{+1.21} _{-1.00} × 10 ⁻⁹	41.9	42	1.00	6.33 ^{+0.67} _{-0.65}	<u>0.95</u>	1.57 ^{+0.17} _{-0.16}	2.01
NGC 3628	14	0.3-1.0	2-17	1.94 ^{+0.41} _{-0.34}	5.81 ^{+1.00} _{-1.73} × 10 ⁻⁹	40.4	32	1.26	6.75 ^{+0.28} _{-0.78}	<u>1.04</u>	2.08 ^{+0.22} _{-0.22}	1.92
NGC 3628	194	0.3-1.0	2-19	3.72 ^{+1.09} _{-0.86}	1.42 ^{+0.56} _{-0.44} × 10 ⁻⁹	83.2	32	2.60	11.39 ^{+1.86} _{-1.69}	<u>2.05</u>	1.45 ^{+0.35} _{-0.24}	3.46
NGC 3628	194	0.3-1.0	1-19	4.21 ^{+0.93} _{-0.85}	1.07 ^{+0.27} _{-0.27} × 10 ⁻⁹	90.7	37	2.45	11.72 ^{+1.70} _{-1.70}	<u>1.87</u>	1.05 ^{+0.20} _{-0.20}	3.45
NGC 3079	75	0.3-1.0	1-18	1.82 ^{+0.41} _{-0.33}	29.00 ^{+9.67} _{-7.12} × 10 ⁻⁹	88.6	42	2.11	5.04 ^{+0.97} _{-0.76}	3.39	1.67 ^{+0.15} _{-0.14}	<u>0.96</u>
NGC 3079	75	0.3-1.0	2-18	3.23 ^{+0.98} _{-0.70}	11.44 ^{+3.94} _{-3.19} × 10 ⁻⁹	28.3	30	<u>0.94</u>	10.67 ^{+2.14} _{-2.00}	1.37	1.67 ^{+0.19} _{-0.15}	1.01
NGC 3079	255	0.3-1.0	0-18	5.20 ^{+1.29} _{-0.98}	4.85 ^{+0.85} _{-0.85} × 10 ⁻⁹	46.7	38	<u>1.23</u>	12.89 ^{+1.94} _{-1.68}	1.33	0.55 ^{+0.07} _{-0.08}	1.78
NGC 3079	255	0.3-1.0	2-18	4.96 ^{+1.66} _{-1.12}	5.38 ^{+1.91} _{-1.51} × 10 ⁻⁹	23.1	26	0.89	13.33 ^{+2.44} _{-1.93}	<u>0.77</u>	1.08 ^{+0.17} _{-0.14}	1.26
NGC 4945	313	0.3-1.0	0.5-5	1.06 ^{+0.30} _{-0.18}	5.01 ^{+1.17} _{-0.96} × 10 ⁻⁹	12.9	15	<u>0.86</u>	2.50 ^{+0.41} _{-0.32}	1.24	0.88 ^{+0.08} _{-0.07}	1.06
NGC 4945	133	0.3-1.0	0.5-5	0.59 ^{+0.15} _{-0.13}	3.11 ^{+0.82} _{-0.66} × 10 ⁻⁹	11.7	12	<u>0.98</u>	1.61 ^{+0.39} _{-0.35}	1.83	1.22 ^{+0.07} _{-0.08}	2.74
NGC 4631	356	0.3-1.0	0.5-17	2.42 ^{+0.19} _{-0.18}	5.70 ^{+0.46} _{-0.44} × 10 ⁻⁹	57.5	51	<u>1.12</u>	6.66 ^{+0.46} _{-0.45}	1.91	0.92 ^{+0.05} _{-0.05}	4.03
NGC 4631	356	0.3-1.0	2-17	2.37 ^{+0.29} _{-0.27}	5.99 ^{+1.33} _{-1.05} × 10 ⁻⁹	49.9	39	1.28	7.85 ^{+0.68} _{-0.63}	<u>1.08</u>	1.63 ^{+0.14} _{-0.12}	1.83
NGC 4631	176	0.3-1.0	0-17	2.33 ^{+0.23} _{-0.21}	4.33 ^{+0.34} _{-0.33} × 10 ⁻⁹	46.1	38	<u>1.21</u>	5.27 ^{+0.41} _{-0.38}	1.28	0.44 ^{+0.03} _{-0.03}	8.02
NGC 4631	176	0.3-1.0	2-17	1.89 ^{+0.50} _{-0.38}	5.76 ^{+2.76} _{-1.73} × 10 ⁻⁹	21.8	23	0.95	5.97 ^{+0.59} _{-0.61}	<u>0.94</u>	1.82 ^{+0.27} _{-0.23}	1.27
NGC 6503	32	0.3-1.0	0-10	0.33 ^{+0.17} _{-0.17}	3.57 ^{+2.68} _{-1.72} × 10 ⁻⁹	7.3	13	<u>0.56</u>	0.72 ^{+0.64} _{-0.29}	0.59	1.04 ^{+0.18} _{-0.18}	0.81
NGC 6503	212	0.3-1.0	0-5	0.18 ^{+0.36} _{-0.18}	3.72 ^{+0.11} _{-2.56} × 10 ⁻⁹	1.1	5	<u>0.22</u>	0.50 ^{+0.43} _{-0.45}	<u>0.22</u>	2.24 ^{+0.14} _{-0.25}	0.56
NGC 891	293	0.3-1.0	2-8	2.44 ^{+3.94} _{-1.34}	2.21 ^{+6.77} _{-1.43} × 10 ⁻⁹	9.7	10	0.97	8.12 ^{+4.49} _{-4.16}	1.18	1.57 ^{+0.76} _{-0.46}	<u>0.83</u>
NGC 891	293	0.3-1.0	0.4-8	1.97 ^{+0.65} _{-0.47}	3.33 ^{+1.01} _{-0.85} × 10 ⁻⁹	19.2	21	<u>0.91</u>	4.46 ^{+1.03} _{-0.74}	0.99	0.88 ^{+0.15} _{-0.17}	1.63
NGC 891	113	0.3-1.0	0.4-5	1.35 ^{+0.50} _{-0.35}	3.64 ^{+1.33} _{-1.05} × 10 ⁻⁹	15.4	14	1.10	3.57 ^{+0.82} _{-0.66}	<u>0.67</u>	1.03 ^{+0.17} _{-0.21}	2.31

NOTE.—See § 4.3.3 for more information. All errors are 1σ for 2 interesting parameters. For each row the lowest reduced χ^2 value has been underlined, to aid the reader in assessing which form of surface model provides the best description of the data. The columns are (2): Position angle of the minor axis surface brightness slice used. (3): Energy band from which the data was extracted. (4): Range of heights above or below the plane of the galaxy used in fitting the surface brightness profiles. (5): Best-fit effective exponential scale height, in kpc. (6): Extrapolated central surface brightness (*i.e.* at $z = 0$), in units of photons $\text{s}^{-1} \text{cm}^{-2} \text{arcsec}^{-2}$. (7, 8 and 9): Total χ^2 value for best-fit exponential model, number of degrees of freedom ν (this is the same for the Gaussian and power law models) and reduced χ^2 value. (10): Best fit Gaussian model FWHM in kpc. (11): Best fit reduced χ^2 for the Gaussian surface brightness model. (12): Best fit power law slope. (13): Best fit reduced χ^2 for the power law surface brightness model.

^aACIS-I observations of M82, ObsIDs 361 and 1302.

^bACIS-S observation of M82, ObsID 2933.

^cNGC 253 observation ObsID 969, nucleus and disk on chip S3, northern halo on S4.

^dNGC 253 observation ObsID 790, northern halo on chip S3, disk and nucleus on S2.

Spectral variation and other caveats

Note that these 1-dimensional fits are intended as a simple empirical measure of the general way in which the surface brightness drops off with increasing height. It is clear that there is real 2-or-3-dimensional structure in the X-ray-emitting gas, with edge-brightened limbs, filaments and clumps apparent in several of Figs. 2 – 13, in addition to the 1st-order decrease in brightness with z .

In several galaxies, notably M82, NGC 253 (northern halo), and NGC 3079, the hardness ratios Q_A and Q_B show no significant spatial variation within increasing distance from the mid-plane, beyond a height of $|z| \sim 2$ kpc (Fig. 15). This implies that no significant variations in plasma temperature or intervening absorption exist, and hence that changes in Σ_X are directly proportional to changes in $\int n_e^2 \delta l$. The typical best-fit surface-brightness exponential scale heights are $H_{\text{eff}} \sim$ a few kpc, implying density scale heights twice as large.

Some galaxies do show intriguing hints of spectral variation within their halos, e.g. NGC 4631, or to the southern side of NGC 3628 (negative z -axis in Fig. 15). A gentle decrease in hardness ratio Q_A is apparent in both of these cases, consistent with either a decrease in effective plasma temperature and/or intrinsic or intervening absorption. Peculiarly, the northern side of NGC 3628 shows no similar spectral softening.

TABLE 7
NUCLEAR, DISK AND HALO COUNT RATES

Galaxy	Region	Size maj. \times min.	Diffuse only?	Area	Soft 0.3-1.0 keV cts/s	tot cts	Medium 1.0-2.0 keV cts/s	tot cts	Hard 2.0-8.0 keV cts/s	tot cts
(1)	(2)	(3)	(4)	(5)	(6)	(7)	(8)	(9)	(10)	(11)
M82 ^a	nucl	1.90	diff	0.663	0.2424 \pm 0.0023	11757	0.5666 \pm 0.0034	27482	0.1445 \pm 0.0018	7007
M82 ^a	nucl	1.90	wsrc	0.711	0.2480 \pm 0.0023	12028	0.6649 \pm 0.0037	32250	0.3719 \pm 0.0028	18038
M82 ^a	disk	8.91 \times 3.81	diff	30.448	0.5196 \pm 0.0034	25206	0.3739 \pm 0.0029	18137	0.0508 \pm 0.0018	2463
M82 ^a	disk	8.91 \times 3.81	wsrc	31.181	0.4915 \pm 0.0033	23845	0.3846 \pm 0.0029	18658	0.0680 \pm 0.0019	3300
M82 ^a	halo	8.00 \times 15.50	diff	90.024	0.1780 \pm 0.0028	8635	0.0640 \pm 0.0020	3105	0.0021 \pm 0.0031	101
M82 ^a	halo	8.00 \times 15.50	wsrc	91.499	0.1878 \pm 0.0028	9111	0.0816 \pm 0.0021	3960	0.0140 \pm 0.0032	677
M82 ^b	nucl	1.90	diff	0.642	0.3955 \pm 0.0048	7116	0.6057 \pm 0.0059	10898	0.1848 \pm 0.0033	3325
M82 ^b	nucl	1.90	wsrc	0.712	0.4879 \pm 0.0053	8779	0.8471 \pm 0.0069	15242	0.5104 \pm 0.0054	9184
M82 ^b	disk	8.91 \times 3.81	diff	31.183	1.1697 \pm 0.0084	21048	0.5490 \pm 0.0058	9879	0.0744 \pm 0.0035	1339
M82 ^b	disk	8.19 \times 3.81	wsrc	31.435	1.1961 \pm 0.0085	21524	0.5889 \pm 0.0060	10597	0.1018 \pm 0.0037	1832
M82 ^b	halo	8.00 \times 15.50	diff	35.144	0.2589 \pm 0.0044	4658	0.0482 \pm 0.0023	866	-0.0002 \pm 0.0030	-4
M82 ^b	halo	8.00 \times 15.50	wsrc	35.426	0.2668 \pm 0.0045	4800	0.0581 \pm 0.0025	1045	0.0063 \pm 0.0031	114
NGC 1482	nucl	0.312	diff	0.016	0.0073 \pm 0.0006	170	0.0077 \pm 0.0006	180	0.0027 \pm 0.0004	64
NGC 1482	nucl	0.312	wsrc	0.020	0.0092 \pm 0.0007	215	0.0120 \pm 0.0008	280	0.0128 \pm 0.0008	300
NGC 1482	disk	2.19 \times 0.62	diff	1.343	0.0359 \pm 0.0014	843	0.0171 \pm 0.0010	400	0.0039 \pm 0.0008	91
NGC 1482	disk	2.19 \times 0.62	wsrc	1.343	0.0359 \pm 0.0014	843	0.0171 \pm 0.0010	400	0.0039 \pm 0.0008	91
NGC 1482	halo	1.00 \times 1.80	diff	1.178	0.0099 \pm 0.0008	231	0.0020 \pm 0.0005	46	-0.0000 \pm 0.0006	-1
NGC 1482	halo	1.00 \times 1.80	wsrc	1.178	0.0099 \pm 0.0008	231	0.0020 \pm 0.0005	46	-0.0000 \pm 0.0006	-1
NGC 253 ^c	nucl	2.65	diff	1.310	0.1816 \pm 0.0042	1995	0.1532 \pm 0.0039	1683	0.0406 \pm 0.0022	446
NGC 253 ^c	nucl	2.65	wsrc	1.374	0.2294 \pm 0.0047	2520	0.2585 \pm 0.0050	2839	0.1197 \pm 0.0035	1315
NGC 253 ^c	disk	20.42 \times 5.29	diff	40.380	0.4296 \pm 0.0069	4719	0.0865 \pm 0.0037	951	0.0228 \pm 0.0046	251
NGC 253 ^c	disk	20.42 \times 5.29	wsrc	40.993	0.5298 \pm 0.0075	5820	0.2422 \pm 0.0053	2661	0.1237 \pm 0.0055	1359
NGC 253 ^c	halo	12.00 \times 24.00	diff	27.770	0.0895 \pm 0.0037	983	0.0077 \pm 0.0021	84	0.0029 \pm 0.0037	32
NGC 253 ^c	halo	12.00 \times 24.00	wsrc	28.137	0.0950 \pm 0.0038	1043	0.0111 \pm 0.0022	122	0.0062 \pm 0.0037	68
NGC 253 ^d	halo	12.00 \times 24.00	diff	69.1181	0.1755 \pm 0.0030	6720	0.0194 \pm 0.0019	744	0.0043 \pm 0.0032	163
NGC 253 ^d	halo	12.00 \times 24.00	wsrc	69.9867	0.1962 \pm 0.0031	7513	0.0328 \pm 0.0020	1258	0.0146 \pm 0.0032	559
NGC 3628	nucl	0.69	diff	0.086	0.0018 \pm 0.0002	98	0.0024 \pm 0.0002	134	0.0012 \pm 0.0002	66
NGC 3628	nucl	0.69	wsrc	0.094	0.0020 \pm 0.0002	107	0.0043 \pm 0.0003	233	0.0037 \pm 0.0003	201
NGC 3628	disk	10.47 \times 1.37	diff	11.267	0.0195 \pm 0.0010	1068	0.0075 \pm 0.0007	410	0.0056 \pm 0.0010	305
NGC 3628	disk	10.47 \times 1.37	wsrc	11.485	0.0258 \pm 0.0010	1409	0.0372 \pm 0.0010	2034	0.0368 \pm 0.0013	2013
NGC 3628	halo	4.00 \times 7.00	diff	17.842	0.0291 \pm 0.0012	1592	0.0036 \pm 0.0007	196	-0.0002 \pm 0.0012	-12
NGC 3628	halo	4.00 \times 7.00	wsrc	17.901	0.0381 \pm 0.0013	2085	0.0105 \pm 0.0008	576	0.0044 \pm 0.0013	241
NGC 3079	nucl	0.40	diff	0.032	0.0050 \pm 0.0005	131	0.0101 \pm 0.0007	268	0.0071 \pm 0.0006	187
NGC 3079	nucl	0.40	wsrc	0.032	0.0050 \pm 0.0005	131	0.0101 \pm 0.0007	268	0.0071 \pm 0.0006	187
NGC 3079	disk	5.50 \times 0.80	diff	4.266	0.0579 \pm 0.0017	1549	0.0209 \pm 0.0010	553	0.0032 \pm 0.0010	86
NGC 3079	disk	5.50 \times 0.80	wsrc	4.390	0.0682 \pm 0.0018	1809	0.0322 \pm 0.0012	854	0.0105 \pm 0.0011	279
NGC 3079	halo	4.80 \times 6.60	diff	23.274	0.0491 \pm 0.0021	1301	0.0099 \pm 0.0013	259	0.0026 \pm 0.0020	69
NGC 3079	halo	4.80 \times 6.60	wsrc	23.401	0.0530 \pm 0.0021	1406	0.0174 \pm 0.0014	461	0.0096 \pm 0.0021	256
NGC 4945	nucl	1.86	diff	0.667	0.0124 \pm 0.0008	356	0.0230 \pm 0.0010	659	0.0432 \pm 0.0013	1238
NGC 4945	nucl	1.86	wsrc	0.681	0.0133 \pm 0.0008	380	0.0240 \pm 0.0010	688	0.0438 \pm 0.0014	1254
NGC 4945	disk	13.80 \times 3.72	diff	31.143	0.0967 \pm 0.0038	2771	0.0519 \pm 0.0032	1489	0.0662 \pm 0.0055	1897
NGC 4945	disk	13.80 \times 3.72	wsrc	31.514	0.1347 \pm 0.0040	3861	0.1750 \pm 0.0038	5016	0.1712 \pm 0.0058	4908
NGC 4945	halo	8.20 \times 8.20	diff	26.119	0.0057 \pm 0.0029	165	0.0045 \pm 0.0025	130	0.0003 \pm 0.0046	8
NGC 4945	halo	8.20 \times 8.20	wsrc	26.249	0.0069 \pm 0.0030	198	0.0058 \pm 0.0025	167	0.0016 \pm 0.0046	46
NGC 4631	nucl	0.92	diff	0.122	0.0009 \pm 0.0002	49	0.0006 \pm 0.0001	31	0.0003 \pm 0.0001	15
NGC 4631	nucl	0.92	wsrc	0.165	0.0014 \pm 0.0002	78	0.0026 \pm 0.0003	145	0.0021 \pm 0.0003	117
NGC 4631	disk	10.47 \times 1.83	diff	15.107	0.0808 \pm 0.0016	4496	0.0175 \pm 0.0009	977	0.0033 \pm 0.0013	181
NGC 4631	disk	10.47 \times 1.83	wsrc	15.889	0.1120 \pm 0.0017	6235	0.0600 \pm 0.0013	3340	0.0431 \pm 0.0016	2401
NGC 4631	halo	8.20 \times 8.20	diff	45.585	0.0571 \pm 0.0019	3181	0.0030 \pm 0.0012	164	0.0018 \pm 0.0021	98
NGC 4631	halo	8.20 \times 8.20	wsrc	46.231	0.0673 \pm 0.0020	3746	0.0135 \pm 0.0013	754	0.0118 \pm 0.0022	659
NGC 6503	nucl	1.32	diff	0.323	0.0027 \pm 0.0007	29	0.0008 \pm 0.0005	8	0.0010 \pm 0.0007	10
NGC 6503	nucl	1.32	wsrc	0.343	0.0086 \pm 0.0011	92	0.0082 \pm 0.0010	88	0.0057 \pm 0.0010	61
NGC 6503	disk	5.58 \times 2.65	diff	14.280	0.0177 \pm 0.0030	188	0.0020 \pm 0.0023	22	0.0076 \pm 0.0042	81
NGC 6503	disk	5.58 \times 2.65	wsrc	14.323	0.0249 \pm 0.0031	264	0.0173 \pm 0.0026	184	0.0174 \pm 0.0044	185
NGC 6503	halo	5.00 \times 7.00	diff	17.141	-0.0002 \pm 0.0031	-2	0.0039 \pm 0.0026	42	0.0006 \pm 0.0047	6
NGC 6503	halo	5.00 \times 7.00	diff	17.141	< 0.0068	< 73	< 0.0095	< 101	< 0.0112	< 119
NGC 6503	halo	5.00 \times 7.00	wsrc	18.294	0.0083 \pm 0.0033	88	0.0154 \pm 0.0029	164	0.0097 \pm 0.0050	103

5. Spectral properties of the diffuse emission

5.1. Separation into nuclear, disk and halo components

We created background, and point-source, subtracted ACIS spectra of the nucleus, the disk and the halo for each galaxy and observation thereof. In this paper we will concentrate primarily on the faint extra-planar diffuse emission from the halo region, although we do tabulate fluxes and luminosities of the diffuse X-ray emission from all three regions for each galaxy. These three regions are defined as:

- **Nucleus:** a circular aperture 1 kpc in radius, centered on the nuclear position given in Table 1.
- **Disk:** a rectangular aperture oriented along the major axis of the disk, of sufficient major-axis length to encompass all of the observed diffuse emission, and extending between $-2 \leq z$ (kpc) ≤ 2 along the minor-axis. The nuclear region defined above is *excluded* from the disk region.
- **Halo:** A rectangular aperture oriented along the minor axis of the galaxy, chosen to enclose all observed diffuse emission, but excluding the region with $|z| \leq 2$ kpc of the plane of the galaxy (*i.e.* excluding the disk and nuclear regions defined above).

For all ACIS-S observations (Table 2), only events from the back-illuminated S3 chip that are also within the regions defined above were used to create the X-ray spectra, as the spectral responses of the neighboring front-illuminated S2 and S4 chips are substantially different. We used data from all four ACIS-I chips in creating spectra from the ACIS-I observation of M82.

We have chosen a projected height of $z = 2$ kpc as the dividing line between what we term as the halo and disk regions, based on the minor-axis optical extent of the galaxies, and that the X-ray spectral hardness profiles we observe are relatively uniform for $|z| \geq 2$ kpc. This ensures negligible contamination of diffuse X-ray emission seen within the halo region by hot gas actually within the disk of the galaxy. Note that this does *not* automatically imply that X-ray emission in what we call the disk region is actually within the plane of the galaxy. For the starburst galaxies, it is clear that the majority of the diffuse X-ray emission in both the disk

and nuclear regions is directly associated with outflowing gas.

The angular size of these regions, the area of sky covered, and the observed background subtracted count rate for the nuclear, disk and halo regions for all galaxies are given in Table 7, both with and without point-source removal.

5.2. Hardness ratio analysis

To provide a quantitative cross-comparison of the spectra, the diffuse emission Q_A and Q_B hardness ratios for both halo and disk regions are shown in Fig. 17¹¹.

The spectral hardness of the diffuse halo emission of all the galaxies, both the starburst galaxies (with the exception of the poorly-constrained halo spectrum of NGC 4945) and NGC 891, are generally very similar to each other. M82, NGC 1482 and NGC 3079 are spectrally harder than the other galaxies, but from this form of analysis it is impossible to distinguish whether this is due to a higher mean plasma temperature, or to higher intrinsic absorption.

Disk diffuse emission is significantly spectrally harder than the halo emission, as mentioned earlier. Explaining this as entirely due to increased absorption requires hydrogen columns $N_H \sim 3 \times 10^{21} \text{ cm}^{-2}$ (as can be seen from Fig. 17). This is reasonable given we would expect some fraction of the diffuse X-ray emission to experience absorption by gas and dust in the highly inclined disk, and consistent with the X-ray measurement of the absorption column through an edge-on spiral galaxy disk by Clarke et al. (2003).

5.3. A single common spectral model for all halo emission

Given the apparent spectral similarity of the halo diffuse emission spectra, it is worth asking if they are, in fact, spectrally identical? To answer this question we simultaneously fit all the halo diffuse emission spectra with a two temperature MEKAL (Mewe, Kaastra & Liedahl 1995) hot plasma model. This approach is motivated by the results from many *ROSAT* PSPC and *ASCA* X-ray spectroscopy studies (to name

¹¹For the more distant nuclear starburst galaxies in this sample (e.g. NGC 3628, NGC 3079 or NGC 1482), it is impossible to achieve point source removal in the nuclear regions to same depth as that obtained in the nearer galaxies such as M82 or NGC 253, e.g. see Table 3. For this reason we have not included nuclear region hardness ratios in Fig. 17

TABLE 7—Continued

Galaxy	Region	Size maj. \times min.	Diffuse only?	Area	Soft 0.3-1.0 keV cts/s	tot cts	Medium 1.0-2.0 keV cts/s	tot cts	Hard 2.0-8.0 keV cts/s	tot cts
(1)	(2)	(3)	(4)	(5)	(6)	(7)	(8)	(9)	(10)	(11)
NGC 891	nucl	0.72	diff	0.087	0.0003 \pm 0.0002	8	0.0005 \pm 0.0002	16	0.0001 \pm 0.0002	4
NGC 891	nucl	0.72	wsrc	0.101	0.0002 \pm 0.0002	8	0.0006 \pm 0.0002	18	0.0009 \pm 0.0003	27
NGC 891	disk	9.33 \times 1.43	diff	12.727	0.0235 \pm 0.0020	722	0.0041 \pm 0.0016	125	-0.0074 \pm 0.0027	-226
NGC 891	disk	9.33 \times 1.43	wsrc	13.190	0.0383 \pm 0.0022	1177	0.0560 \pm 0.0021	1720	0.0345 \pm 0.0030	1059
NGC 891	halo	4.40 \times 4.40	diff	12.949	0.0117 \pm 0.0020	360	0.0000 \pm 0.0016	1	-0.0005 \pm 0.0028	-17
NGC 891	halo	4.40 \times 4.40	wsrc	13.050	0.0204 \pm 0.0020	627	0.0083 \pm 0.0017	253	0.0033 \pm 0.0028	101
NGC 4244	nucl	1.90	diff	0.674	0.0003 \pm 0.0002	16	0.0002 \pm 0.0002	8	-0.0004 \pm 0.0002	-18
NGC 4244	nucl	1.90	wsrc	0.681	0.0006 \pm 0.0002	27	0.0002 \pm 0.0002	8	-0.0004 \pm 0.0002	-18
NGC 4244	disk	10.23 \times 3.81	diff	30.685	0.0049 \pm 0.0015	231	0.0023 \pm 0.0012	110	0.0070 \pm 0.0023	335
NGC 4244	disk	10.23 \times 3.81	wsrc	30.968	0.0123 \pm 0.0016	583	0.0087 \pm 0.0013	415	0.0112 \pm 0.0023	530
NGC 4244	halo	8.20 \times 8.20	diff	33.428	0.0002 \pm 0.0016	10	-0.0003 \pm 0.0013	-14	-0.0004 \pm 0.0024	-17
NGC 4244	halo	8.20 \times 8.20	diff	33.428	< 0.0034	< 159	< 0.0024	< 112	0.0045	< 213
NGC 4244	halo	8.20 \times 8.20	wsrc	33.658	0.0063 \pm 0.0017	299	0.0057 \pm 0.0014	269	0.0037 \pm 0.0024	174

NOTE.—Errors are 1σ , calculated using the Gehrels (1986) approximation, and include the uncertainties associated with the background subtraction. Upper limits are exact Poissonian 3σ (99.73% confidence) upper limits. Column 2: Nuclear (nucl), disk or halo region, as defined in § 5.1 Column 3: Size of the spectral region in arcminutes. For nuclear regions the value quoted is the angular diameter of the circular extraction region, corresponding to a physical diameter of 2 kpc. For the disk and halo regions the values are the total r and z -axis angular widths of the rectangular extraction regions. All regions are centered on the positions given in Table 1. The nuclear region is excluded from the disk region, and that both the nuclear and disk regions are excluded from the halo region. Note also that the final area used is the fraction of this geometrical region that falls within the boundaries of the field of view of the S3 chip. Column 4: Count rates where the emission from point sources has been excluded (*i.e.* diffuse X-ray emission only) are noted as diff. Count rates including both diffuse and point source emission are denoted as wsrc. Column 5: Total resulting area, in units of arcmin². Columns 6 through 11: Background-subtracted soft energy band count rate, count rate error, and total number of counts accumulated after background subtraction. Values are given for the soft, medium and hard energy bands.

^aACIS-I observations of M82, ObsIDs 361 and 1302. Data from ACIS-I chips.

^bACIS-S observation of M82, ObsID 2933. Data from the S3 chip only.

^cNGC 253 observation ObsID 969, Data from S3 chip only.

^dNGC 253 observation ObsID 790, Data from S3 chip only.

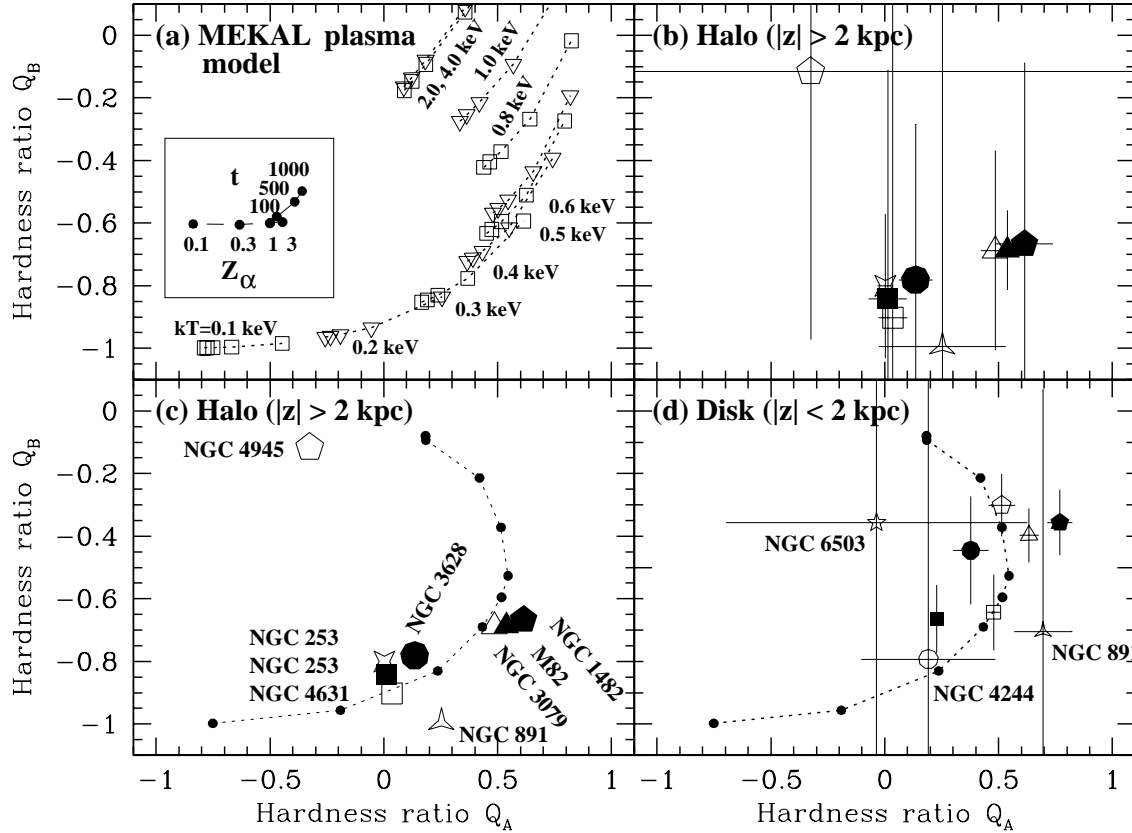


Fig. 17.— Halo and disk diffuse X-ray emission hardness ratios, compared to hardness ratios from a MEKAL hot plasma code simulation. The hardness ratios Q_A and Q_B are defined in Equation 1 (see § 4.3). Only data from the back-illuminated S3 chip is used. Panel (a) shows the hardness ratios expected from a single temperature hot plasma in collisional ionization equilibrium, calculated using the MEKAL model. The plasma is assumed to have Solar ratios of the alpha elements (*i.e.* $Z_{\sim\alpha} = 1 Z_{\odot}$), with the relative abundance of iron and other refractory elements being 1/3 Solar. The use of square and inverted triangular symbols is alternated to aid the reader in distinguishing between predictions for different temperature plasmas in regions where hardness ratios overlap. For each temperature, hardness ratios for hydrogen columns of $N_H = 0, 1, 3, 10$ and $30 \times 10^{20} \text{ cm}^{-2}$ are shown. The lowest column always has the lowest value of Q_A and Q_B . The insert shows the magnitude of hardness ratio changes due to different metal abundances ($Z_{\sim\text{Fe}}$ is always assumed to be 1/3 of the alpha-element abundance), and due to the increasing contamination of the ACIS optical blocking filter (t is days since launch). Panel (b) displays the observed S3-chip hardness ratios for the diffuse emission within the halo region (defined in § 5.2), with 1σ error bars. A different symbol is used for each galaxy — the same symbol is used in panels c and d. Panel (c) displays the same data, sans error bars. Individual galaxies are identified by name. Predicted hardness ratios for a single temperature plasma with temperatures (from lower left) $kT = 0.1, 0.2, 0.3, 0.4, 0.5, 0.6, 0.8, 1.0, 2.0$ and 4.0 keV , $Z_{\sim\alpha} = 1 Z_{\odot}$, $Z_{\sim\text{Fe}} = 0.33 Z_{\odot}$ and $N_H = 3 \times 10^{20} \text{ cm}^{-2}$ are shown as the connected set of small circles. Panel (d) shows the observed S3-chip hardness ratios, with errors, for the diffuse emission found within $z \leq 2 \text{ kpc}$ the disk. The connected set of small circles represent the same predicted hardness ratios as used in panel c.

but a few, Della Ceca et al. 1996; Della Ceca, Griffiths & Heckman 1997; Ptak et al. 1997; Tsuru et al. 1997; Dahlem et al. 1998; Zezas, Georgantopoulos

& Ward 1998; Moran, Lehnert & Helfand 1999), and our detailed *Chandra* study of the diffuse halo emission from NGC 253 (Strickland et al. 2002a). These

studies found that the X-ray spectra of starburst galaxies are usually best-fit by low temperature ($kT \lesssim 0.2$ keV) and a medium temperature ($kT \sim 0.6$ keV) thermal plasma (in addition to a spectrally hard power law component representing X-ray emission from X-ray binaries and low luminosity AGN, in the *ROSAT* PSPC and/or *ASCA* observations which lack the spatial resolution to remove point source emission).

Our aim with this approach is *not* to find a set of models that perfectly fit each of the halo spectra, but rather to see if all of the halo spectra can be fit by the same spectral model, and if not, in what ways does this approach fail? In reality, the halo plasma is unlikely to be in the ionization equilibrium state assumed by the MEKAL model (see the discussion in Strickland & Stevens 2000). Similarly, although two temperature models fit well, a more complex range of temperatures is likely to exist. These, indeed all, best-fit X-ray spectral models of diffuse emission in star-forming galaxies, should only be interpreted as empirical characterizations of the spectra, and not as representing the true physical state of the emitting plasma.

5.3.1. Spectral model description

The basic model we use is a two-temperature, variable-abundance MEKAL hot plasma model (Mewe et al. 1995), incorporating the effects of foreground absorption (using the Solar abundance photoelectric absorption model of Morrison & McCammon 1983) and the molecular contamination of the ACIS optical blocking filters (using version 1.1 of the ACISABS model by G. Chartas & K. Getman, and the observation dates given in Table 2). In terms of the syntax used in the XSPEC spectral fitting program, the model specification is `acisabs*wabs*(vmekal+vmekal)`.

Model parameters that are fit for, and which are forced to have the same value in each spectrum, are the two plasma temperatures kT_S and kT_M , and elemental abundances with respect to hydrogen. In other words, the best-fit values of these parameters are those that provide maximum goodness-of-fit to the collective ensemble of spectra. For each individual spectrum the normalization of each of the two thermal components (K_S and K_M), and the equivalent hydrogen column density of foreground absorption N_H each spectrum experiences, are not tied to a universal, collectively-determined value, but instead are free to assume any best-fit value. As we do not expect large amounts of intrinsic absorption within the halos of these galaxies,

we constrain the fitted column to lie within the range from half to three times the Galactic foreground absorption value (given in Table 3).

5.3.2. Metal abundance fitting

In general, the strongest spectral features visible in *Chandra* ACIS spectra of star-forming galaxies are unresolved emission line complexes due from highly ionized O and Fe, and occasionally-visible weaker spectral emission features from Mg, Ne, Si and S. Visual inspection of the many of the halo-region diffuse emission spectra immediately revealed that the strength of the Fe L-shell complex at $E \sim 0.8$ – 1.0 keV with respect to O VII/O VIII emission $E \sim 0.53$ – 0.65 keV is less than would be expected from a plasma with Solar heavy element abundance ratios¹². We therefore allow for non-Solar ratios of O to Fe in the spectral fit. Given the weakness of spectral features due to other elements, we constrain to abundance of Mg, Si, Ne, S, Ar, C and N with respect to hydrogen to track the fitted O abundance. This value, now with respect to the Solar value, we will refer to as the approximate oxygen abundance $Z_{\sim O}$. We similarly constrain the abundances of Ni, Ca, Al and Na to track the Fe abundance, and refer to this value as the approximate iron abundance $Z_{\sim Fe}$.

5.3.3. Other spectral fitting details

Fitting is only performed to data within the energy range 0.3 – 3.0 keV (slightly different energy ranges were used for the ACIS-I spectrum of M82 and the ACIS-S spectra of NGC 253, of 0.5–3.0 keV and 0.3–2.0 keV respectively). This approach is conservative, in the sense that had we included the spectral data at higher energies in the fit, we would have obtained *lower* values of best-fit reduced chi-squared given the very low 2 – 8 keV count rates in the halo regions (see Table 7).

The spectral model was initialized by choosing parameter values deemed reasonable, based on the discussion given above. Temperatures were initialized at $kT_S = 0.2$ and $kT_M = 0.7$ keV, the foreground hydrogen column at the Galactic value appropriate for

¹²We use as Solar the abundance ratios given by Anders & Grevesse (1989), as this abundance set is most commonly employed within the X-ray community, and have converted any other abundances quoted to this abundance scale. Note that more recent studies give significantly lower values for the Solar abundance of both O and Fe with respect to hydrogen, by 0.20 and 0.16 dex respectively (Grevesse & Sauval 1998; Holweger 2001).

each galaxy (see Table 3), and the metal abundances at $Z_{\sim O} = 1.00 Z_{\odot}$ and $Z_{\sim Fe} = 0.33 Z_{\odot}$. Model normalizations K_S and K_M were chosen so as to provide the best fit to the observed spectra with all other parameters fixed at their initial values. Rather than immediately fitting for all of the model parameters, we initially only fit for the model normalizations and temperatures, leaving other values at their initial values. Once this fit had converged, we let the metal abundance values to also be determined by the fit. Finally we allowed the hydrogen column density to assume a best-fit value.

The minimization technique employed within the XSPEC fitting package is the standard Levenberg-Marquardt method. To avoid the fit getting trapped in local minima of the multi-dimensional fit-space (a common occurrence with this method), we perform a full confidence region calculation for all model parameters after each invocation of the fit command. This has the practical effect of extracting the fit from shallow local minima, as it ensures that the final best-fit values lie in a valley that is at least $\Delta\chi^2 \geq 42.6$ deep (90% confidence for 32 interesting parameters) in fit-space for all parameters. We also performed the fitting using the maximum likelihood C-statistic, but obtained statistically identical results.

5.3.4. Results of the halo-region combined spectral fitting

We find, somewhat to our surprise, that it is possible to obtain a reasonably acceptable model (reduced chi-squared $\chi^2_{\nu} = 1.32$, with 534 degrees of freedom), provided that the relative normalization of the soft and medium temperature thermal components is not the same in all of the galaxies. The ACIS spectra, and the simultaneously-fit two temperature model, are shown in Fig. 18. The best-fit halo model parameters are given in Table 8. Considered on a galaxy-by-galaxy basis, this model does surprisingly well, yielding statistically acceptable fits in several cases, although this is partially due to poorer photon statistics in some of the better fits.

We do not wish to place undue significance on the best fit model parameters, and hence will not convert emission integrals into gas densities and masses. We note that the temperatures of the two thermal components ($kT_S \sim 0.1$ keV and $kT_M \sim 0.4$ keV, see Table 8) are lower than $kT \sim 0.25$ and ~ 0.7 keV components typically found in two temperature *ROSAT* and *ASCA*

fits to the total X-ray spectra of starbursts by Dahlem et al. (1998). This is not surprising, as we are fitting only the halo-region emission, and the hardness ratio profiles demonstrate that the halo emission is spectrally softer than the brighter disk region (which would have dominated the combined *ROSAT* and *ASCA* spectral fitting).

The metal abundances with respect to hydrogen are poorly constrained from the ACIS X-ray spectra (Fig. 19b), as they lack the spectral resolution necessary to resolve lines from the continuum. Our model α -to-iron element ratio is significantly better constrained, $Z_{\sim O}/Z_{\sim Fe} = 2.69^{+0.64}_{-1.02}$ (errors are 68% confidence for 32 parameters of interest), statistically identical to the value Martin et al. (2002) find for the diffuse X-ray emission of the low-metallicity dwarf starburst galaxy NGC 1569. Spectra of X-ray emission with apparently enhanced α -to-iron element ratios in starburst galaxies were first reported by Ptak et al. (1997) and Tsuru et al. (1997) based on the *ASCA* spectroscopy of the entire emission from M82 and NGC 253, but these newer *Chandra* observations finally allow us to be confident that they also apply to the diffuse extra-planar emission.

Although the physical processes behind the X-ray emission are of interest in themselves, it is the gross radiative cooling rate that is of importance in assessing the efficiency with which superwinds can transport energy and metals out of galaxies. The model-derived absorption-and-contamination-corrected X-ray fluxes and luminosities for the halo region of the sample galaxies are given in Table 9. While the raw halo flux is a reasonably robust value irrespective of the specific spectral model (provided the model reproduces the observed count rate reasonably well), the absorption-and-contamination-corrected fluxes are model dependent. We estimate this systematic uncertainty (*i.e.* not knowing what the true emission process is, and oversimplified modeling of probably patchy absorption for the disk regions) makes the intrinsic, absorption corrected, fluxes f_{ABSC} quoted uncertain by a factor ~ 2 . This is likely to dominate over statistical uncertainties, which is why we have not attempted to calculate the formal statistical uncertainties associated with the fitted spectral models.

5.4. Diffuse nuclear and disk emission

For completeness we present diffuse X-ray fluxes and luminosities for the nuclear and disk regions,

TABLE 8
HALO DIFFUSE X-RAY EMISSION SPECTRAL FIT RESULTS AND MEAN SURFACE BRIGHTNESS

Galaxy (1)	N_H (2)	Normalizations		$\langle kT \rangle$ (5)	χ^2_ν (6)	ν (7)	Σ_{HALO}	
		K_S (3)	K_M (4)				0.3–1.0 keV (8)	1.0–2.0 keV (9)
M82 ^a	12.0(L)	0.00(L) (<19.26)	17.05 ^{+28.31} _{-13.79}	0.37	1.40	77	2.88E–09	5.12E–10
M82 ^b	12.0(L)	17.75 ^{+23.44} _{-10.97}	11.57 ^{+12.16} _{-8.25}	0.27	2.35	76	4.36E–09	8.06E–10
NGC 1482	8.79	0.16 ^{+1.71} _{-0.16}	0.41 ^{+1.08} _{-0.26}	0.34	1.26	15	4.57E–09	9.01E–09
NGC 253 ^c	0.70(L)	2.51 ^{+8.40} _{-1.76}	1.28 ^{+2.69} _{-0.52}	0.25	0.84	47	2.82E–09	1.49E–10
NGC 253 ^d	0.70(L)	5.39 ^{+16.01} _{-2.24}	2.39 ^{+5.38} _{-1.47}	0.25	1.78	76	2.28E–09	1.13E–10
NGC 3628	5.05	1.81 ^{+3.07} _{-1.55}	0.61 ^{+1.53} _{-0.27}	0.23	1.19	57	1.19E–09	9.81E–11
NGC 3079	2.4(L)	0.15 ^{+1.69} _{-0.15}	1.46 ^{+2.55} _{-0.48}	0.36	1.17	53	1.30E–09	1.86E–10
NGC 4945	13.9	0.99 ^{+22.47} _{-0.99}	0.14 ^{+4.73} _{-0.14}	0.18	0.49	7	1.80E–10	1.38E–11
NGC 4631	0.65(L)	2.03 ^{+8.05} _{-1.02}	0.81 ^{+1.72} _{-0.20}	0.24	1.28	58	1.08E–09	5.70E–10
NGC 6503	<3.57E–10	<2.22E–10
NGC 891	7.80	0.99 ^{+15.70} _{-0.99}	0.31 ^{+1.11} _{-0.31}	0.23	0.54	21	7.18E–10	6.84E–11
NGC 4244	<9.14E–11	<2.88E–11

NOTE.—Results from the two temperature MEKAL hot plasma model fit made simultaneously to all the halo region spectra. See § 5.3 for further details. Other best-fit model parameters are $kT_S = 0.11^{+0.03}_{-0.02}$ keV, $kT_M = 0.37^{+0.03}_{-0.03}$ keV, $Z_{\sim O} = 0.94^{+19.1}_{-0.64} Z_\odot$, $Z_{\sim Fe} = 0.35^{+10.8}_{-0.22} Z_\odot$ (the ratio $Z_{\sim O}/Z_{\sim Fe} = 2.69^{+0.64}_{-1.02}$ is better constrained) with a final reduced chi-squared value of $\chi^2_\nu = 1.32$ ($\chi^2 = 706.6$, number of degrees of freedom $\nu = 534$). Unless specified otherwise below, the quoted errors represent a $\Delta\chi^2 = 42.58$ (90% confidence for 32 parameters of interest). Model parameters marked as (L) represent a lower or upper limit imposed upon the fit. Column 2: Best-fit column density (assuming Solar abundances) in units of 10^{20} cm^{-2} . Columns 3 and 4: Model normalizations for the soft and medium temperature thermal components. The normalization $K = 10^{-10} EI/4\pi D^2$, where the volume emission integral $EI = \eta_X n_e n_H V$ and D the source distance in cm. Column (5): The X-ray luminosity weighted mean temperature in keV, $\langle kT \rangle = (kT_S f_{X,S} + kT_M f_{X,M}) / (f_{X,S} + f_{X,M})$, where $f_{X,S}$ and $f_{X,M}$ are the absorption-corrected X-ray fluxes produced by the two thermal components in the 0.3–2.0 keV energy band. Columns 6 and 7: Reduced χ^2_ν value and number of degrees of freedom, if the best-fit model was applied to this alone. Columns 8 and 9: Halo region X-ray mean surface brightness (photons $\text{s}^{-1} \text{ cm}^{-2} \text{ arcsec}^{-2}$) derived from the ACIS spectra, in the 0.3–1.0 and 1.0–2.0 keV energy bands, averaged over the area given in Table 7. These surface brightnesses have the same physical meaning as the surface brightness values derived from the ACIS images discussed in § 4.1, *i.e.* an estimate of the X-ray photon flux in that energy band immediately *prior* to passing through the telescope’s optics.

^aACIS-I observations of M82, ObsIDs 361 and 1302. Data from ACIS-I chips, covering the majority of the extra-planar diffuse emission, but not extending as far as the northern cloud.

^bACIS-S observation of M82, ObsID 2933. Data from the S3 chip only, which does not cover the full extent of the diffuse emission.

^cNGC 253 observation ObsID 969. Only a small fraction of the Northern halo lies on the S3 chip.

^dNGC 253 observation ObsID 790. Data from S3 chip only, covering most of the bright diffuse emission in the Northern halo.

TABLE 9

HALO, DISK, NUCLEAR AND TOTAL DIFFUSE THERMAL X-RAY FLUXES AND LUMINOSITIES

Galaxy (1)	Halo region X-ray flux and luminosity					Disk region X-ray flux and luminosity					Nuclear region X-ray flux and luminosity				Total X-ray flux and luminosity		
	f_{Raw} (2)	f_{OBFC} (3)	f_{ABSC} (4)	$L_{\text{X,H}}$ (5)	$f_{\text{X,H}}/f_{\text{FIR}}$ (6)	f_{OBFC} (7)	f_{ABSC} (8)	$L_{\text{X,D}}$ (9)	$f_{\text{X,D}}/f_{\text{FIR}}$ (10)	f_{OBFC} (11)	f_{ABSC} (12)	$L_{\text{X,N}}$ (13)	$f_{\text{X,N}}/f_{\text{FIR}}$ (14)	f_{ABSC} (15)	$L_{\text{X,T}}$ (16)	$f_{\text{X,T}}/f_{\text{FIR}}$ (17)	
M82 ^a	1.4E-12	1.4E-12	2.7E-12	4.1E39	4.43E-5	4.0E-12	1.0E-11	1.6E40	1.73E-4	3.4E-12	1.5E-11	2.3E40	2.47E-4	2.8E-11	4.3E40	4.62E-4	
M82 ^b	8.0E-13	1.2E-12	2.9E-12	4.5E39	4.82E-5	5.9E-12	1.8E-11	2.8E40	2.97E-4	3.1E-12	1.8E-11	2.8E40	3.00E-4	3.9E-11	6.0E40	6.45E-4	
NGC 1482	2.9E-14	4.3E-14	7.4E-14	4.3E39	4.28E-5	1.6E-13	4.8E-13	2.8E40	2.78E-4	4.7E-14	7.4E-14	4.3E39	4.27E-5	6.3E-13	3.7E40	3.64E-4	
NGC 253 ^c	2.7E-13	3.3E-13	3.5E-13	2.9E38	6.51E-6	1.2E-12	4.1E-12	3.3E39	7.57E-5	6.9E-13	1.2E-12	9.4E38	2.15E-5	
NGC 253 ^d	5.3E-13	6.5E-13	7.0E-13	5.7E38	1.30E-5	
NGC 253 ^e	1.5E-12	1.2E39	2.72E-5	1.2E-12	4.1E-12	3.3E39	7.57E-5	6.9E-13	1.2E-12	9.4E38	2.15E-5	6.8E-12	5.5E39	1.25E-4	
NGC 3628	8.4E-14	1.3E-13	2.1E-13	2.5E39	6.65E-5	6.4E-14	2.2E-13	2.6E39	7.14E-5	9.0E-15	2.0E-14	2.4E38	6.46E-6	4.4E-13	5.3E39	1.44E-4	
NGC 3079	1.5E-13	2.0E-13	2.4E-13	8.3E39	8.05E-5	2.4E-13	6.7E-13	2.3E40	2.26E-4	1.4E-14	2.9E-14	1.0E39	9.90E-6	9.2E-13	3.2E40	3.14E-4	
NGC 4945	1.8E-14	2.2E-14	8.2E-14	1.3E38	2.22E-6	2.9E-13	1.8E-12	2.9E39	4.80E-5	9.0E-14	2.2E-13	3.7E38	6.10E-6	2.1E-12	3.4E39	5.62E-5	
NGC 4631	1.7E-13	2.3E-13	2.5E-13	1.7E39	4.81E-5	2.9E-13	9.0E-13	6.1E39	1.73E-4	6.2E-15	9.2E-15	6.2E37	1.78E-6	1.2E-12	7.8E39	2.23E-4	
NGC 6503 ^f	<4.9E-14	<1.6E38	<7.03E-5	4.8E-14	1.9E-13	6.0E38	2.68E-4	1.5E-14	3.4E-14	1.1E38	4.91E-5	2.2E-13	7.1E38	3.17E-4	
NGC 891	3.7E-14	5.3E-14	1.1E-13	1.2E39	2.41E-5	9.1E-14	4.2E-13	4.7E39	9.44E-5	4.6E-15	1.1E-14	1.2E38	2.42E-6	5.4E-13	6.0E39	1.21E-4	
NGC 4244 ^f	<1.6E-14	<2.5E37	<4.67E-5	1.4E-14	3.4E-14	5.3E37	9.91E-5	3.7E-15	7.7E-15	1.2E37	2.25E-5	4.1E-14	6.5E37	1.22E-4	

NOTE.—All X-ray fluxes and luminosities quoted are in the 0.3–2.0 keV energy band, and refer to the diffuse thermal emission components of the best-fit spectral models alone. Columns 2, 3 and 4: Model-derived halo-region diffuse X-ray flux, in units of $\text{erg s}^{-1} \text{cm}^{-2}$ in the 0.3–2.0 keV energy band. No corrections for the absorption or the contamination of the ACIS optical blocking filter have been made to f_{Raw} . Estimated fluxes corrected for the optical blocking filter contamination are given in column 3 (f_{OBFC}), while absorption-and-contamination-corrected fluxes are given in column 4 (f_{ABSC}). Column 5: Halo region 0.3–2.0 keV energy band diffuse X-ray luminosity (erg s^{-1}), based on f_{ABSC} and the distances given in Table 1. Column 6: Ratio of the X-ray luminosity from thermal emission in the halo region of each galaxy to the total galactic far-infrared flux estimated from the IRAS 60 μm and 100 μm flux densities, where $f_{\text{FIR}} = 1.26 \times 10^{-11} \times (2.58 \times f_{60} + f_{100})$, in units of $\text{erg s}^{-1} \text{cm}^{-2}$, where f_{60} and f_{100} are given in units of Jy. Columns 7 to 10: Disk region diffuse thermal X-ray fluxes, luminosities and X-ray to FIR flux ratios. Columns 11 to 14: Nuclear region diffuse thermal X-ray fluxes, luminosities and X-ray to FIR flux ratios. Columns 15 to 17: Total thermal X-ray absorption-corrected X-ray flux, luminosity and X-ray to FIR flux ratio, *i.e.* the sum of the thermal emission from the nuclear, disk and halo regions. For NGC 6503 and NGC 4244 these totals ignore any contribution from the halo region.

^aACIS-I observations of M82, ObsIDs 361 and 1302. Data from ACIS-I chips, covering the majority of the extra-planar diffuse emission, but not extending as far as the northern cloud.

^bACIS-S observation of M82, ObsID 2933. Data from the S3 chip only, which does not cover the full extent of the diffuse emission.

^cNGC 253 observation ObsID 969. Only a small fraction of the Northern halo lies on the S3 chip.

^dNGC 253 observation ObsID 790, Data from S3 chip only, covering most of the bright diffuse emission in the Northern halo.

^eFluxes and luminosities covering all of NGC 253 and its wind. We estimate that the northern halo region covered by the ObsID 790 observation accounts for $\sim 48\%$ of the total halo region flux (*i.e.* both sides of the planes of the galaxy) from NGC 253, based comparison of the estimated halo diffuse count rate in the *ROSAT* PSPC observation. Scaling the fluxes obtained from the *Chandra* observation, the total 0.3–2.0 keV energy band diffuse X-ray flux from both the north and south of the plane is $f_{\text{ABSC}} \sim 1.47 \times 10^{-12} \text{ erg s}^{-1} \text{ cm}^{-2}$ ($L_{\text{X}} \sim 1.2 \times 10^{39} \text{ erg s}^{-1}$).

^fUpper limits of the X-ray flux from diffuse gas in the halos of NGC 6503 and NGC 4244 were calculated from the 3σ upper limits on the 0.3–2.0 keV diffuse emission count rate (0.0122 and 0.0040 cts s^{-1} respectively), and an ACIS S3 chip count rate to absorption-corrected flux conversion factor of $4 \times 10^{-12} \text{ erg s}^{-1} \text{ cm}^{-2} (\text{cts s}^{-1})^{-1}$.

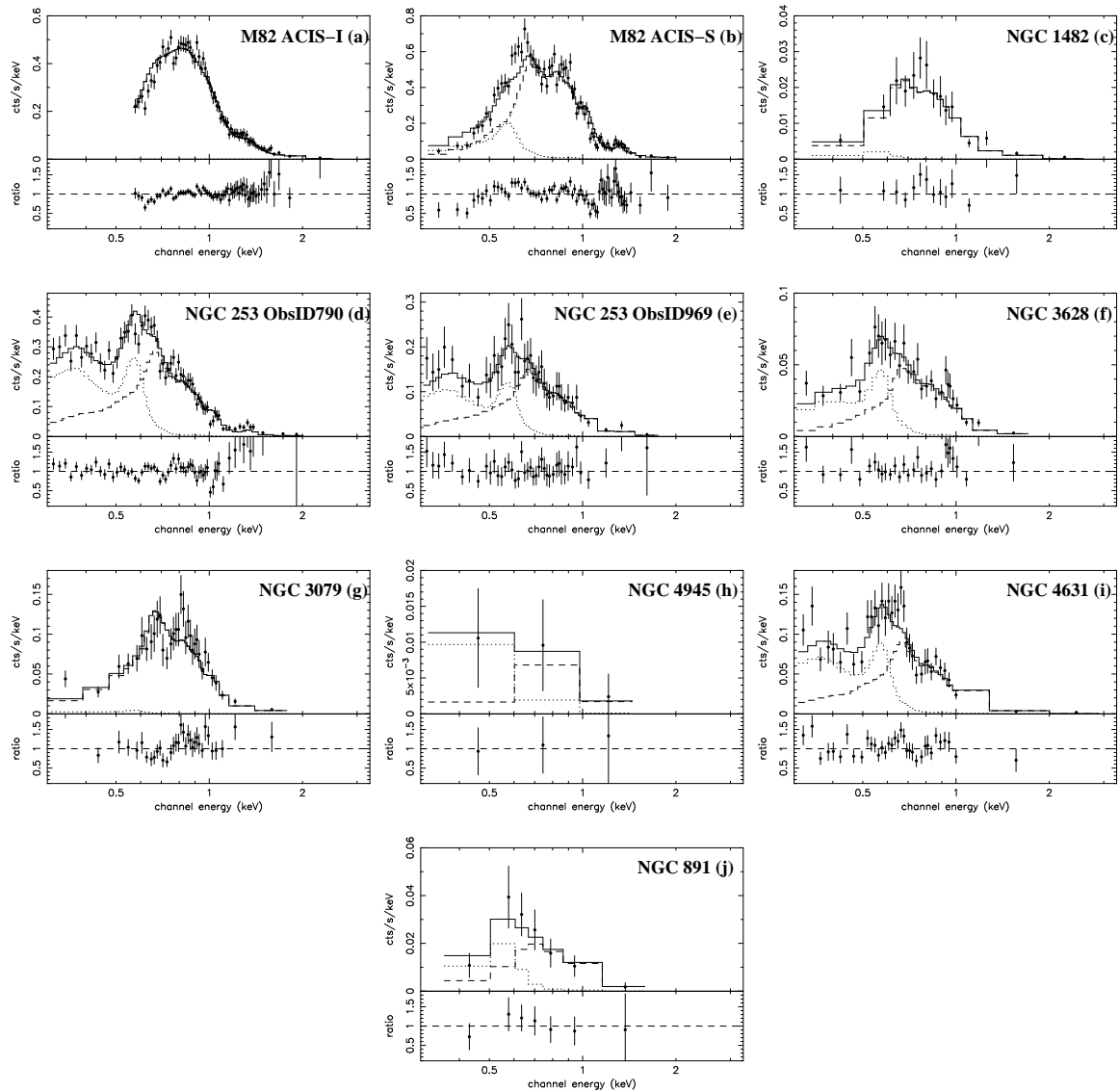


Fig. 18.— *Chandra* ACIS X-ray spectra of the diffuse X-ray emission from the halo regions ($|z| \geq 2$ kpc) of the sample galaxies. The top of each panel shows the observed spectrum (solid points with 1σ error bars), along with a solid line showing the best-fit two thermal component model (simultaneously fit to all the spectra — see § 5.3). The individual $kT = 0.37$ keV and $kT = 0.11$ keV thermal components are represented by the dashed and dotted lines respectively. The lower part of each panel is the ratio of the data to the model.

along with totals (summing nuclear, disk and any halo region diffuse X-ray emission) in Table 9. The nuclear and disk region diffuse flux are also based on simultaneous fits.

Simultaneous fitting of the nuclear and disk region spectra was more difficult than for the halo as the spectra are more complex, and in terms of reduced

χ^2_ν values these nuclear and disk region combined fits are worse than the combined halo region best-fit, with $\chi^2_\nu = 2.15$ (952 degrees of freedom) and 2.02 (1200 degrees of freedom) respectively. There are several reasons why model fitting to the nuclear and disk region spectra is more complicated than for the halo. Firstly these spectra typically have higher signal to

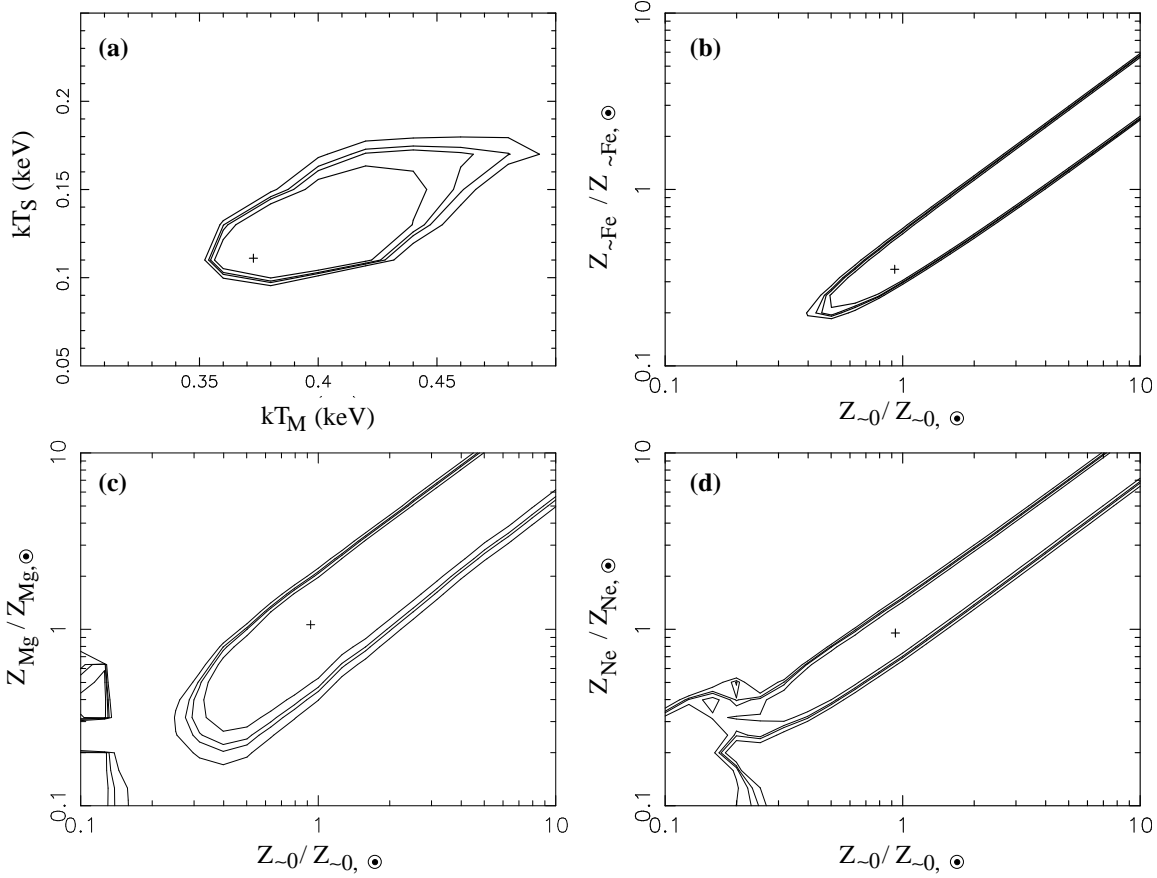


Fig. 19.— Two-dimensional confidence regions from the combined best-fit spectral model for the diffuse halo emission, for the temperatures of the two hot plasma components (panel a) and the abundance measures $Z_{\sim 0}$ and $Z_{\sim Fe}$ (panel b). The best-fit value is marked as a cross. Solid contours are shown at $\Delta\chi^2$ of 35.2, 42.6, 46.2 and 53.5 from the best-fit value (corresponding to the 68.3, 90.0, 95.0 and 99% confidence regions for 32 interesting parameters). In panels c and d the confidence regions are of the magnesium abundance, and the neon abundance, with respect to oxygen and the other α -elements respectively. Again contours corresponding to 68.3, 90.0, 95.0 and 99% confidence are plotted, now for 33 interesting parameters.

noise than the halo region spectra. Secondly, residual contamination by point sources is immediately apparent in the disk and nuclear spectra as a hard power-law continuum above energies of $E \sim 2$ keV, which adds an additional model component to the fits. Thirdly, the diffuse component of the spectra is not well modeled as a two temperature plasma with uniform foreground absorption. For both nuclear and disk spectral fits we used an additional model component that physically represents patchy absorption, where a significant fraction of the diffuse X-ray emission passes through absorption equivalent to a hydrogen column of $N_H \sim 3 \times 10^{21} \text{ cm}^{-2}$. The fit to the nuclear region

spectra also required the presence of the much hotter thermal component, with $kT = 5$ keV, in the M82 spectra. The normalization of this third thermal component was found to be negligible in the other galaxies, except for NGC 1482 and NGC 4945.

We shall reexamine the X-ray temperature and abundance properties of the disk and nuclear regions in more detail in a future paper, where the application of updated spectral calibration should lead to better fits. For convenience we reproduce only the model-derived thermal-component fluxes and luminosities (*i.e.* we quote only the fluxes associated with thermal emission components, ignoring the power law model compo-

ment used to fit for residual point source X-ray emission) in this paper, which are given in Table 9, along with the total diffuse component X-ray flux for each galaxy. The primary source of uncertainty in these numbers is again systematic, so the fluxes are unlikely to become more accurately known even after improved spectral calibrations of ACIS become available.

Our method treats spectrally distinct regions (disk vs. halo, and nucleus vs. disk) separately, and thus goes much of the way toward resolving out the spatial variations in spectral properties that can complicate and distort the results of standard X-ray spectral fitting (see the discussion in Weaver, Heckman & Dahlem 2000; Dahlem et al. 2000). The total diffuse-component X-ray fluxes quoted in Table 9 should therefore be more robust and accurate than previous flux estimates based on fitting models to the summed X-ray emission from each galaxy in its entirety, the only method available given the low spatial resolution and sensitivity of *ROSAT* and *ASCA*.

5.5. Distinguishing between α -element enhancement or depletion of iron onto dust

Martin et al. (2002) present a plausible case for the direct observation of metal-enriched X-ray-emitting gas in the ACIS observation of the low mass dwarf starburst galaxy NGC 1569 ($v_{\text{rot}} \sim 30 \text{ km s}^{-1}$). Despite having many more photons in our halo region spectra, we can not automatically make the same claim.

Martin et al.'s case is convincing as their best-fit oxygen abundance $Z_{\text{O}} \sim 1 Z_{\odot}$ (greater than $0.25 Z_{\odot}$ at 99% confidence) is higher than the ambient ISM oxygen abundance of $\sim 0.2 Z_{\odot}$ of this dwarf galaxy. Our best-fit combined *halo* region oxygen abundance is similarly $Z_{\text{O}} \sim 1 Z_{\odot}$, but in the much more massive galaxies of our sample the ambient ISM of the disk will have such a metallicity (Tremonti et al. in preparation). The high α -to-Fe ratio can be explained as some residual depletion of the iron on dust grains, assuming the X-ray emission comes from gas originally part of the disk, there being considerable evidence for dust in superwind outflows (e.g. Radovich, Kahanpää & Lemke 2001; Heckman 2001; Sugai et al. 2003; Shapley et al. 2003). Dust destruction by sputtering has a timescale comparable to the 10^7 – 10^8 year timescale appropriate for winds and fountains (Popescu et al. 2000), so it is plausible that some fraction of the refractory elements are retained on dust grains in even hot halo gas.

To test this hypothesis we investigated the abundances of the refractory α -elements magnesium and silicon, and the volatile element neon, with respect to oxygen. For each of these three elements, we allowed its abundance to fit independently of the oxygen-dominated α -element group it had previously been assigned to, and then measured its abundance relative to oxygen (see panels c and d in Fig. 19). As the confidence space is poorly behaved for low absolute abundances, we measure this ratio at $Z_{\sim \text{O}} = 1 Z_{\sim \text{O}, \odot}$.

The measured values are given in Table 10. For comparison, we also reproduce the observed abundance pattern of warm ionized gas in the halo of our own galaxy (from Savage & Sembach 1996), and theoretical predictions for nucleosynthesis in SNe taken from Gibson, Loewenstein & Mushotsky (1997).

The observed halo-region abundance pattern is consistent with massive star enrichment, lying close to the broad range of possible Type II SN ejecta abundance patterns collected by Gibson et al. (1997), although the theoretical yields predict a slightly higher ratio of iron to oxygen than observed. Gas as heavily depleted as the warm halo gas of the Milky Way is ruled out. However, without either knowing the Mg/O or Si/O ratios to within approximately ± 0.1 dex, or (preferably) the abundances with respect to hydrogen, it is currently impossible to rule out some form of a depletion scenario for the hot X-ray-emitting gas.

Finally, some caution is warranted as this analysis relies upon the temperature structure of emitting plasma being accurately modeled.

6. Discussion

6.1. A physical interpretation of the quasi-isothermal, semi-exponential surface brightness profiles in the starburst galaxies

The general features of the extra-planar emission (namely spatially-correlated X-ray and $\text{H}\alpha$ emission, often with apparent limb-brightening, soft thermal spectra with little or no significant spectral variation with increasing height above the plane, and a semi-exponential X-ray surface brightness profile) are similar in all of the starburst galaxies with detected halo diffuse X-ray emission. These are the same empirical properties considered in our discussion of the physical origin of the halo emission in NGC 253 (see § 7 of Strickland et al. 2002a), to which we refer the reader.

Our favored models for explaining the extra-planar

TABLE 10
RELATIVE ELEMENT ABUNDANCES

	[Fe/O]	[Mg/O]	[Si/O]	[Ne/O]
Observed hot halo emission	$-0.43^{+0.14}_{-0.08}$	$0.06^{+0.21}_{-0.29}$	< 0.60	$0.01^{+0.14}_{-0.15}$
Warm Galactic halo ^a	-0.80	-0.55	-0.30	...
Type II SN averaged over IMF, A96 ^b	-0.08	0.13	...	-0.05
Type II SN averaged over IMF, T95 ^b	-0.32	-0.01	0.01	-0.17
Type II SN averaged over IMF, W95;A; $10^{-4} Z_{\odot}$ ^b	-0.20	-0.18	0.25	-0.21
Type II SN averaged over IMF, W95;B; $10^{-4} Z_{\odot}$ ^b	-0.39	-0.17	0.04	-0.10
Type II SN averaged over IMF, W95;A; Z_{\odot} ^b	-0.19	-0.10	0.14	-0.11
Type II SN averaged over IMF, W95;B; Z_{\odot} ^b	-0.23	-0.08	0.07	-0.08
Type Ia SN, TNH93 ^b	1.55	-0.05	1.16	-0.75

NOTE.—All errors represent 90% confidence, upper limits are 99.73% confidence (3σ). Abundance ratios are relative to the scale presented in Anders & Grevesse (1989).

^aFrom Savage & Sembach (1996).

^bTaken from compilation of IMF-averaged yields presented by Gibson et al. (1997). See Gibson et al. (1997) for details and nomenclature.

X-ray and $H\alpha$ emission was that the outflowing superwind was interacting with a tenuous and dusty thick-disk/halo medium, itself possibly driven into the lower halo by fountain activity. The limb-brightened X-ray emission might either arise in a shell of shock-heated ambient halo gas (see Fig. 11c of Strickland et al. 2002a), or from metal-enriched wind material that has been compressed in reverse shocks near the walls of the outflow (Fig. 11d of Strickland et al. 2002a).

The filamentary structures visible in even heavily smoothed X-ray images, and their similarity and close spatial association with extra-planar $H\alpha$ filaments on both small and large scales (scales of 10's of pc and kiloparsecs respectively), are compelling evidence that the X-ray emission is not from a volume-filling component of the wind (for a more detailed discussion of this, see Strickland et al. 2000, 2002a).

The observed abundances patterns are consistent with either of these interpretations (§ 5.3), although with higher quality data and a better understanding of the spectra they could be used to distinguish between these two scenarios.

Our finding from this paper, of semi-exponential or Gaussian vertical X-ray surface brightness distributions, are consistent with first scenario, and do not rule out the second scenario. Exponential or Gaussian minor-axis density distributions are expected in both galactic fountain models (see Bregman 1980; Collins, Benjamin & Rand 2002) and the cosmological accretion models (Sommer-Larsen et al. 2002). The dis-

tribution of X-ray emission from halo gas shocked by a superwind will mirror the original halo gas distribution. Optical studies of edge-on star-forming galaxies that have extra-planar warm ionized gas (see Wang, Heckman & Lehnert 1997; Hoopes, Walterbos & Rand 1999; Collins et al. 2000; Miller & Veilleux 2003, and references therein) find emission scale heights of order a few kpc, similar to those we have found in the diffuse X-ray emission. Provided that the temperature of the gas does not vary significantly with z , as we observe, then the X-ray surface brightness profile expected from these models will also be semi-exponential or Gaussian, with a characteristic scale-height half that of the underlying density distribution. Assessing the expected observational properties of the second scenario is non-trivial, and we defer further consideration of this to a future paper.

In contrast, X-ray emission from a volume-filling component of the wind will produce a power-law X-ray surface brightness profile (Chevalier & Clegg 1985), with $\Sigma \propto z^{-3}$. Note that this applies to almost any model with emission from a volume-filling component, including mass-loaded models with observationally-motivated conical outflow geometries Suchkov et al. (1996). This is further evidence that the observed X-ray emission in superwinds is not dominated by a heavily-mass-loaded volume-filling component of the wind, despite some claims to the contrary (e.g. Schurch et al. 2002; Pietsch et al. 2001).

In either of the two scenarios discussed above we require the presence of a pervasive gaseous halo. This

suggests that the disk/halo interaction may be more fountain-like (e.g. Shapiro & Field 1976; Bregman 1980), rather than the more localized chimney model of Norman & Ikeuchi (1989), given the need to produce a widespread halo medium. In this case, it may be possible to use superwinds as a probe of the pre-existing halo properties (e.g. Sofue & Vogler 2001).

6.2. No current need to propose AGN-driving

When presenting this work, we are often asked “NGC 4945 and NGC 3079 have AGN. Is there any evidence that AGN play a role in creating the large-scale winds you see?”

The best answer currently available is that they do not. Take the simplest assumption, that the more radiatively-luminous AGN can also supply more mechanical energy into the ISM. Then, if AGN contributed in any significant way to powering the winds, we would expect galaxies with the most powerful AGN to also to have the notably luminous, spatially extended and/or kinematically powerful winds. Instead, there is no obvious correlation between the presence and luminosity of any AGN and any superwind property. Of the three intrinsically-most X-ray luminous, highest surface-brightness galaxies in this sample, M82, NGC 1482 and NGC 3079, only NGC 3079 has an AGN (which does not obviously have any direct relationship to the wind, as discussed in § 4.2.5) NGC 4945, the most powerful AGN in this sample, is in no way spectacular. The nuclear outflow cone is very similar in X-ray luminosity ($L_X \sim 10^{38}$ erg s⁻¹) and size (~ 500 pc, see Schurch et al. 2002) to that in NGC 253 (which has a low luminosity AGN, see Weaver et al. 2002), and has lower outflow velocities than M82 or NGC 3079. X-ray emission from the halo of NGC 4945 is weak, if present at all.

A more quantitative answer to this question is difficult to present. Heckman et al. (1990) show that the shape of the optically-derived pressure profiles in the central few kpc of many superwind galaxies *exclude* AGN-driving, as expected for clouds embedded in a Chevalier & Clegg (1985) style wind model with a distributed source of energy and mass (*i.e.* a starburst) — indeed, this is one of the reasons the Chevalier & Clegg model is still used despite the lack of a direct observational detection of the merged SN and stellar wind ejecta that drives superwinds. No pressure profile is available for NGC 4945, but the pressure profile for NGC 3079 is possibly consistent with distributed

energy and mass injection (Heckman et al. 1990).

Supernova-driving was originally suggested for the winds in NGC 3079 and NGC 4945 for a variety of reasons, but one significant physical reason is that the estimated rates of *mechanical* energy return to the ISM by SNe were more than sufficient to power the outflows. The same can not be said for AGN. It is far from clear what the relationship is between the power an AGN radiates in any waveband, and energy it may transfer to the ISM, and/or to the powering of jets.

Without further methods to quantitatively test or directly falsify the AGN-driving hypothesis, we feel that the question of whether AGN-driving is important in galaxies such as NGC 4945 and NGC 3079 is not a meaningful issue to raise at this time. In any case, the burden of proof lies with the advocates of AGN-driving for NGC 4945 and NGC 3079..

Seyfert nuclei and LLAGN may well drive weakly-collimated galactic outflows in galaxies without obvious starbursts, e.g. NGC 2110 and NGC 2992 (Weaver et al. 1995; Colbert et al. 1996a,b; Veilleux, Shopbell & Miller 2001). Our argument is that in the “classic” starburst galaxies of this sample, and most probably in Seyfert galaxies with starbursts (for the reasons presented in Levenson, Weaver & Heckman 2001a,b), it is the starburst that is the dominant cause and driver of the outflow.

6.3. The similarity in extra-planar gas properties between NGC 891 and the starburst galaxies

The similarity between the properties of the extra-planar emission around the normal spiral NGC 891 and that around the starburst galaxies is intriguing. The $f_{X,HALO}/f_{FIR}$ and $f_{X,HALO}/f_{1.4GHz}$ flux ratios of NGC 891 are consistent with the values found in the starbursts. In addition, the extra-planar X-ray emitting gas in NGC 891 is accompanied by extra-planar optical emission, again similar to the apparently ubiquitous coupling of H α and X-ray emitting gas in the starbursts. The implication is that the physical conditions in the extra-planar gas around NGC 891 are very similar to those in the optical and X-ray emitting gas in starburst-driven superwinds.

Read & Ponman (2001) suggest that it is possible, using the spectral properties of the diffuse X-ray emission, to distinguish between “coronal” systems (galaxies with static hot halos and/or fountains) and “wind” systems (galaxies with starburst-driven superwinds). In physical terms this is plausible — the temperature

of hot gas in static or fountain-type halos should be less than or similar to the halo virial temperature, while in winds the gas temperature can easily be higher than virial temperature (although it might also be lower, and show no correlation with the host galaxy mass at all).

Our best-fit halo spectral model, essentially dominated by the spectra of the starburst galaxies, provides a good fit to the halo X-ray spectrum of the “normal” spiral NGC 891. When considered in terms of a simple hardness-ratio analysis (§ 5.2), or based on the spectral modeling in § 5.3 (e.g. the luminosity-weighted gas temperatures shown in Table 8), we find no significant spectral difference between the X-ray-emitting gas halos of starburst galaxies and the one normal galaxy (other than the Milky Way) currently known to have hot gas in its halo.

As our sample includes all of the edge-on galaxies on which Read & Ponman’s suggestion is based, why do we come to different conclusions? Read & Ponman assume that NGC 891 and NGC 4631 represent examples of semi-static halos. Of the approximately edge-on systems in their sample, these two galaxies have the lowest diffuse emission temperatures, based on single temperature spectral fits to point-source-subtracted *ROSAT* PSPC spectra of the *entire* galaxy. In terms of luminosity-weighted mean temperature, or spectral hardness, the *Chandra* observation-derived *halo* spectra of NGC 891 and NGC 4631 are no cooler or spectrally softer than the halos of NGC 253 or NGC 3628 — galaxies with clear galactic winds.

The physical interpretation of what drives the observed characteristic halo emission temperature, or temperatures, remains an open, and important question. Nevertheless, we would argue that evidence for a spectral difference between hot gas in the halos of normal galaxies and that in the halos of starburst galaxies, or evidence to allow a separation between “coronae” (or fountains) and “winds,” is currently lacking.

7. Summary

We present a detailed study of the diffuse X-ray emission in a sample of 10 approximately edge-on disk galaxies (7 starburst galaxies, 3 normal spirals) that span the full range of star formation found in disk galaxies. With the arcsecond spatial resolution of the *Chandra* X-ray telescope we are able to robustly separate the X-ray emission from point sources from the truly diffuse component. *Chandra* is the first, and only, X-ray telescope with the spatial resolution sufficient

to allow a meaningful comparison of the spatial location of the X-ray emission to observations of the host galaxies at other wavelengths, in particular to ground or space-based optical imaging. In addition to a detailed discussion of each galaxy, we have presented a mini-atlas of soft and hard X-ray, $H\alpha$ and R-band images of each of the 10 galaxies, shown at a common spatial and surface brightness scale to facilitate cross-comparison.

We consider a variety of quantitative measures of the spatial extent, spectral hardness, and shape of the minor axis surface brightness profiles, several of which can be applied to future samples of galaxies with lower S/N data. We find that the spectral properties of the diffuse X-ray emission show only weak, or some cases no, variation with increasing height (outside an absorbed region within $z \sim 2$ kpc of the disk mid-plane). The vertical decrease in surface brightness of the extra-planar emission ($|z| \geq 2$ kpc) appears to be better described by exponential (effective surface brightness scale heights are typically between 2–4 kpc), or Gaussian models, than the power law expected of a freely expanding fluid.

For the eight galaxies with detections of extra-planar diffuse emission, we find that a common spectral model, comprising a two-temperature MEKAL hot plasma model with an enhanced α -to-Fe element ratio, can fit the ACIS X-ray spectra. The X-ray-derived metal abundances show super-Solar ratios of α -process elements (primarily oxygen) to iron. This is consistent with the origin of the X-ray emission being either (metal-enriched) merged SN ejecta, or from shocked halo gas (with moderate remaining depletion of refractory elements onto dust). We wish to stress that with the present quality of X-ray spectroscopic data, high α /Fe ratios in X-ray emitting plasma are not an automatic indication of massive star SN enrichment.

The spectral and spatial properties of the one normal galaxy in which extra-planar diffuse X-ray emission is detected (NGC 891), are consistent with those of the starburst galaxies, many of which show unambiguous evidence for galactic scale outflows (superwinds). Does this mean that NGC 891 is driving a global wind, or is the similarity of its halo to the superwinds simply due to similar emission processes occurring in both fountains and superwinds? More observation effort needs to be expended on deep X-ray observations of edge-on normal spiral galaxies, before we will fully understand the structure and physics of

the disk/halo interface in star-forming galaxies.

Our favored model for the origin of the extra-planar soft X-ray emission is that SN feedback in the disks of star-forming galaxies create, via blow out and venting of hot gas from the disk, tenuous exponential atmospheres of density scale height $H_g \sim 4 - 8$ kpc. AGN-driven winds do not appear to be significant in this sample, in that there is no obvious correlation between the presence and luminosity of any AGN and the properties of the diffuse X-ray emission. The soft thermal X-ray emission observed in the halos of the starburst galaxies is either pre-existing halo medium (which has been swept-up and shock-heated by the starburst-driven superwinds) or from a *small fraction* (by volume) of the merged-SN-ejecta that has been compressed near the walls of the outflow (e.g. by a reverse shock propagating back into the outflowing wind). In either case the observed exponential X-ray surface brightness distributions are an inheritance from galactic fountain activity prior to the currently-observed starburst phase. This model is based on the qualitative 2-D morphology of the diffuse X-ray and optical $H\alpha$ emission (in particular the filamentary, occasionally limb-brightened morphology of both the X-ray and $H\alpha$ emission), as well as interpretation of the more-quantitative minor axis surface brightness and spectral hardness profiles. One important implication of this model is that galactic-scale gaseous halos may be common around star-forming disk galaxies. Observing starburst galaxies, in which superwinds “light-up” these pre-existing halos, may present the best method for studying the gaseous halos of star-forming galaxies.

Over the several years this project has been in the making, we have have been fortunate to benefit from the insightful comments and questions of many astronomers, too numerous to mention individually, to whom we extend our thanks. The anonymous referee deserves thanks for her or his constructive criticism. We would also like to thank S. Hameed for providing us with R-band and $H\alpha$ images of NGC 1482, and for drawing the attention of the community to this previously ignored but very interesting superwind galaxy.

DKS is supported by NASA through *Chandra* Postdoctoral Fellowship Award Number PF0-10012, issued by the *Chandra* X-ray Observatory Center, which is operated by the Smithsonian Astrophysical Observatory for and on behalf of NASA under contract NAS8-39073.

This research is partially based on data from the ING Archive. This publication makes use of data products from the Two Micron All Sky Survey, which is a joint project of the University of Massachusetts and the Infrared Processing and Analysis Center/California Institute of Technology, funded by the National Aeronautics and Space Administration and the National Science Foundation. Furthermore, this research has made use of the extremely-useful NASA/IPAC Extragalactic Database (NED) which is operated by the Jet Propulsion Laboratory, California Institute of Technology, under contract with the National Aeronautics and Space Administration.

REFERENCES

- Aguirre, A., Hernquist, L., Schaye, J., Weinberg, D.H., Katz, N. & Gardner, J., 2001, ApJ, 560, 590
- Allen, R.J., Baldwin, J.E. & Sancisi, R., 1978, A&A, 62, 397
- Anders, E. & Grevesse, N., 1989, Geochim. Cosmochim. Acta, 53, 197
- Armus, L., Heckman, T.M., Weaver, K.A. & Lehnert, M.D., 1995, ApJ, 445, 666
- Arp, H., Burbidge, E.M., Chu, Y., Flesch, E., Patat, F., Rupprecht, G., 2002, A&A, 391, 833
- de Avillez, M.A., 2000, MNRAS, 315, 479
- Murakami, I. & Babul, A., MNRAS, 309, 161
- Bell, E.F. & de Jong, R.S., 2001, ApJ, 550, 212
- Benson, A.J., Bower, R.G., Frenk, C.S. & White, S.D.M., 2000, MNRAS, 314, 557
- Bergman, P., Aalto, S., Black, J.H. & Rydbeck, G., 1992, A&A, 265, 403
- Bessel, M.S., Castelli, F. & Plez, B., 1998, A&A, 333, 231
- Bland, J. & Tully, R.B., Nature, 334, 43
- Bottema, R. & Gerritsen, J.P.E., 1997, MNRAS, 290, 585
- Boulanger, F. & Péroul, M., 1998, ApJ, 330, 964
- Braine, J., Guelin, M., Dumke, M., Brouillet, N., Herpin, F. & Wielebinski, R. 1997, A&A, 326, 963

- Bregman, J.N., 1980, ApJ, 236, 577
- Bregman, J.N. & Glassgold, A.E., 1982, ApJ, 263, 564
- Bregman, J.N. & Houck, J.C., 1997, ApJ, 485, 159
- Bregman, J.N. & Irwin, J.A., 2002, ApJ, 56, L13
- Bregman, J.N. & Pildis, R.A., 1994, ApJ, 420, 570
- Bregman, J.N., Schulman, E. & Tomisaka, K., 1995, ApJ, 439, 155
- Brock, D., Joy, M., Lester, D.F., Harvey, P.M. & Benton Eliss., H., Jr., 1988, ApJ, 329, 208
- Burstein, D. & Heiles, C., 1982, AJ, 87, 1165
- Carpenter, J.M., 2001, AJ, 121, 2851
- Carral, P., Turner, J.L., Ho, P.T.P., 1990, ApJ, 362, 434
- Cecil, G., Bland-Hawthorn, J., Veilleux, S. & Filipenko, A.V., 2001, ApJ, 555, 338
- Cecil, G., Bland-Hawthorn, J. & Veilleux, S., 2002, ApJ, 576, 745
- Chen, K.P., Collins, N., Angione, R., Talbert, F., Hintzen, P., Smith, E.P., Stecher, T. & The UIT Team, 1997, "UV/Visible Sky Gallery on CDROM"
- Chevalier, R. & Clegg, A., 1985, Nature, 317, 44
- Chiang, W.-H., Ryu, D. & Vishniac, E.T., 1988, PASP, 100, 1386
- Clarke, T.E., Uson, J.M., Sarazin, C.L. & Blanton, E.L., 2003, ApJ, in press (astro-ph/0310508)
- Colbert, E.J.M., Baum, S.A., Gallimore, J.F., O'Dea, C.P., Lehnert, M.D., Tsvetanov, Z.I., Mulchaey, J.S. & Caganoff, S., 1996a, ApJS, 105, 75
- Colbert, E.J.M., Baum, S.A., Gallimore, J.F., O'Dea, C.P. & Christensen, J.A., 1996b, ApJ, 467, 551
- Cole, G.H.J., Mundell, C.G. & Pedlar, A., 1998, MNRAS, 300, 656
- Collins, J.A., Benjamin, R.A. & Rand, R.J., 2002, ApJ, 578, 98
- Collins, J.A., Rand, R.J., Duric, N. & Walterbos, R.A.M., 2000, ApJ, 536, 645
- Cox, D.P., ApJ, 245, 534
- Crillon, R. & Monnet, G., 1969, A&A, 2, 1
- Dahlem, M., 1997, PASP, 109, 1298
- Dahlem, M., Golla, G., Whiteoak, J. B., Wielebinski, R., Huettemeister, S. & Henkel, C., 1993, A&A, 270, 29
- Dahlem, M., Heckman, T.M., Fabbiano, G., Lehnert, M.D. & Gilmore, D., 1996, ApJ, 461, 724
- Dahlem, M., Lisenfeld, U. & Golla, G., 1995, ApJ, 444, 119
- Dahlem, M., Lazendic, J.S., Haynes, R.F., Ehle, M. & Lisenfeld, U., 2001, A&A, 374, 42
- Dahlem, M., Parmar, A., Oosterbroek, T., Orr, A., Weaver, K.A. & Heckman, T.M., 2000, ApJ, 538, 555
- Dahlem, M., Weaver, K.A. & Heckman, T.M. 1998, ApJS, 118, 401
- Dale, D.A., et al. , 2000, AJ, 120, 583
- Deharveng, J.-M., Bixler, J., Joubert, M., Bowyer, S. & Malina, R., 1986, A&A, 154, 119
- Dekel A., Silk J., 1986, ApJ, 303, 39
- Della Ceca, R., Griffiths, R.E., Heckman, T.M. & MacKenty, J.W., 1996, ApJ, 469, 662
- Della Ceca, R., Griffiths, R.E. & Heckman, T.M., 1997, ApJ, 485, 581
- de Mello, D.F., Wiklind, T. & Maia, M.A.G., 2002, A&A, 381, 771
- Désert, F.-X., Boulanger F. & Puget, J.L., 1990, A&A, 237, 215
- Dettmar, R.-J., 1990, A&A, 232, L15
- de Vaucouleurs, G. & Caulet, A., 1982, ApJS, 49, 515
- de Vaucouleurs G., de Vaucouleurs A., Corwin Jr. H.G., Buta R.J., Paturel G. & Fouque P., 1991, *Third Reference Catalogue of Bright Galaxies (RC3)* (Springer-Verlag: New York)
- Devine, D. & Bally, J., 1999, ApJ, 510, 197
- De Young, D.S. & Heckman T.M., 1994, ApJ, 431, 598

- Dickey, J.M. & Lockman, F.J., 1990, ARA&A, 28, 215.
- Done, C., Madejski, G.M. & Smith, D.A., 1996, ApJ, 463, L63
- Douglas, J.N., Bash, F.N., Arakel Bozayan, F., Torrence, G.W., Wolfe, C., 1996, AJ, 111, 1945
- Ekers, R.D. & Sancisi, R., 1977, A&A, 54, 973
- Elfhag, T., Booth, R.S., Hoglund, B., Johansson, L.E.B. & Sandqvist, Aa., 1996, A&AS, 115, 439
- Elmouttie, M., Haynes, R.F., Jones, K.L., Ehle, M., Beck, R., Harnett, J.I. & Wielebinski, R., 1997, MNRAS, 284, 830
- Engelbracht, C.W., Rieke, M. J., Rieke, G.H., Kelly, D.M., Achtermann, J.M., 1998, ApJ, 505, 639
- Fabbiano, G., Heckman, T.M., Keel, W.C., 1990, ApJ, 355, 442
- Fabbiano, G. & Juda, J.Z., 1997, ApJ, 476, 666
- Fabbiano, G. & Trinchieri, G., 1984, ApJ, 286, 491
- Ferrara, A., Pettini, M. & Shchekinov, Y., 2000, MNRAS, 319, 539
- Ferrara, A. & Tolstoy, E., 2000, MNRAS, 313, 291
- Filippenko, A.V. & Sargent, W.L.W., 1992, AJ, 103, 28
- Ford, H.C., Dahari, O., Jacoby, G.H., Crane, P.C. & Ciadullo, R., 1986, ApJ, 311, L7
- Frster Schreiber, N.M., Genzel, R., Lutz, D., Kunze, D. & Sternberg, A., 2001, ApJ, 552, 544
- Freedman, W.L., et al. , 1994, ApJ, 427, 628
- Fry, A.M., Morrison, H.L., Harding, P. & Boroson, T.A., 1999, AJ, 118, 1209
- García-Burillo, S. & Guélin, M., 1995, A&A, 299, 657
- Gehrels, N., 1986, ApJ, 303, 336
- Giacconi, R., et al. , 2001, ApJ, 551, 624
- Gibson, B.K., Loewenstein, M. & Mushotsky, R.F., 1997, MNRAS, 290, 623
- Griffiths, R.E., Ptak, A., Feigelson, E.D., Garmire, G., Townsley, L., Brandt, W.N., Sambruna, R. & Bregman, J.N., Science, 290, 1325
- Golla, G., 1999, A&A, 345, 778
- Golla, G., Allen, M.L. & Kronberg, P.P., 1996, ApJ, 473, 244
- Golla, G., Dettmar, R.-J. & Domgörgen, H., 1996, A&A, 313, 439
- Golla, G. & Hummel, E., 1994, A&A, 284, 777
- Golla, G. & Wielebinski, R., 1994, A&A, 286, 733
- Grevesse, N. & Sauval, A.J., 1998, Space Sci. Rev., 85, 161
- Guianazzi, M., Matt, G., Brandt, W.N., Antonelli, L.A., Barr, P. & Bassani, L., 2000, A&A, 356, 463
- Hameed, S. & Devereux, N., 1999, AJ, 118, 730
- Hardcastle, M.J., 2000, A&A, 357, 884
- Hawarden, T.G., Israel, F.P., Geballe, T.R. & Wade, R., 1995, MNRAS, 276, 1197
- Haynes, M.P., Giovanelli, R. & Chincarini, G.L., 1984, ARA&A, 22, 445
- Heckman, T.M., 1980, A&A, 87, 152
- Heckman, T.M., 1999, Ap&SS, 266, 3
- Heckman, T. M., Armus, L., & Miley, G. K. 1990, ApJS, 74, 833
- Heckman, T.M., 2001, in Gas and Galaxy Evolution, ed. J.E. Hibbard, M. Rupen, & J. H. van Gorkom (San Francisco: ASP), 345
- Hollenbach, D.J. & Tielens, A.G.G.M., 1997, ARA&A, 35, 179
- Holweger, H., 2001, in AIP Conf. Ser. 598, Solar and Galactic Composition, ed. R.F. Wimmer-Schweingruber (New York: Springer), 23
- Hoopes, C.G., Walterbos, R.A.M. & Greenawalt, B.E., 1996, AJ, 112, 1429
- Hoopes, C.G., Walterbos, R.A.M. & Rand, R.J., 1999, ApJ, 552, 669
- Howk, J.C. & Savage, B.D., 1997, AJ, 114, 2463
- Howk, J.C. & Savage, B.D., 1999, AJ, 119, 644
- Ichikawa, T., Yanagisawa, K., Itoh, N., Tarusawa, K., van Driel, W. & Ueno, M., 1995, AJ, 109, 2038

- Irwin, J.S. & Seaquist, E.R., 1988, *ApJ*, 335, 658
- Irwin, J.S. & Seaquist, E.R., 1991, *ApJ*, 371, 111
- Irwin, J.A., Seaquist, E.R., Taylor, A.R. & Duric, N., 1987, *ApJ*, 313, L91
- Irwin, J.S. & Sofue, Y., 1996, *ApJ*, 464, 738
- Israel, F.P., van der Werf, P.P., Hawarden, T.G. & Aspin, C., 1998, *A&A*, 336, 433
- Jaaret, T.H., Chester, T., Cutri, R., Schneider, S. & Huchra, J.P., 2003, *AJ*, 125, 525
- Kaaret, P., Prestwich, A.H., Zezas, A., Murray, S.S., Kim, D., Kilgard, R.E., Schlegel, E.M. & Ward, M.J., 2001, *MNRAS*, 321, L29
- Karachentsev I.D. & Sharina M.E., 1997, *A&A*, 324, 457
- Kennicutt, R.C., 1998a, *ApJ*, 498, 541
- Kennicutt, R.C., 1998b, *ARA&A*, 36, 189
- Kennicutt, R.C., Tamblyn, P. & Congdon, C.W., 1994, *ApJ*, 435, 22
- Kewley, L.J., Heisler, C.A., Dopita, M.A. & Lumsden, S., 2001, *ApJS*, 132, 37
- Koorneef, J., 1993, *ApJ*, 403, 581
- Kromendy, J. & Bahcall, J.N., 1974, *AJ*, 79, 671
- Krabbe, A., Böker, T. & Maiolino, R., 2001, *ApJ*, 557, 626
- Kruit, P.C. van der, 1984, *A&A*, 140, 470
- Larson, R.B., 1974, *MNRAS*, 169, 229
- Lehnert, M. & Heckman, T.M., 1995, *ApJS*, 97, 89
- Lehnert, M. & Heckman, T.M., 1996, *ApJ*, 472, 546
- Lehnert, M.D., Heckman, T.M. & Weaver, K.A., 1999, *ApJ*, 523, 575
- Levenson, N.A., Krolik, J.H., Życki, P.T., Heckman, T.M., Weaver, K.A., Awaki, H. & Terashima, T., 2002, *ApJ*, 573, L81
- Levenson, N.A., Weaver, K.A. & Heckman, T.M., 2001a, *ApJS*, 133, 269
- Levenson, N.A., Weaver, K.A. & Heckman, T.M., 2001b, *ApJ*, 550, 230
- Lira, P., Johnson, R. & Lawrence, A., 2002, *MNRAS* in press (astro-ph/0206123)
- Lynds, C.R. & Sandage, A.R., 1963, *ApJ*, 137, 1005
- McCarthy, P.J., Heckman, T.M. & van Breugel, W., 1987, *AJ*, 92, 264
- McKee, C.F., 1995, in *ASP Conf Series 80, The Physics of the Interstellar Medium*, A. Ferrara, C.F. McKee, C. Heiles & P.R. Shapiro (San Francisco: ASP), 292
- McKee, C.F. & Ostriker, J.P., 1977, *ApJ*, 218, 148
- McKeith, C.D., Greve, A., Downes, D. & Prada, F., 1995, *A&A*, 293, 703
- Mac Low, M.-M. & Ferrara, A., 1999, *ApJ*, 513, 142
- Mac Low, M.-M. & McCray, R., 1988, *ApJ*, 324, 776
- Maddox, S.J., Efstathiou, G., Sutherland, W.J., Loveday, J., 1990, *MNRAS*, 243, 692
- Madejski, G., Życki, O., Done, C., Valinia, A., Blanco, P., Rothschild, R. & Turek, B., 2000, *ApJ*, 535, L87
- Marconi, A., Oliva, E., van der Werf, P.P., Maiolino, R., Schreier, E.J., Macchetto, F. & Moorwood, A.F.M., 2000, *A&A*, 357, 24
- Markevitch, M., 2001, "General discussion of the quiescent and flare components of the ACIS background," (CXO: Cambridge), http://asc.harvard.edu/cal/Links/Acis/acis/Cal_prods/bkgnd/current/back
- Martin, C. & Kern, C., 2001, *ApJ*, 555, 258
- Martin, C.L., Heckman, T.M. & Kobulnicky, H.A., 2002, *ApJ*, 574, 663
- Matsumoto, H., Tsuru, T.G., Koyama, K., Awaki, H., Canizares, C.R., Kawai, N., Matsushita, S., Prestwich, A., Ward, M., Zezas, A.L. & Kawabe, R., 2001, *ApJ*, 547, L25
- Matsushita, S., Kawabe, R., Matsumoto, H., Tsuru, T.G., Kohno, K., Morite, K.-I., Okumura, S.K. & Vila-Vilaró, B., 2000, *ApJ*, 545, L107
- Mayya, Y.D. & Rengarajan, T.N., 1997, *AJ*, 114, 932
- Mewe R., Kaastra J. S., Liedahl D. A., 1995, *Legacy*, 6, 16
- Miller, S.T. & Veilleux, S., 2003, *ApJS*, 148, 383

- Moorwood, A.F.M. & Oliva, E., 1994, *ApJ*, 429, 602
- Moorwood, A.F.M., van der Werf, P.P., Kotilainen, J.K., Marconi, A. & Oliva, E., 1996, *A&A*, 308, L1
- Moran, E.C., Lehnert, M.D., Helfand, D.J., 1999, *ApJ*, 526, 649
- Morrison, R. & McCammon, D., 1983, *ApJ*, 270, 119
- Muxlow, T.W.B., Pedlar, A., Wilkinson, P.N., Axon, D.J., Sanders, E.M. & de Bruyn, A.G., 1994, *MNRAS*, 266, 455
- Nakai, N., 1989, *PASJ*, 41, 1107
- Norman, C.A. & Ferrara, A., 1996, *ApJ*, 467, 280
- Norman, C. A. & Ikeuchi, S., 1989, *ApJ*, 345, 372
- Olling, R.P., 1996, *AJ*, 112, 457
- Ott, M., Whiteoak, J.B., Henkel, K. & Wielebinski, R., 2001, *A&A*, 372, 463
- Pence, W.D., 1981, *ApJ*, 247, 473
- Pietsch, W., Trinchieri, G. & Vogler, A., 1998, *A&A*, 340, 351
- Pietsch, W., et al. , 2001, *A&A*, 365, L174
- Popescu, C.A., Tuffs, R.J., Fischera, J. & Völk, H., 2000, *A&A*, 354, 480
- Ptak, A., Serlemitsos, P., Yaqoob, T., Mushotzky, R. & Tsuru, T., 1997, *AJ*, 113, 1286
- Puche, D., Carignan, C., 1988, *AJ*, 95, 1025
- Puche, D., Carignan, C., van Gorkom, J.H., 1991, *AJ*, 101, 456
- Pudritz, R.E. & Fiege, J.D., 2000, in *ASP Conf. Series* 168, *New Perspectives on the Interstellar Medium*, A.R. Taylor, T.L. Landecker & G. Joncas, (San Francisco: ASP), 235
- Radovich, M., Kahanpää, J., Lemke, D., 2001, *A&A*, 377, 73
- Rand, R., 1994, *A&A*, 285, 833
- Rand, R.J., 2000, *ApJ*, 535, 663
- Rand, R.J., Kulkarni, S.R. & Hester, J.J., 1990, *ApJ*, 352, 1
- Rand, R.J., Kulkarni, S.R. & Hester, J.J., 1992, *ApJ*, 396, 97
- Read, A.M. & Ponman, T.J., 2001, *MNRAS*, 328, 127
- Read, A.M., Ponman, T.J., Strickland, D.K., 1997, *MNRAS*, 286, 626
- Rice, W., Lonsdale, C.J., Soifer, B.T., Neugebauer, G., Kopan, E.L., Llyod, L.A., deJong, T. & Habing, H.J., 1988, *ApJS*, 68, 91
- Rots, A. H., 1978, *AJ*, 83, 219
- Roth, J., Mould, J.R. & Davies, R.D., 1991, *AJ*, 102, 1303
- Rupen, M.P., 1991, *AJ*, 102, 48
- Rupen, M.P., van Gorkom, J.H., Knapp, G.R. & Gunn, J.E., 1987, *AJ*, 94, 61
- Sanders, D.B. & Mirabel, I.F., 1996, *ARA&A*, 34, 749
- Savage, B.D. & Sembach, K.R., 1996, *ARA&A*, 34, 279
- Sawado-Satoh, S., Inoue, M., Shibata, K.M., Kameno, S., Migenes, V., Nakai, N. & Diamond, P.J., 2000, *PASJ*, 52, 421
- Schiano, A.V.R., 1985, *ApJ*, 299, 24
- Schlickeiser, R., Werner W., & Wielebinski, R., 1984, *A&A*, 140, 277
- Schmidt, G.D., Angel, J.R.P. & Cromwell, R.H., 1976, *ApJ*, 206, 888
- Scoville, N.Z., Thakkar, D., Carlstrom, J.E. & Sargent, A.I., 1993, *ApJ*, 404, L59
- Schurch, N.J., Roberts, T.P. & Warwick, R.S., 2002, *MNRAS*, 335, 241
- Seaquist, E.R., Davis, L. & Bignell, R.C., 1978, *A&A*, 63, 199
- Shapiro, P.R. & Field, G.B., 1976, *ApJ*, 205, 762
- Shapiro, P.R., Giroux, M.L. & Babul, A., 1994, *ApJ*, 427, 25
- Shapley, A.E., Steidel, C.C., Pettini, M. & Adelberger, K.L., 2003, *ApJ*, 588, 65
- Shopbell, P.L., Bland-Hawthorn, J., 1998, *ApJ*, 493, 129

- Silich, S.A. & Tenorio-Tagle, G., 1998, MNRAS, 299, 249
- Silich, S.A. & Tenorio-Tagle, G., 2001, ApJ, 552, 91
- Slavin, J.D. & Cox, D.P., 1993, ApJ, 417, 187
- Smith, A.M., et al., 2001, ApJ, 546, 829
- Snowden, S.L., et al., 1995, ApJ, 454, 643
- Snowden, S.L. & Pietsch, W., 1995, ApJ, 452, 627
- Sofue, Y., 1997, PASJ, 49, 17
- Sofue, Y. & Vogler, A., 2000, A&A, 370, 53
- Sofue, Y., Wakamatsu, K. & Malin, D.F., 1994, AJ, 108, 2102
- Soifer, B.T., et al., 1989, AJ, 98, 1766
- Soifer, B.T., Sanders, D.B., Madore, B.F., Neugebauer, G., Danielson, G.E., Elias, J.H., Lonsdale, C.J. & Rice, W.L., 1987, ApJ, 320, 238
- Sommer-Larsen, J., Toft, S., Rasmussen, J., Pedersen, K., Gotz, M. & Portinari, L., 2003, Ap&SS, 284, 693
- Sorai, K., Nakai, N., Kuno, N., Nishiyama, K. & Hasegawa, T., 2000, PASJ, 52, 785
- Spoon, H.W.W., Koornneef, J., Moorwood, A.F.M., Lutz, D. & Tielens, A.G.G.M., 2000, A&A, 357, 898
- Strickland, D.K., 2002, in ASP Conf. Series 253 "Chemical Enrichment of the ICM and IGM," Eds. R. Fusco-Femiano & F. Matteucci, (Sheridan Books: Michigan), 387
- Strickland, D.K., Heckman, T.M., Weaver, K.A. & Dahlem, M., 2000, AJ, 120, 2965
- Strickland, D.K., Heckman, T.M., Colbert, E.J.M., Hoopes, C.G. & Weaver, K.A., 2003, in "A Massive Star Odyssey, from Main Sequence to Supernova," Eds. K.A. van der Hucht, A. Herrero & C. Esteban (ASP: San Francisco), 612
- Strickland, D.K., Heckman, T.M., Colbert, E.J.M., Hoopes, C.G. & Weaver, K.A., 2004, submitted to ApJ (Paper II)
- Strickland, D.K., Heckman, T.M., Weaver, K.A., Hoopes, C.G. & Dahlem, M., 2002a, ApJ, 568, 689
- Strickland, D.K., Ponman, T.J. & Stevens, I.R., 1997, A&A, 320, 378
- Strickland, D.K. & Stevens, I.R., 1999, MNRAS, 306, 43
- Strickland, D.K. & Stevens, I.R., 2000, MNRAS, 314, 511
- Suchkov, A.A., Balsara, D.S., Heckman, T.M., Leitherner, C., 1994, ApJ, 430, 511
- Suchkov A. A., Berman V. G., Heckman T. M., Balsara D. S., 1996, ApJ, 463, 528
- Sugai, H., Davies, R.I. & Ward, M.J., 2003, ApJ, 584, 9
- Swaters, R.A., Sancisi, R. & Hulst, J.M., van der, 1997, ApJ, 491, 140
- Toft, S., Rasmussen, J., Sommer-Larsen, J. & Pedersen, K., 2002, MNRAS, 335, 799
- Townsley, L.K., Broos, P.S., Garmire, G.P. & Nousek, J.A., 2000, ApJ, 534, L139
- Tremonti, C.A., et al., in preparation
- Trotter, A.S., Greenhill, L.J., Moran, J.M., Reid, M.J., Irwin, J.A. & Lo, K.-Y., 1998, ApJ, 495, 740
- Tsuru, T.G., Awaki, H., Koyama, K. & Ptak, A., 1997, PASJ, 49, 619
- Ulvestad, J.S., 2000, AJ, 120, 670
- Ulvestad, J.S. & Antonucci, R.R.J 1997, ApJ, 488, 621
- Veilleux, S., Cecil, G., Bland-Hawthorn, J. & Shopbell, P.L., 2002, Revista Mexicana de Astronomia y Astrofisica, 13, 222
- Veilleux, S., Cecil, G., Bland-Hawthorn, J., Tully, R.B., Filippenko, A.V. & Sargent, W.L.W., 1994, ApJ, 433, 48
- Veilleux, S. & Rupke, D.S., 2002, ApJ, 565, L63
- Veilleux, S., Shopbell, P.L. & Miller, S.T., 2001. AJ, 121, 198
- Vogler, A. & Pietsch, W., 1996, A&A, 311, 35
- Vogler, A., Pietsch, W. & Kahabka, P., 1995, A&A, 305, 71
- Voit, G.M., 1996, ApJ, 465, 548

- Wainscoat, R.J., de Jong, T. & Wesselius, P.R., 1987, A&A, 181, 225
- Wang, J., Heckman, T.M. & Lehnert, M.D., 1997, ApJ, 491, 114
- Wang, Q.D., Immler, S., Walterbos, R., Lauroesch, J.T. & Breitschwerdt, D., 2001, ApJ, 555, L99
- Wang, Q.D., Walterbos, R.A.M., Steakley, M.F., Norman, C.A. & Braun, R., 1995, ApJ, 439, 176
- Weaver, K.A., Heckman, T.M. & Dahlem, M., 2000, ApJ, 534, 684
- Weaver, K.A., Heckman, T.M., Strickland, D.K. & Dahlem, M., 2002, ApJ, 576, L19
- Weaver, K.A., Mushotzky, R.F., Serlemitsos, P.J., Wilson, A.S., Elvis, M. & Briel, U., 1995, ApJ, 442, 597
- Weiss, A., Walter, F., Neininger, N. & Klein, U., 1999, A&A, 345, L23
- Weliachew, I., Fomalont, E.B. & Greisen, E.W., 1984, A&A, 137, 335
- Whiteoak, J.B., 1986, Proc. Astronom. Soc. Australia., 6, 467
- Williams, R.J.R., Baker, A.C. & Perry, J.J., 1999, MNRAS, 310, 913
- Wills, K.A., Pedlar, A. & Muxlow, T.W.B., 2002, MNRAS, 331, 313
- Wiseman, J.J. & Ho, P.T.P., 1998, ApJ, 502, 676
- Yun, M.S., Ho, P.T.P. & Lo, K.Y., 1993, ApJ, 411, L17
- Zezas, A.L., Georgantopoulos, I. & Ward, M.J., 1998, MNRAS, 301, 915
- Zhao, J.-H., Anantharamaiah, K.R., Goss, W.M. & Viallefond, F., 1997, ApJ, 482, 186